

## ABSTRACT

SRIVASTAVA, DEEPTI. Monte Carlo Simulations of Adsorption and Reaction of Lennard-Jones Molecules in Carbon Pores and Protein-Polyelectrolyte Complexation (Under the direction of Dr. Keith Gubbins and Dr. Erik Santiso).

Understanding systems involving many-particle interactions through experiments alone can often be a difficult task. This task is further complicated when examining systems at the nano-scale that involve the study of properties such as pressures and reaction equilibrium. In such scenarios and others, molecular simulations and more specifically, Monte Carlo techniques, provide great value in finding answers to questions that experiments struggle to answer.

One area that has made significant progress and greatly benefited from Monte Carlo simulation studies is the understanding of adsorption in pores. Recently, several studies have found that phenomena that normally occur at extremely high pressures in a bulk phase can occur in nano-phases confined within porous materials at much lower bulk phase pressures, thus providing an alternative route to study high-pressure phenomena. In order to better understand the pressures in these confined phases, we use Constant-Pressure Monte Carlo methods to examine the effect of variables such as the molecular shape, strength of the fluid-wall interactions, and pore width, on the tangential pressure for carbon slit-shaped pores. We find that, for multi-site molecules, the presence of additional rotational degrees of freedom leads to unique changes in the shape of the tangential pressure profile, especially in larger pores. We show that, due to the direct relationship between the molecular density and the fluid-wall interactions, the latter have a large impact on the pressure tensor. The pore size and

molecular shape can also greatly impact the layering of molecules in the pore, influencing both the shape and magnitude of the tangential pressure profile.

Additionally, it is well established that confinement within a nano-porous material can also affect reaction yield, reaction rate and even the mechanism of the reaction. These effects arise from the strong intermolecular forces between the various reacting species, including the activated state, and the pore walls, but are poorly understood. Using Reactive Monte Carlo techniques, we report the effects of confinement within a nanoporous carbon material on the equilibrium yield of the nitric oxide dimerization reaction. We study the reaction in slit-shaped carbon pores and carbon nanotubes of various widths and over a range of temperatures. We examine several approximations made in earlier molecular simulation studies, in particular the force fields used, and show that the latter have a large effect on the calculated yield. In addition, we also investigate the relationship between the high in-pore tangential pressures and the higher reaction conversion yields in slit-shaped pores.

Apart from adsorption studies, Monte Carlo simulations can also be applied in understanding systems involving biological complexes such as proteins. Experimental studies have shown the formation of soluble complexes in the pure repulsive Coulombic regime even when the net charges of the protein and the polyelectrolyte have the same sign. One theory explaining this phenomenon assumes the existence of “charged patches” on the protein surface from ion-dipole interactions, thus allowing a polyelectrolyte to bind to an oppositely heterogeneous charged protein region. Another theoretical view considers the induced-charge interactions to be the dominant factor in these complexations. This charge regulation mechanism can be described by proton fluctuations resulting from mutual rearrangements of

the distributions of the charged groups, due to perturbations of the acid-base equilibrium. Using constant-pH Monte Carlo simulations, we investigate the validity of both theories for two whey proteins,  $\alpha$ -lactalbumin ( $\alpha$ -LA) and lysozyme (LYZ). Through physical chemistry parameters, free energies of interactions, and the mapping of amino acid pKa shifts and polyelectrolyte trajectories, we show the charge regulation mechanism (*i.e.* proton fluctuations) to be the most important contributor in protein-polyelectrolyte complexation regardless of pH, dipole moment, and protein capacitance.

© Copyright 2017 Deepti Srivastava

All Rights Reserved

Monte Carlo Simulations of Adsorption and Reaction of Lennard-Jones Molecules in Carbon  
Pores and Protein-Polyelectrolyte Complexation

by  
Deepti Srivastava

A dissertation submitted to the Graduate Faculty of  
North Carolina State University  
in partial fulfillment of the  
requirements for the degree of  
Doctor of Philosophy

Chemical Engineering

Raleigh, North Carolina

2017

APPROVED BY:

---

Dr. Keith E. Gubbins  
Committee co-chair

---

Dr. Erik E. Santiso  
Committee co-chair

---

Dr. Douglas L. Irving

---

Dr. Melissa A. Pasquinelli

## DEDICATION

*I dedicate this dissertation to my parents, Alok and Nandini Srivastava, who have always stood by me while I pursued my dreams, both personal and professional. Without them, I would not be who I am today. They have always celebrated and taken pride in my accomplishments and lifted me up when I failed. They not only taught me the value of hard work and persistence, but also showed me the importance of having a well-rounded life, filled with family, friends, fun and laughter. Their unconditional love has and will always be my biggest source of strength.*

*I am eternally grateful to them.*

## **BIOGRAPHY**

Deepti Srivastava was born in Vadodara, India to her parents, Alok and Nandini Srivastava. She is their second child, following her older brother Anubhav Srivastava. She spent her early childhood years in a little town called Nagothane, about 70 miles outside of Mumbai. When she was 6 years old, she moved to Singapore with her family and spent the next 8 years there, attending Bukit View Primary School and Methodist Girls' Secondary School. From a young age, Deepti was always a curious child and enjoyed learning about science. Her two favorite topics were dinosaurs and space. At age 14, she moved to Houston, Texas when her father was offered a position at ExxonMobil's Baytown location. She attended Clear Lake High School where she continued her studies by taking Pre-AP and AP science classes and pursued new hobbies such as debate and dancing.

In fall of 2006, with her parents' encouragement, Deepti went on to attend the University of Texas at Austin. She started off as an Electrical Engineering major but quickly realized her passions were leading her elsewhere. After exploring Economics, she decided to pursue the same field as her father and enrolled in the Chemical Engineering program. In her 3<sup>rd</sup> year, she went on to study abroad in France for 6 months and upon returning, started doing undergraduate experimental research under the guidance of Dr. Christopher Ellison. After graduating from UT Austin, Deepti gained further research experience under Dr. Hugh Smyth in the UT Pharmaceuticals Department and is extremely grateful for the guidance and support she received from him during this time. At the end of this year, Deepti decided to attend North Carolina State University to pursue a Ph.D. in Chemical Engineering.

After her first semester, she decided to join Dr. Gubbins' research group and began working on studying chemical reactions in pores using Monte Carlo simulations. During this time, Dr. Gubbins generously gave her the opportunity to attend several conferences all over the world and she also spent a summer in Ribeirão Preto, Brazil to collaborate on a project with Dr. Fernando Luís Barroso da Silva at the University of São Paulo. During her first couple of years of graduate school, Deepti also received guidance from Dr. Erik Santiso who offered invaluable advice and direction for her research. In her 3<sup>rd</sup> year, Deepti officially became co-advised with Dr. Erik Santiso. She is immensely grateful to both Dr. Keith Gubbins and Dr. Erik Santiso for their incredible support throughout her graduate school career.

It was also in graduate school that Deepti met her husband, Joseph Tilly, who is a current Ph.D. student at NC State. In her spare time, Deepti enjoys hiking, rock climbing, and spending time with her 4-year old Labrador, Ace the Bathound. She also loves to travel and learn about different cultures, languages and cuisines.

## ACKNOWLEDGMENTS

I first wish to thank both my advisors, Dr. Keith Gubbins and Dr. Erik Santiso, for so many reasons. Dr. Gubbins, I thank you for working tirelessly to provide financial support for me over the past 5 years, never once putting that burden on me. I thank you for the unwavering support and encouragement you have provided me over the past 5 years. When I struggled, you always gently encouraged me to persist and you never failed to give me a pat on the back when I succeeded. I am incredibly grateful for all the opportunities you gave me to travel the world and to present at several conferences. These experiences helped me grow immensely as a graduate student and I consider myself extremely lucky to have had the opportunity to interact with the leading researchers in my field through these conferences.

Dr. Santiso, I have no words to express how grateful I am for all that you've done for me in the past few years. Even though you didn't start off as my advisor, you were always there to answer my questions and guide me through the early years when I was struggling to get my simulations working. As an advisor, you always made an effort to be available despite your immensely busy schedule. From brainstorming new ideas to helping me debug my codes, your input was always invaluable. You always met me with a friendly smile and your encouragement and ideas never failed to provide me with motivation when I needed it the most.

Dr. Irving, I'm grateful to have you as a committee member and your course on Density Functional Theory was extremely useful in helping me understand the difficult concepts and in learning to use programs such as VASP. Dr. Pasquinelli, thank you for agreeing to be on my committee on such short notice and for always being cheerful, responsive, and accommodating during our email exchanges. Dr. Hall, thank you for being on my committee for the past 4

years and for the countless words of encouragement during my time as a graduate student. I still remember you approaching me after my oral presentation at Schoenborn 2016 to let me know that you were very proud of me for a job well done. Your glowing praise, then and on multiple other occasions, always made my day and motivated me to keep going.

I'd like to acknowledge multiple people in the department for their help and company throughout the years. These include Sandra Bailey, Maria Moreno, Saundra Dobey, Angela Efimenko and June McKoy, to name a few. I'm also grateful to all the members of the Gubbins and Santiso group for their helpful conversations and invaluable feedback regarding my research. I'd especially like to thank Katherine Phillips, Liangliang "Paul" Huang, Cody Addington, Nathan Duff, Mariah King, Kaihang Shi, Matt Mansell, Laura Weiser, Amulya Pervaje, Jennifer Clark, Amit Misra, Christopher Walker, and Chengxiang Liu.

I'd like to thank my parents, Alok and Nandini Srivastava, for their constant love and support throughout my Ph.D. I would be remiss in not mentioning the wonderful friendships I established in graduate school; the past few years would have been a lot less fun without Jennifer Ovental, Drs. Erinn and Craig Needham, Dr. Brittany Mertens, Joseph and Ashton Lavoie, Dr. Daniel Armstrong, Dr. Matthew Mellilo, and Dr. Ryan Barton. I'm also incredibly grateful to my high school friends, Diana Wang and Jennifer Ge, for their friendship and for providing unwavering support from miles away.

Lastly, I would like to thank my husband, Joseph Tilly. There are no words to describe the incredible support he has shown me since we've known each other in graduate school. Thank you for always being willing to proofread my papers, listen to my practice talks, and discuss my research with me. Thank you for standing by me during my lows and cheering with

me at my highs. Thank you for being a welcome distraction when I couldn't stop worrying about research and for providing encouragement and motivation when I was disheartened. Without you, I would not have made it.

## TABLE OF CONTENTS

<b>LIST OF TABLES .....</b>	<b>xi</b>
<b>LIST OF FIGURES .....</b>	<b>xii</b>
<b>CHAPTER 1 : Introduction.....</b>	<b>1</b>
1.1 Why Molecular Simulation?.....	1
1.2 Monte Carlo Simulations .....	1
1.3 Research Agendas and Techniques used .....	4
1.3.1 Pressure Enhancement in Confined Fluids .....	4
1.3.2. Nitric Oxide Dimerization Reaction .....	7
1.3.3 Protein-Polyelectrolyte Complexation.....	9
1.4 Scope of this dissertation .....	11
1.5 References.....	14
<b>CHAPTER 2 : Pressure Enhancement in Confined Fluids: Effect of Molecular Shape and Fluid-Wall Interactions .....</b>	<b>18</b>
2.1 Introduction.....	18
2.2 Simulation Methods.....	21
2.2.1 Molecular Models .....	23
2.2.2 Pressure calculations.....	25
2.3 Results and Discussion .....	28
2.3.1 Lennard-Jones Monomers.....	29
2.3.2 Lennard-Jones Dimers .....	37
2.3.3 Lennard-Jones Trimers .....	44

2.4 Summary and Discussion of Results .....	47
2.4.1 Effect of $\alpha$ parameter .....	50
2.4.2 Effect of molecular geometry .....	52
2.4.3 Effect of pore size .....	56
2.5 Conclusion .....	59
2.6 Acknowledgement .....	59
2.6 References.....	60
<b>Chapter 3 : The Nitric Oxide Dimer Reaction in Slit-Shaped Pores and Carbon Nanotubes .....</b>	<b>64</b>
3.1 Introduction.....	64
3.2 Simulation Methods.....	68
3.2.1 Monte Carlo Simulations .....	68
3.2.2 Pore Models .....	69
3.3 Results and Discussion .....	73
3.3.1 Sensitivity Analysis and Ab Initio Calculations .....	73
3.3.2 Effect on Reaction Conversion .....	78
3.3.3 Effect on Slit-Pore Pressure Tensor.....	84
3.3.4 NO Dimerization in Cylindrical Pores.....	89
3.4 Conclusion .....	94
3.5 Acknowledgement .....	94
3.5 References.....	96

<b>CHAPTER 3 : Computationally mapping pKa shifts due to the presence of a polyelectrolyte chain around milk proteins.....</b>	<b>100</b>
4.1 Introduction.....	100
4.2 Simulation Methods.....	107
4.2.1 Protein model.....	110
4.2.2 Polyanion model .....	112
4.2.3 System details .....	113
4.3 Results and Discussion .....	116
4.3.1 Main physical chemistry parameters .....	116
4.3.2 Free energy of interactions.....	117
4.3.3 pKa shifts due to the interactions with the polyelectrolyte.....	121
4.3.4 Accuracy of the pKa shifts.....	129
4.4 Conclusion .....	130
4.5 Acknowledgment.....	131
4.6 References.....	132
Appendix.....	139
<b>CHAPTER 4 : Conclusions and Future Work.....</b>	<b>144</b>
5.1 Pressure Enhancement in Confined Fluids .....	144
5.2 The Nitric Oxide Dimer Reaction.....	146
5.3 Protein-Polyelectrolyte Interactions .....	147

## LIST OF TABLES

<b>Table 2.1:</b> Summary of the effect of molecular shape, fluid-wall interactions, and pore width on different parameters .....	48
<b>Table 3.1:</b> Partition functions for the NO monomer and (NO) <sub>2</sub> dimer .....	71
<b>Table 4.1:</b> Titrating residues in the proteins studied. The dissociation constants (pK <sub>0</sub> ) for the isolated amino acids are given in the second row followed by the number of occurrences of each ionizable amino acid in both proteins. The data was taken from the experimental work of Nozaki & Tanford. <sup>55</sup> .....	112
<b>Table 4.2:</b> Computed protein net charge number (Z), charge capacitance (C) and dipole moment number (μ) for LYZ at different pH regimes. These data were obtained from the MC runs with set A. The Coulombic, charge regulation and patch contributions were analytically calculated in kT units using the equations for A <sub>cou</sub> , A <sub>reg</sub> , and A <sub>dip</sub> , respectively. The total contribution was obtained by adding these three terms. The ratio Regulation/Patch was given by A <sub>reg</sub> /A <sub>dip</sub> . Radii for LYZ and the polyelectrolyte were estimated as 28 and 30 Å, respectively. <sup>50</sup> .....	117
<b>Table 4.3:</b> Calculated and Experimental pKa values of lysozyme. <sup>(a)</sup> Data taken from Chen et al. <sup>57</sup> at 50mM of salt. <sup>(b)</sup> Data taken from Barroso da Silva et al. <sup>21</sup> .....	130

## LIST OF FIGURES

<b>Figure 1.1:</b> Monte Carlo moves associated with CP-GEMC. ....	6
<b>Figure 2.1:</b> Constant-pressure Gibbs Ensemble Monte Carlo for narrow pores. Dotted lines signify periodic boundaries. ....	22
<b>Figure 2.2:</b> Different molecular geometries for the monomer, dimer, and trimer. ....	24
<b>Figure 2.3:</b> The normal and tangential pressure components in a slit pore. ....	26
<b>Figure 2.4:</b> Example of the Irving-Kirkwood method where the pore is divided into bins of equal width. The interactive energy, $u(r_{ij})$ , contributes linearly to the bins between $i$ and $j$ . In this case, $u(r_{ij})$ would contribute to bins $z_2, z_3, z_4, z_5$ , and $z_6$ . ....	27
<b>Figure 2.5:</b> (a) Pressure and density profiles for the monomers in the pore of width $3\sigma$ , at $\alpha = 10$ . (b) Snapshot of the equilibrium configuration of the monomers in the $3\sigma$ pore. (c) Radial distribution function in the $xy$ plane for the contact layer in the $3\sigma$ pore at $\alpha = 10$ . (d) The intermolecular force between two monomer particles with the repulsive and attractive regions highlighted. The blue dot is the average nearest neighbor distance between two molecules in the $xy$ plane for the $3\sigma$ pore at $\alpha = 10$ . In Fig. 2.5(a) the number densities plotted are the number of molecules, $N_m$ , in a given bin of width $0.1 \text{ \AA}$ divided by the bin volume. ....	29
<b>Figure 2.6:</b> (a) Pressure and density profiles for the monomers in the $3\sigma$ pore, at $\alpha = 39$ (b) In-plane radial distribution function for the contact layer in the $3\sigma$ pore at $\alpha = 39$ . ....	31
<b>Figure 2.7:</b> (a): Pressure and density profiles for the monomers in the pore of width $5\sigma$ pore, at $\alpha = 10$ ; (b) Snapshot of the equilibrium configuration of the monomers in the $5\sigma$ pore; (c) In-plane radial distribution function in the contact layer in the $5\sigma$ pore at $\alpha = 10$ . ....	33

- Figure 2.8:** (a) Pressure and density profiles for the monomers in the pore of width  $5\sigma$ , at  $\alpha = 39$ ; (b) In-plane radial distribution function for the contact layer of monomers in the  $5\sigma$  pore at  $\alpha = 39$ . ..... 34
- Figure 2.9:** Snapshots of simulations, showing compression of the adsorbed contact layer next to the pore wall in xy plane for (a)  $r_{xy} = 3.15$  and (b)  $r_{xy} = 2.95$ , respectively. (c) Lateral compression in the adsorbed layer ..... 36
- Figure 2.10:** (a) Pressure and density profiles for the dimers in the pore of width  $3\sigma$ , at  $\alpha = 10$ ; (b) Snapshot of the equilibrium configuration of the dimers in the  $3\sigma$  pore at  $\alpha = 10$ ; (c) Histogram showing the distribution of the angles of the dimers relative to the pore wall; (d) In-plane radial distribution function for the dimer sites in the  $3\sigma$  pore, at  $\alpha = 10$ . ... 37
- Figure 2.11:** (a) Pressure and density profiles for the dimers in the pore of width  $3\sigma$ ,  $\alpha = 39$ ; (b) Snapshot of the equilibrium configuration of the dimers in the  $3\sigma$  pore,  $\alpha = 39$ ; (c) Histogram of the distribution of angles of the dimers relative to the pore wall; (d) In-plane radial distribution function for dimer sites in the  $3\sigma$  pore,  $\alpha = 39$ . ..... 39
- Figure 2.12:** (a) Pressure and density profiles for the dimers in the  $5\sigma$  pore, at  $\alpha = 10$ ; (b) Snapshot of the equilibrium configuration of the dimers in the  $5\sigma$  pore,  $\alpha = 10$ ; (c) Histogram of the angles of the dimers relative to the pore wall; (d) In-plane radial distribution function for the dimer sites in the  $5\sigma$  pore,  $\alpha = 10$ . ..... 41
- Figure 2.13:** (a) Pressure and density profiles for the dimers in a pore width of  $5\sigma$ , at  $\alpha = 39$ ; (b) Snapshot of the equilibrium configuration of the monomers in the  $5\sigma$  pore,  $\alpha = 39$ ; (c) Histogram of the angles of the dimers relative to the pore wall; (d) In-plane radial distribution function for the dimer sites in the  $5\sigma$  pore,  $\alpha = 39$ . ..... 43
- Figure 2.14:** (a) Pressure and density profiles for the trimers in the  $3\sigma$  pore, at  $\alpha = 39$ ; (b) Two main orientations of the trimer in the  $3\sigma$  pore (c) Snapshot of the equilibrium

configuration of the trimers in the $3\sigma$ pore, $\alpha = 39$ ; (d) Histogram of the angles of the trimers relative to the pore wall; (e) In-plane radial distribution function for the trimer sites in the $3\sigma$ pore, $\alpha = 39$ .....	44
<b>Figure 2.15:</b> (a) Pressure and density profiles for the trimers in the $5\sigma$ pore, at $\alpha = 39$ ; (b) Snapshot of the equilibrium configuration of the trimers in the $5\sigma$ pore, $\alpha = 39$ ; (c) Histogram of the angles of the trimers relative to the pore wall; (d) In-plane radial distribution function for the trimer sites in the $5\sigma$ pore, $\alpha = 39$ .....	46
<b>Figure 2.16:</b> (a) The average separation distance between nearest neighbor monomer sites in the xy plane for all four monomer systems are shown on the Lennard-Jones intermolecular force plot as colored circles. Figure 2.5(d) is shown on the top right of each figure, with the shaded region identifying the area being plotted. (b) The average separation distance between nearest neighbor dimer sites in the xy plane for all four dimer systems are shown on the Lennard-Jones intermolecular force plot. ....	49
<b>Figure 2.17:</b> An enlarged view of the tangential pressure tensor profile for the dimers in a $5\sigma$ pore at $\alpha = 39$ , showing the broad shoulder effect.....	54
<b>Figure 2.18:</b> An enlarged of the tangential pressure for dimers in the $5\sigma$ pore at $\alpha = 10$ , showing the slight broad shoulder effect. ....	58
<b>Figure 3.1:</b> Simulation snapshots of the (a) (8,8) and (b) (10,10) nanotube bundles. The nanotube diameters are (a) 10.9 Å and (b) 13.6 Å and the intertubular distance is 3.35 Å for both bundles. ....	70
<b>Figure 3.2:</b> A sensitivity analysis on the effect of changing the interaction energy for the NO-wall interaction on the reaction conversion. A multiplication factor of 1 corresponds to the NO-wall interaction energy predicted by the Lorentz-Berthelot mixing rules. The (NO) <sub>2</sub> -wall interaction energy in these calculations was kept constant at the value predicted by the Lorentz-Berthelot rules. ....	74

**Figure 3.3:** A sensitivity analysis on the effect of changing the interaction energy for the (NO)<sub>2</sub>-wall interaction on the reaction conversion. A multiplication factor of 1 corresponds to the (NO)<sub>2</sub>-wall interaction energy predicted by the Lorentz-Berthelot mixing rules. The NO-wall interaction energy in these calculations was kept constant at the value predicted by the Lorentz-Berthelot rules. The points show the number of molecules in the pore, and should be read on the left axis. The dotted line shows the mole fraction of dimer in the pore. .... 75

**Figure 3.4:** Left: Visualization of the (a) structure and (c) HOMO orbitals for the NO monomers. Right: Visualization of the (b) structure and (d) HOMO orbitals for the NO dimers..... 77

**Figure 3.5:** Reaction conversion in the bulk phase and different pore sizes from 120 K to 160 K..... 79

**Figure 3.6:** Average reaction conversion vs. pore width at  $P_{\text{bulk}} = 0.16$  bar..... 80

**Figure 3.7:** *Left:* Configurations of the center of mass in (a)  $3\sigma$ , (c)  $3.5\sigma$ , (e)  $4\sigma$ , (g)  $4.5\sigma$ , (i)  $5\sigma$  and (k)  $5.5\sigma$  pore, respectively at 160 K. Orange molecules are monomers and blue molecules are dimers. *Right:* Configurations of the molecular sites in (b)  $3\sigma$ , (d)  $3.5\sigma$ , (f)  $4\sigma$ , (h)  $4.5\sigma$ , (j)  $5\sigma$  and (l)  $5.5\sigma$  pore, respectively at 160 K. The green spheres represent the centers of the (NO)<sub>2</sub> dimers, while purple spheres indicate the NO monomers. The dark blue spheres are the LJ sites in the NO and (NO)<sub>2</sub> molecules. .... 81

**Figure 3.8:** Pressure and density profiles for all 6 pore sizes at 160 K:  $3\sigma$  (top left),  $3.5\sigma$  (top right),  $4\sigma$  (center left),  $4.5\sigma$  (center right),  $5\sigma$  (bottom left),  $5.5\sigma$  (bottom right). Blue lines represent the NO dimer reduced density and orange lines represent the NO monomer reduced density. The red lines are the tangential pressure and green lines are the normal pressure. .... 85

<b>Figure 3.9:</b> (a) Left: radial distribution function for the LJ sites for the $5\sigma$ pore at 160 K in the $xy$ plane. (b) Right: Intermolecular force plot for the interaction between two LJ sites on different molecules, showing the repulsive and attractive regions. The blue dot indicates the most probable site separation distance for $5\sigma$ pore at 160 K.....	86
<b>Figure 3.10:</b> Individual configurational contributions to the tangential pressure tensor for the $5\sigma$ pore at 160 K. ....	87
<b>Figure 3.11:</b> Configuration of NO molecules in the $xy$ plane for the $3\sigma$ slit pore at 160 K. .	89
<b>Figure 3.12:</b> Conversion of the NO dimerization reaction in (8,8) and (10,10) nanotube bundles. Simulation temperatures ranged from 120 – 160 K. The bulk pressure was kept constant at 0.16 bar. ....	90
<b>Figure 3.13:</b> Simulation snapshots of the NO dimerization reaction in the carbon nanotube bundles. a) configuration of the molecular interaction sites in the (8,8) bundle, b) configuration of the centers of mass in the (8,8) bundle, c) configuration of the molecular interaction sites in the (10,10) bundle, d) configuration of the centers of mass in the (10,10) bundle. In Figures (a) and (c), the dark blue spheres are the LJ sites in the NO and (NO) <sub>2</sub> molecules. In Figures (b) and (d), green spheres represent the centers of the (NO) <sub>2</sub> dimers, while purple spheres indicate the NO monomers. ....	92
<b>Figure 3.14:</b> (a) Number density profile for the (8,8) center nanotube (b) Number density profile for the (10,10) center nanotube .....	93
<b>Figure 4.1:</b> Schematic representation of the model system in explicit salt. a) <i>Top</i> : System with no polyelectrolyte. Protein is surrounded by counterions and added salt particles. b) <i>Bottom</i> : A polyanion, consisting of 21 negatively charged monomers, is also present with the protein system. Simulations with both models were carried out at different pH regimes <sup>45</sup> .....	109

**Figure 4.2:** Computed potentials of mean force between the centers of mass of lysozyme and the polyelectrolyte chain. Data are from the MC runs with set B at pI assuming different charge models. Simulation parameters and details are chosen as in Barroso da Silva et al.<sup>45</sup> pH regimes where a negative minimum for  $\beta w(r)$  is observed are shown with solid lines while repulsive cases are shown with dashed lines for all three panels. .... 119

**Figure 4.3:** Computed potentials of mean force between the centers of mass of the proteins and the polyelectrolyte chain. **a)** Data for LYZ at solution pH equal to 7.0, 10.9 (pI) and 13.0. **b)** Data for  $\alpha$ -LA at solution pH equals to 4.0, 5.3 (pI) and 8.0. pH regimes where a negative minimum for  $\beta w(r)$  is observed are shown with solid lines while repulsive cases are shown with dashed lines for all three panels. .... 120

**Figure 4.4:** Snapshots of the  $\alpha$ -LA protein showing the difference in pKa values between the protein in the presence of the polyanion and for the isolated protein simulations. The amino acid side chains undergoing a change in pKa are labeled. Blue indicates a positive shift in pKa, while red indicates a negative shift in pKa. Shifts are calculated as  $\Delta pK_a = pK_{a,PPol} - pK_{a,P}$ . a), b), and c) shows the  $\alpha$ -LA from different angles and viewpoints to provide a complete picture of the shifts observed. .... 122

**Figure 4.5:** Mapping the pKa shifts for the LYS protein showing the difference in pKa values between the protein in the presence of the polyanion and for the isolated protein simulations. The amino acid side chains undergoing a change in pKa are labeled. Blue indicates a positive shift in pKa, while red indicates a negative shift in pKa. Shifts are calculated as  $\Delta pK_a = pK_{a,PPol} - pK_{a,P}$ . a), b), and c) shows the lysozyme from different angles and viewpoints to provide a complete picture of the shifts observed. .... 125

**Figure 4.6:** A visualization of the changing coordinates of the polyelectrolyte with the proteins mapped into a single frame, allowing us to see all the points visited by the polyelectrolyte. The green polyanion beads indicate interactions with the lysozyme while the orange polyanion beads describe the interaction with the  $\alpha$ -lactalbumin. The trajectories were

visualized at the following pH regimes: a) 7.0 (LYS, attractive) b) 10.9 (LYS, pI) c) 13.0 (LYS, repulsive) d) 5.3 ( $\alpha$ -LA, pI) e) 8.0 ( $\alpha$ -LA, repulsive)..... 128

# **CHAPTER 1 : Introduction**

## **1.1 Why Molecular Simulation?**

Molecular simulations have been used to study properties of many-particle systems for several decades<sup>1</sup>. They have been applied as tools to test the validity of existing theories and provide a way to bridge the gap between theories and experiments. Molecular simulations are especially useful in studying systems that are difficult to study experimentally, either due to expense or lack of equipment that can effectively measure the desired quantities. For example, experimentally measuring the concentrations of a fluid mixture in a nanoporous material is extremely challenging, but using computer simulations to study these scenarios provides an alternative, efficient and affordable method to gain this knowledge<sup>2</sup> When studying reaction equilibrium, it is often difficult to distinguish metastable states from true equilibrium via experimentation<sup>3</sup>. In addition, simulations allow us to have precise control of different variables, eliminate uncertainties that arise from working with nano- and micro-scale systems, and offer a way to determine true equilibrium states<sup>2</sup>.

## **1.2 Monte Carlo Simulations**

In order for molecular simulations to be useful and applicable in solving real-world problems, they have to provide information that can be related to experimental data, such as average properties as opposed to instantaneous details. The majority of molecular simulations use classical statistical mechanics to describe the motion of particles, the laws of which are derived from quantum mechanics. One approach to conduct these simulations is by using Monte Carlo (MC) molecular modeling. MC methods are stochastic in nature and are based on

equilibrium statistical mechanics, generating states based on the Boltzmann probability distribution. There are several advantages to using MC methods: a) they are extremely effective in treating different thermodynamic ensembles, b) they can accurately predict thermodynamic properties, and c) they only require energies to generate the trajectories of atoms, to name a few. From statistical mechanics, any observable, mechanical quantity<sup>i</sup>  $\langle A \rangle$ , such as local density or potential energy, can be written as<sup>1</sup>:

$$\langle A \rangle = \frac{\int d\mathbf{r}^N \exp [-\beta U(\mathbf{r}^N)] A(\mathbf{r}^N)}{\int d\mathbf{r}^N \exp [-\beta U(\mathbf{r}^N)]}$$

where  $\mathbf{r}^N$  represents the coordinates of all  $N$  particles,  $\beta$  is  $1/kT$  (where  $k$  is the Boltzmann constant and  $T$  is the temperature), and  $U$  is the configurational energy of the system. Since it is generally not possible to analytically evaluate the integral  $\int d\mathbf{r}^N \exp [-\beta U(\mathbf{r}^N)]$  due to the high number of integrand variables, the Metropolis Monte Carlo scheme<sup>4</sup> was developed to sample the ratio of the two integrals in Equation (1.1). The Metropolis algorithm generates random configurations according to a probability distribution and then computes the average value of  $\langle A \rangle$ . In order to generate the random configurations, a Markov chain of states is constructed that allows a system to move from one configuration state to another without any memory of the previous states. The system changes configurations using different types of Monte Carlo moves, such as the displacement or rotation of single particles. At the end of each

---

<sup>i</sup> A ‘mechanical property’ in classical statistical mechanics is one that has a definite value for a particular molecular configuration,  $(\mathbf{r}^N)$ . Examples are energy, number of molecules and the radial distribution function. ‘Statistical properties’ such as entropy and free energy (thermodynamic potential), by contrast, depend on all possible configurations of the molecules.

attempt to create a new configuration, the proposed move is either accepted or rejected based on the Metropolis criterion<sup>1</sup>. For particle displacements or rotations, this is:

$$P_{acc} = \min[1, \exp(-\beta(U_2 - U_1))]$$

where  $U_1$  is the energy of the current state and  $U_2$  is the energy of the proposed state. Therefore, if  $U_2$  is less than  $U_1$ , the proposed move will always be accepted to help reach equilibrium faster. If  $U_2$  is greater than  $U_1$ , a random number,  $r$ , is generated and the proposed move is only accepted if  $P_{acc}$  is greater than  $r$ .

One of the many advantages of Monte Carlo is that we can use different ensembles to study different systems, depending on the properties we want to calculate and the properties that are already known to us. While the displacement and rotation moves are standard MC steps in all ensembles, additional MC moves are required when studying ensembles besides the canonical ensemble and different acceptance criteria have to be derived. In this dissertation, we use Monte Carlo techniques to study 3 different research agendas:

- the effect of fluid-wall interactions and molecule shape on the adsorption of molecules in carbon pores,
- the effect of confinement on the nitric oxide dimerization reaction in carbon pores such as slit-pores and nanotubes, and
- the importance of charge regulation on protein-polyelectrolyte complexation.

Following is a brief background for each system and a description of the Monte Carlo method used to study it. This chapter aims to only cover an abridged explanation of the problems in order to provide context for the methods used to study them; a more in-depth literature review

and background for each system is available in the introduction sections of Chapters 2, 3, and 4.

### **1.3 Research Agendas and Techniques used**

#### *1.3.1 Pressure Enhancement in Confined Fluids*

Recently, several experimental and simulation studies have found that phenomena that normally occur at extremely high pressures in a bulk phase can occur in nano-phases confined within porous materials at much lower bulk phase pressures, thus providing an alternative route to study high-pressure phenomena<sup>5-8</sup>. Our main concern is in studying the in-pore pressure tensor in carbon pores, particularly the tangential pressure which runs parallel to the pore walls, in order to gain a better understanding of how confinement can lead to high pressure effects in these pores. While several molecular simulations have studied the pressure tensor for one-site Lennard-Jones molecules<sup>5,9</sup>, relatively little effort has been made to study the pressure tensor for multi-site molecules that are often the subject of other simulation studies (eg. water, carbon dioxide etc.).

When studying the equilibrium properties for adsorption of fluid molecules, two main techniques are generally used, the Grand Canonical Monte Carlo (GCMC) method and the Gibbs Ensemble Monte Carlo (GEMC) method<sup>10</sup>. Both methods allow for the study of two phases without an interface. In GCMC, the chemical potential  $\mu$ , volume  $V$ , and temperature  $T$  are kept constant and the configuration inside the pore is determined by randomly creating and removing molecules. In GEMC, two simulation boxes are created and placed in equilibrium with each other; one box representing the bulk phase and the other box

representing the pore phase<sup>11</sup>. The total number of molecules  $N$ , the total volume of both simulation boxes  $V$ , and the temperature  $T$  are kept constant. Since the constant variables are the input variables for molecular simulations, it can be seen that neither of the above techniques allows us to define the bulk pressure as an input variable. Since the pressure of the bulk fluid is an easily measurable quantity in experiments, most experimental data such as adsorption isotherms are presented as functions of bulk pressure. Since the bulk pressure and temperature used in prior studies are known variables, we opt to use the Constant-Pressure Gibbs Ensemble (CP-GEMC) method which allows us to define these quantities as input variables<sup>10</sup>. In addition, the CP-GEMC method eliminates the need for us to calculate chemical potentials, making it easier to utilize for the reactive system studied in this dissertation. There are many similarities between GEMC and CP-GEMC, with both methods involving displacement, rotation, particle exchange moves (see Figure 1.1). However, while the volumes of both simulation boxes are allowed to change in order to keep the total volume constant in GEMC, the volume of the pore phase in CP-GEMC is fixed. The volume of the bulk phase is still allowed to change, thus enabling us to keep the pressure of the bulk phase constant and define it as an input variable.

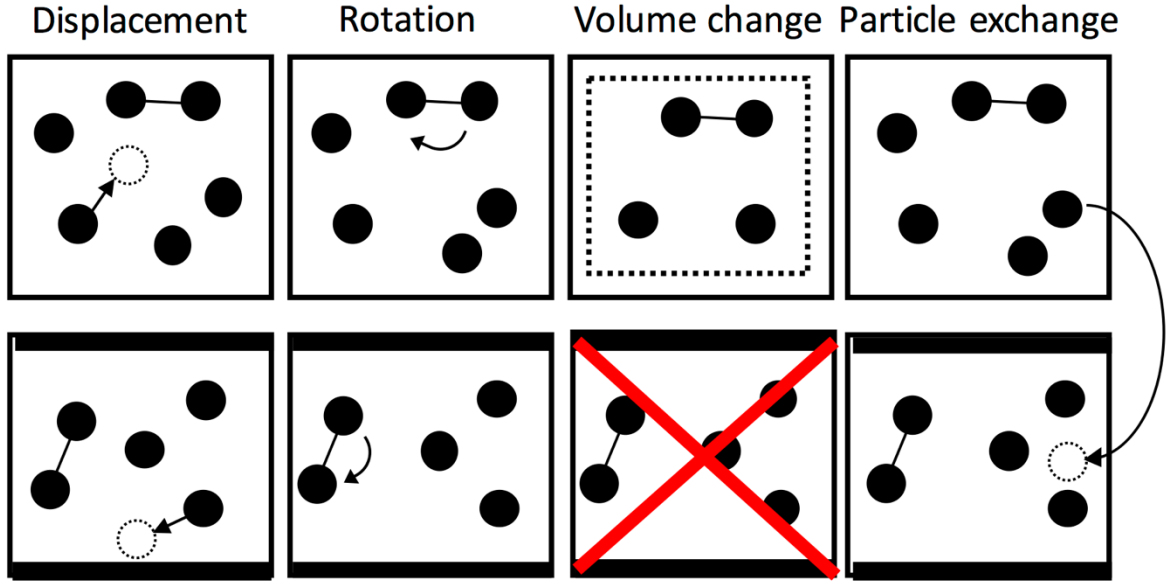


**Figure 1.1:** Monte Carlo moves associated with CP-GEMC.

So as to accurately calculate the acceptance criterion, the two phases are considered to be part of a larger system that has a constant volume. The acceptance criterion for the Monte Carlo moves associated with CP-GEMC are then calculated to be<sup>1,2,10</sup>:

- Displacement:  $P_{acc} = \min[1, \exp(-\beta(U_2 - U_1))]$
- Rotation:  $P_{acc} = \min[1, \exp(-\beta(U_2 - U_1))]$
- Particle exchange from bulk to pore:

$$P_{acc} = \min\left[1, \exp\left(-\beta(\delta U_{N_{B,i-1}} - \delta U_{N_{P,i+1}}) \times \frac{N_{B,i} V_P}{(N_{P,i+1}) V_B}\right)\right]$$

- Particle exchange from pore to bulk:

$$P_{acc} = \min\left[1, \exp\left(-\beta(\delta U_{N_{P,i-1}} - \delta U_{N_{B,i+1}}) \times \frac{N_{P,i} V_B}{(N_{B,i+1}) V_P}\right)\right]$$

- Volume change in the bulk phase:  $P_{acc} = \min\left[1, \exp\left(-\beta\left(\delta U_V - P\delta V_B - \frac{N}{\beta} \ln\left(\frac{V_{B,n}}{V_{B,o}}\right)\right)\right)\right]$

where  $N_{B,i}$  and  $N_{P,i}$  are the number of molecules of type  $i$  in the bulk and pore phase, respectively,  $\delta U$  is the energy change in the bulk or pore phase after a move,  $V_B$  is the volume of the bulk phase,  $V_P$  is the volume in the pore phase,  $V_{B,n}$  is the new volume of the bulk phase,  $V_{B,o}$  is the original volume of the bulk phase, and  $\delta V_B = V_{B,n} - V_{B,o}$ .

### *1.3.2. Nitric Oxide Dimerization Reaction*

Experiments have shown that chemical reactions which generally occur at extremely high pressures in the bulk phase, occur in the confined phase at much lower bulk pressures. The behavior of chemical reactions in pores is an important phenomenon to study for a multitude of reasons. For example, many different types of porous materials are used as catalyst supports to drive chemical reactions in industry. However, while some materials, such as zeolites, have been the subject of study for over 50 years, others such as carbon nanotubes, metal-organic framework (MOFs), and mesoporous carbons have been studied less intensively. In order to enhance catalyst design, it is important to understand the interactions occurring in these porous materials at the molecular level. In Chapter 3, we aim to understand how the nitric oxide dimerization reaction ( $2\text{NO} \leftrightarrow (\text{NO})_2$ ) is affected by confinement in carbon slit-shaped pores and carbon nanotubes.

The NO dimerization reaction is exothermic, thermodynamically driven and is important in atmospheric chemistry. It is also useful in controlling functions in living organisms, such as the regulation of blood pressure in the human body<sup>12</sup>. Furthermore, the study of this reaction in pores is important to pollution abatement because activated carbons are often utilized for the removal of nitrogen oxides from auto exhaust and industrial effluent

gas streams<sup>12,13</sup>. Experiments by Kaneko et al.<sup>14</sup> and Byl et al.<sup>15</sup> have shown the reaction conversion to reach almost 100% in both activated carbons and carbon nanotubes. Conversely, the reaction conversion is close to 0% in the bulk phase. A thorough understanding of the driving force behind this high reaction yield in the pores is still incomplete and this problem is further complicated by simulation studies struggling to replicate experimental data<sup>13,16</sup>. One explanation for the high conversion under confinement could lie in Le Chatelier's principle which states that if a dynamic equilibrium is changed by varying the conditions, the equilibrium will shift to counteract the change. Therefore, if the pressure increases, the confined phase should shift the reaction conversion towards the formation of (NO)<sub>2</sub> in order to reduce the number of moles. However, Kaneko et al. also studied the following reaction experimentally in activated carbon<sup>17</sup>:



The above reaction clearly results in an increase in the number of moles. However, experimental results showed an increase in yield for the above reaction in the pore phase as well. Therefore, it is clear that Le Chatelier's principle alone cannot be used to explain this phenomenon of increased conversion in pores and another explanation is required.

In order to calculate the reaction equilibrium, we use a technique developed by Smith and Triska<sup>18</sup> and Johnson et al.<sup>19,20</sup>, known as the Reactive Monte Carlo (RxMC) technique in conjunction with the CP-GEMC method mentioned earlier. In the RxMC technique, reaction equilibrium is simulated by adding forward and reverse reaction moves to the set of Monte Carlo moves discussed earlier. Each move involves either adding or deleting a molecule based on stoichiometry, but the total number of particles in the system are still the same. For example,

when an NO monomer is converted to an (NO)<sub>2</sub> dimer, two monomers are deleted and one dimer is added, keeping the total number of atoms unchanged. The acceptance criteria for the reactive moves for the NO dimerization reaction are<sup>2</sup>:

- Forward reaction:  $P_{\text{acc}} = \min\left[1, \exp\left(-\beta\delta U_{\text{F}} \times \frac{q_{(\text{NO})_2}}{q_{\text{NO}}^2} \times \frac{(N_{\text{NO}}(N_{\text{NO}}-1))}{(N_{(\text{NO})_2}+1)}\right)\right]$
- Reverse reaction:  $P_{\text{acc}} = \min\left[1, \exp\left(-\beta\delta U_{\text{R}} \times \frac{q_{\text{NO}}^2}{q_{(\text{NO})_2}} \times \frac{N_{(\text{NO})_2}}{(N_{\text{NO}}+1)(N_{\text{NO}}+2)}\right)\right]$

where  $q_{\text{NO}}$  and  $q_{(\text{NO})_2}$  are the molecular partition functions for NO and (NO)<sub>2</sub>. The equations for calculating the molecular partition functions are listed in Chapter 3.

### 1.3.3 Protein-Polyelectrolyte Complexation

In Chapter 4, we switch gears from studying adsorption and reaction in pores to examining molecular phenomena of complex fluids involving charged macromolecules such as proteins and polyelectrolytes. Protein-polyelectrolyte complexation is a topic of great interest to the food science community because this phenomenon is observed in the production of food products as well as pharmaceuticals and cosmetics<sup>21–23</sup>. In order to supplement the multiple experimental studies that have been conducted in this area, we aim to provide simulation data to further understand this complexation at the molecular level. Our main motivation behind this study is to understand why positively or negatively charged polyelectrolytes are seen forming stable complexes with like-charged proteins. There are currently two popular theories that aim to explain and identify the main driving force behind this phenomenon. One theory supports the assumption of so-called “charged patches” on the protein surface due to charge-dipole interactions<sup>24–29</sup>. According to this theory, the

polyelectrolyte is essentially only binding to these oppositely-charged patches. The other theory suggests the charge regulation mechanism to be the driving force for these attractions i.e. the attraction between like-charged particles is actually due to changes in the protonation state of the protein as a result of the electrostatic potential of the neighboring molecule<sup>30-32</sup>. While both charge-dipole interactions and charge-induced interactions contribute to the electrostatic free energy of complexation, we aim to use Monte Carlo simulations to calculate the change in protonation states (i.e. pKa shifts) and map them onto the protein surface to show that the charge-induced interaction is the more dominant factor. Further details on the two theories described above and the prior work done in this area can be found in Chapter 4.1.

In order to study the interactions between proteins and polyelectrolytes, we use the semi-grand canonical ensemble using the standard Metropolis Monte Carlo algorithm mentioned earlier to conduct displacement moves for the salt, counterions and polyanions<sup>33-35</sup>. In a regular canonical ensemble, the temperature, volume and total number of molecules at a fixed composition are kept constant. In our case, while the total number of molecules is kept constant, the charges on the particles are allowed to change to maintain an electroneutral simulation cell, leading to a varying composition of negatively and positively charged particles throughout the simulation, hence its description as a semi-grand ensemble. For example, when a titratable site is protonated, the charge of that site is increased by 1 while the charge on a mobile ion is decreased by 1. No new particles are added into the system and no particles are removed; the identities of the existing particles have simply been changed. In order to change the charges, a titration MC move is implemented in addition to the displacement moves. In this

move, a random titratable protein site undergoes protonation or deprotonation and is accepted with the following probability<sup>33</sup>:

$$P_{\text{acc}} = \min[1, \exp(-\beta(\delta U_{el} \pm [pH - pKa] \ln 10))] ]$$

where  $U_{el}$  is the change in total electrostatic energy and  $pKa$  is the intrinsic  $pKa$  value for the amino acid undergoing titration.

## 1.4 Scope of this dissertation

The above discussion has provided a brief introduction to the research problems we explore in this dissertation, and has demonstrated the need for Monte Carlo simulations to investigate these areas. At this point, the reader might find it useful to streamline the focus points for our dissertation. What are the key questions we hope to answer? To accomplish this, we identify the scope of this dissertation with the following questions:

1. How is the pressure tensor in pores affected when involving molecules with more than one interaction site?
2. How is the pressure tensor affected by changes in the fluid-wall interaction energies or changes in pore width?
3. How does confinement affect chemical reaction yield and what drives chemical reactions to reach higher conversions in pores at low bulk pressures?
4. What is the source of the discrepancy between experiments and previous simulations when studying the nitric oxide dimerization reaction?

5. How does this reaction conversion relate to the large magnitude of the tangential pressure tensor that has been observed in pores? Do mixtures affect the pressure tensor differently from pure components?
6. What is the dominant factor in protein-polyelectrolyte complexation when both have the same net charge: charge-dipole interactions (“charged patches”) or charge-induced interactions? Can observing pKa shifts and polyelectrolyte trajectories show any preferential hot spots on the protein surface, as suggested by the “charged-patch” theory?

This dissertation is arranged as follows. In Chapter 2, we consider the effects of fluid-wall interactions and molecular shape, important variables that have not yet been studied, on the pressure tensor in slit pores. In Chapter 3, we explore the prior experimental and computational work done for the dimerization of nitric oxide and conduct our own simulation study in both slit-shaped pores and carbon nanotubes. A source for the discrepancy between simulation and experimental results is investigated. In Chapter 4, we provide a more detailed background on the theory of protein-polyelectrolyte complexation and examine the driving forces for complexation when both molecules are similarly charged. Each of these chapters contains:

- an Introduction section providing a more in-depth background and literature review on the topic of interest,
- a Simulation Methods section outlining additional techniques used, such as *ab initio* quantum chemistry calculations and the Irving-Kirkwood method of calculating of the pressure tensor, along with the MC methods.

- a Results and Discussion section analyzing the data obtained.
- a Conclusion section summarizing the findings for each chapter.

In Chapter 5, all our findings are summarized and recommendations are presented for future work.

## 1.5 References

1. Frenkel, D. & Smit, B. *Understanding Molecular Simulations: from Algorithms to Applications*. (Academic Press, 2002).
2. Turner, C. H. Computer Simulation of Chemical Reactions in Porous Materials. Ph.D. Dissertation. (North Carolina State University, 2002).
3. Heath Turner, C. *et al.* Simulation of chemical reaction equilibria by the reaction ensemble Monte Carlo method: a review. *Mol. Simul.* **34**, 119–146 (2008).
4. Metropolis, N., Rosenbluth, A. W., Rosenbluth, M. N., Teller, A. H. & Teller, E. Equation of State Calculations by Fast Computing Machines. *J. Chem. Phys.* **21**, 1087–1092 (1953).
5. Long, Y. Pressure Tensor of Adsorbate in Nanoporous Materials: Molecular Simulation Studies. Ph.D. Dissertation. (North Carolina State University, 2012).
6. Sliwińska-Bartkowiak, M. Melting Behavior of Water in Cylindrical Pores: Carbon Nanotubes and Silica Glasses. *Phys. Chem. Chem. Phys.* 4909–4919 (2008).
7. Takaiwa, D., Hatano, K., Koga, K. & Tanaka, H. Phase Diagram of Water in Carbon Nanotubes. *Proc. Natl. Acad. Sci. U. S. A.* 39–43 (2008).
8. Matsuda, K., Hibi, T., Kadowai, H., Kataura, H. & Maniwa, Y. Water Dynamics inside Single-Wall Carbon Nanotubes: NMR Observations. *Phys. Rev. B* 73415 (2006).
9. Long, Y., Palmer, J. C., Coasne, B., Sliwinski-Bartkowiak, M. & Gubbins, K. E. Pressure enhancement in carbon nanopores: a major confinement effect. *Phys. Chem. Chem. Phys.* **13**, 17163 (2011).

10. McGrother, S. C. & Gubbins, K. E. Constant pressure Gibbs ensemble Monte Carlo simulations of adsorption into narrow pores. *Mol. Phys.* **97**, 955–965 (1999).
11. Panagiotopoulos, A. Z. Adsorption and capillary condensation of fluids in cylindrical pores by Monte Carlo simulation in the Gibbs ensemble. *Mol. Phys.* **62**, 701–719 (1987).
12. Lancaster, J. R. Nitric Oxide in Cells. *Am. Sci.* **80**, 248–259 (1992).
13. Turner, C. H., Johnson, J. K. & Gubbins, K. E. Effect of confinement on chemical reaction equilibria: The reactions  $2\text{NO} \rightleftharpoons (\text{NO})_2$  and  $\text{N}_2 + 3\text{H}_2 \rightleftharpoons 2\text{NH}_3$  in carbon micropores. *J. Chem. Phys.* **114**, 1851–1859 (2001).
14. Kaneko, K., Fukuzaki, N., Kakei, K., Suzuki, T. & Ozeki, S. Enhancement of nitric oxide dimerization by micropore fields of activated carbon fibers. *Langmuir* **5**, 960–965 (1989).
15. Byl, O., Kondratyuk, P. & Yates, J. T. Adsorption and Dimerization of NO Inside Single-Walled Carbon Nanotubes - An Infrared Spectroscopic Study. *J. Phys. Chem. B* **107**, 4277–4279 (2003).
16. Lisal, M., Brennan, J. K. & Smith, W. R. Chemical reaction equilibrium in nanoporous materials: NO dimerization reaction in carbon slit nanopores. *J. Chem. Phys.* **124**, 64712 (2006).
17. Nishi, Y., Suzuki, T. & Kaneko, K. Ambient Temperature Reduction of NO to N<sub>2</sub> in Ru-Tailored Carbon Subnanospace. *J. Phys. Chem. B* **101**, 1938–1939 (1997).
18. Smith, W. R. & Triska, B. The reaction ensemble method for the computer simulation of chemical and phase equilibria. I. Theory and basic examples. *J. Chem. Phys.* **100**,

- 3019–3027 (1994).
19. Karl Johnson, J. *Advances in Chemical Physics: Monte Carlo Methods in Chemical Physics*. **105**, (Wiley, 1999).
  20. Johnson, J. K., Panagiotopoulos, A. Z. & Gubbins, K. E. Reactive canonical Monte Carlo. *Mol. Phys.* **81**, 717–733 (1994).
  21. Steiner, E., Gastl, M. & Becker, T. Protein changes during malting and brewing with focus on haze and foam formation: A review. *European Food Research and Technology* **232**, 191–204 (2011).
  22. Chen, K. *et al.* Electrostatic selectivity in protein-nanoparticle interactions. *Biomacromolecules* **12**, 2552–2561 (2011).
  23. Egan, T., O’Riordan, D., O’Sullivan, M. & Jacquier, J. C. Cold-set whey protein microgels as pH modulated immobilisation matrices for charged bioactives. *Food Chem.* **156**, 197–203 (2014).
  24. De Kruif, C. G., Weinbreck, F. & De Vries, R. Complex coacervation of proteins and anionic polysaccharides. *Current Opinion in Colloid and Interface Science* **9**, 340–349 (2004).
  25. de Vries, R. & Cohen Stuart, M. Theory and simulations of macroion complexation. *Current Opinion in Colloid and Interface Science* **11**, 295–301 (2006).
  26. Yigit, C., Heyda, J. & Dzubiella, J. Charged patchy particle models in explicit salt: Ion distributions, electrostatic potentials, and effective interactions. *J. Chem. Phys.* **143**, (2015).
  27. Yigit, C., Heyda, J., Ballauff, M. & Dzubiella, J. Like-charged protein-polyelectrolyte

- complexation driven by charge patches. *J. Chem. Phys.* **143**, (2015).
28. de Vries, R. Monte Carlo simulations of flexible polyanions complexing with whey proteins at their isoelectric point. *J. Chem. Phys.* **120**, 3475–3481 (2004).
  29. De Vries, R., Weinbreck, F. & De Kruif, C. G. Theory of polyelectrolyte adsorption on heterogeneously charged surfaces applied to soluble protein-polyelectrolyte complexes. *J. Chem. Phys.* **118**, 4649–4659 (2003).
  30. da Silva, F. L. B. & Jönsson, B. Polyelectrolyte–protein complexation driven by charge regulation. *Soft Matter* **5**, 2862 (2009).
  31. Kirkwood, J. G. & Shumaker, J. B. Forces between protein molecules in solution arising from fluctuations in proton charge and configuration. **38**, 863–871 (1952).
  32. Biesheuvel, P. M. & Stuart, M. A. C. Electrostatic free energy of weakly charged macromolecules in solution and intermacromolecular complexes consisting of oppositely charged polymers. *Langmuir* **20**, 2785–2791 (2004).
  33. Teixeira, A. A. R., Lund, M. & Da Silva, F. L. B. Fast proton titration scheme for multiscale modeling of protein solutions. *J. Chem. Theory Comput.* **6**, 3259–3266 (2010).
  34. Lund, M. & Jönsson, B. On the Charge Regulation of Proteins. doi:10.1021/bi047630o
  35. Kesvatera, T., Jönsson, B., Thulin, E. & Linse, S. Ionization behavior of acidic residues in calbindin D(9k). *Proteins Struct. Funct. Genet.* **37**, 106–115 (1999).

## CHAPTER 2 : Pressure Enhancement in Confined Fluids: Effect of Molecular Shape and Fluid-Wall Interactions

### 2.1 Introduction

There is much experimental evidence that the molecules in a fluid or amorphous film adsorbed on a solid substrate can experience strong compression. Such compression has been observed by direct *in situ* experiments; examples include adsorption measurements of the area occupied by a molecule<sup>1</sup>, X-ray diffraction<sup>2</sup>, low energy electron diffraction<sup>3</sup> and microcalorimetry measurements<sup>4</sup>. This compression has also been observed in molecular simulations<sup>5-7</sup>. Such compression is particularly evident for solid substrates having a high surface atomic density, such as carbons. Compression can occur in both the  $z$ -direction, normal to the surface, and in the  $xy$  plane parallel to the surface. Molecular simulations show that the pressures in such films can be greatly enhanced over that of the bulk fluid phase, and that this enhancement is particularly large in the direction parallel to the surface of the substrate. For example, for an adsorbed film of Lennard-Jones argon molecules on a carbon substrate at 87.3 K (the normal boiling point of argon) and 1 bar bulk pressure, the tangential pressure in the adsorbed layer in contact with the surface is of the order 20,000 bar<sup>6</sup>, i.e. an enhancement of more than 4 orders of magnitude.

The pressure in such adsorbed films is a second order tensor,  $\mathbf{P}$ , with components  $P_{\alpha\beta}$  giving the force per unit area in the  $\beta$  direction acting on an element of area pointing in the  $\alpha$  direction. Provided that the film is not under strain, the off-diagonal elements vanish. Of the

three diagonal elements, for a planar surface the two pressures parallel to the surface are equal,  $P_{xx} = P_{yy} = P_T$ , the tangential pressure, while  $P_{zz} = P_N$  is the pressure normal to the surface. The condition of mechanical equilibrium<sup>8,9</sup> for such a film is  $\nabla \cdot \mathbf{P} = 0$ . A result of this condition is that the normal pressure,  $P_N$ , must be constant and independent of the distance  $z$  from the surface of the substrate.

The normal pressure exerts a force on the solid substrate that causes changes to the solid structure, and this change can be measured in diffraction experiments; provided that the Young's modulus is known, it is possible to estimate the normal pressure on the surface<sup>10</sup>. So far, however, no experimental method has been proposed to measure the tangential pressure in such films. On the other hand, both components of the local pressure tensor can be calculated in molecular simulations. A complication is that the tangential pressure at a point near a planar interface is not uniquely defined<sup>8,9,11</sup>. This is because the pressure results from forces between pairs (and triplets, etc., in some cases) of molecules, so that an operational decision has to be made as to how much of such forces acting on a surface element  $d\mathbf{S}$  are assigned to a particular point  $\mathbf{r}$  in space. Two such operational definitions of the local tangential pressure have been commonly used, that of Irving and Kirkwood (IK)<sup>12</sup>, and that due to Harasima (H)<sup>13</sup>. In this work we adopt the Irving-Kirkwood definition of the pressure tensor. We note that it is not unusual that properties do not have a unique definition at the nanoscale, where the length scale is of the order of the range of the intermolecular forces. The volume is a common example<sup>8</sup>.

The local normal and tangential components of the pressure tensor have been studied fairly extensively in recent years via molecular simulation for atomic liquids that experience van der Waals forces. For the planar gas-liquid interface for a Lennard-Jones (LJ) fluid near

its normal boiling point, the tangential pressure at the interface is predicted to be of the order of -50 bar, there being only a rather small difference between the local IK and H pressures<sup>9,14</sup>. It is this strong, negative tangential pressure that gives rise to the surface tension. By contrast, for a dense LJ fluid confined in a slit-shaped carbon pore of width  $H$ , with fluid-wall interactions described by Lorentz-Berthelot combining rules, the local tangential pressure acting on molecules near the pore wall is usually positive and can be as high as 20,000 - 60,000 bar, even when the bulk gas with which it is in equilibrium is at a pressure of only 1 bar<sup>5,6,15,16</sup>. This large pressure enhancement of 4 or 5 orders of magnitude is a result of tight packing near the walls.

While some partial understanding exists for the pressure tensor components for simple LJ-like fluids in pores of slit-, cylindrical and spherical geometry, very little is known about the pressures for fluids in pores when stronger interactions are involved, e.g. due to chemisorption or chemical reaction. That in some cases the tangential pressures can be even larger than those described above is suggested by several recent experimental and molecular simulation studies. First, when sulfur, an insulator at near ambient conditions, is adsorbed within carbon nanotubes of appropriate diameter (just wide enough to accommodate sulfur atoms) it is found to form a linear polymer chain that is metallic, as shown in experiments by Fujimori et al.<sup>17</sup> Bulk sulfur does form a three-dimensional metallic phase at pressures of almost 1 million bar<sup>18,19</sup>, suggesting that high tangential pressures may be present in the nanotube. Recent molecular simulations for the sulfur-CNT system by Addington et al.<sup>20</sup> find that the local tangential pressure acting on the confined sulfur atoms in the one-dimensional chain are of the order 7 million bar. In the calculations, these very high local pressures are

found to result from a combination of effects due to the chemical reaction of the sulfur atoms to form a covalently bonded chain, coupled with strong repulsive interactions with the pore walls. In a second example, two independent experimental studies<sup>21,22</sup> of nitric oxide confined within carbon pores of roughly one nanometer width showed 100% conversion to the nitric oxide dimer, (NO)<sub>2</sub>. Recently we have shown, through quantum mechanical calculations, that the dimer interacts strongly with the  $\pi$  electrons in the carbon substrate, and this chemisorption interaction leads to the surprisingly high conversion of monomer to dimer. Subsequent molecular dynamics simulations for this system show that this strong dimer-carbon interaction results in very high local tangential pressures, of the order of millions of bars.

In this work, we report a molecular simulation study to examine the effect on the pressure tensor in a slit pore of two variables that have so far received little or no attention: (a) the influence of non-spherical molecular shape, and (b) the influence of the relative strength of the attractive fluid-wall and fluid-fluid interactions for cases where the fluid-wall interaction is strongly attractive, as in chemisorption. We also study the effect of pore width on these unique systems. In the next section, we describe the model and methods used, followed by the results and discussion. Conclusions are presented in the last section.

## 2.2 Simulation Methods

We use the Constant Pressure Gibbs Ensemble to simulate a two-phase system<sup>23–25</sup> (see Figure 2.1). The pressure and temperature of the bulk phase is kept constant and periodic boundaries are maintained in all three directions. For the pore phase, the volume is kept constant, and periodic boundaries are maintained in the x and y directions. Particles are exchanged between the pore and bulk phase in order to maintain chemical equilibrium between

the two phases. Displacement, rotational, and particle exchange moves are conducted in both simulation boxes, while volume change moves are carried out in the bulk phase only.

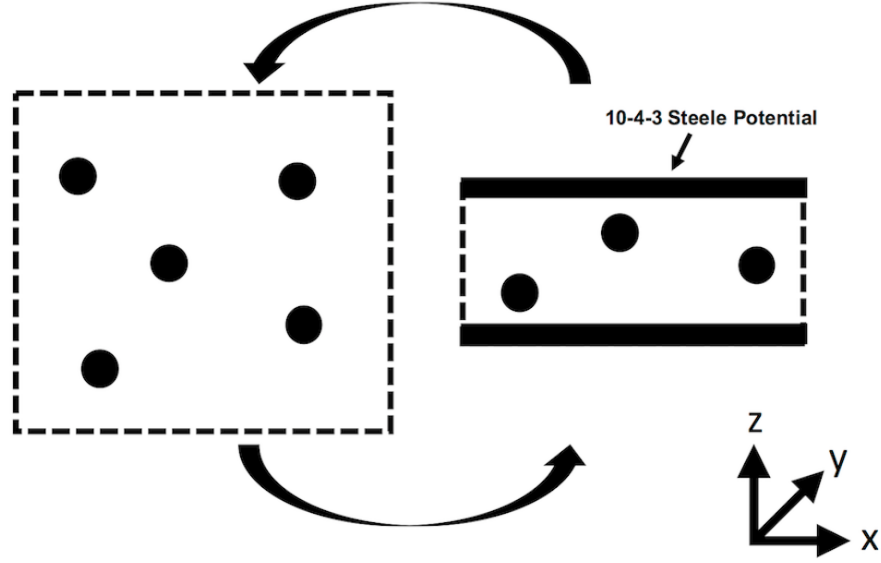


**Figure 2.1:** Constant-pressure Gibbs Ensemble Monte Carlo for narrow pores. Dotted lines signify periodic boundaries.

The carbon walls in the slit pore are simulated using the 10-4-3 Steele potential<sup>26,27</sup> for the fluid-wall ( $f_w$ ) interactions,

$$u_{f_w}(z) = 2\pi\rho_w\sigma_{f_w}^2\varepsilon_{f_w}\Delta\left[\frac{2}{5}\left(\frac{\sigma_{f_w}}{z}\right)^{10} - \left(\frac{\sigma_{f_w}}{z}\right)^4 - \left(\frac{\sigma_{f_w}^4}{3\Delta(z+0.61\Delta)^3}\right)\right] \quad (2.1)$$

where  $z$  is the distance of a fluid molecule from the wall,  $\rho_w$  is the solid density in atoms per unit volume,  $\sigma_{f_w}$  and  $\varepsilon_{f_w}$  are the usual size and energy parameters in the intermolecular potential energy, here taken to be the Lennard-Jones (12,6) model, and  $\Delta$  is the interlayer spacing between layers of solid atoms in the substrate. Equation (2.1) is obtained by integrating the fluid-wall pair interactions over the positions of atoms in the wall. Comparisons of results for

the adsorption properties using this (10,4,3) model with those for a fully atomistic wall<sup>28</sup> show that it is a good approximation provided that the fluid molecules are relatively large compared to the spacing of the wall atoms, and the temperature is not below 100 K; these conditions are well fulfilled for the model considered here.

The total number of molecules and temperature of the system were kept constant. We carried out all simulations at a temperature of 140 K, and maintained the pressure in the bulk phase at a constant value of 0.16 bar by changing the volume of the bulk phase periodically throughout our simulation.

### *2.2.1 Molecular Models*

Three different molecular geometries were studied. The models used for the monomer, dimer, and trimer are shown in Figure 2.2. The monomer was modelled as a 1-site Lennard-Jones (LJ) model with the following parameters:  $\sigma_{ff} = 0.31715$  nm and  $\epsilon_{ff}/k_B = 125.0$  K. The dimer was modelled as a 2-site Lennard-Jones model with each site having the same parameters as the monomer, and a bond length of 2.237 Å. The trimer was modeled using the same parameters as the dimer with a bond angle of 104°. The bonds between the particles in multi-site molecules were modelled as rigid bonds. The interactions between carbon atoms in the graphene sheet were modeled with the following LJ parameters<sup>26,27</sup>:  $\sigma_w = 0.34$  nm and  $\epsilon_w/k_B = 28.0$  K. The parameters for graphite in the 10-4-3 Steele potential are still  $\rho_w = 114$  nm<sup>-3</sup> and  $\Delta = 0.335$  nm.

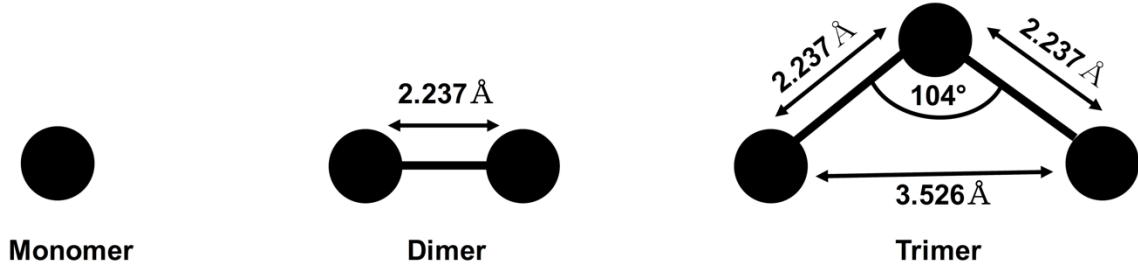


**Figure 2.2:** Different molecular geometries for the monomer, dimer, and trimer

The pore dimensions for the larger pore were  $50 \text{ \AA} \times 50 \text{ \AA} \times 15.9 \text{ \AA}$ , corresponding to a pore width (H) of approximately  $5\sigma$ . The smaller pore had the same dimensions in the x and y directions, with a pore width of  $9.5 \text{ \AA}$ , corresponding to approximately  $H = 3\sigma$ . In order to quantify the effect of the fluid-wall interactions on the pressure tensor, we calculated the ratio of fluid-wall interactions to fluid-fluid interactions, as given by the wetting parameter<sup>5</sup>,  $\alpha$ :

$$\alpha = \frac{\text{Fluid - Wall Interaction}}{\text{Fluid - Fluid Interaction}} = \rho_w \sigma_{fw}^2 \Delta \left( \frac{\epsilon_{fw}}{\epsilon_{ff}} \right) \quad (2.2)$$

where  $\rho_w$ ,  $\Delta$  and  $\epsilon_{ff}$  have the values given above, and the unlike parameters,  $\sigma_{fw}$  and  $\epsilon_{fw}$  remain to be specified. In previous studies of the pressure tensor for nano-phases confined within carbon pores it has usually been assumed that the interactions between the adsorbate molecules and the carbon atoms in the wall are of LJ form and can be approximated by the Lorentz-Berthelot (LB) combining rules<sup>29,30</sup> ( $\epsilon_{fw} = \sqrt{\epsilon_{ff} \epsilon_w}$  and  $\sigma_{fw} = (\sigma_{ff} + \sigma_w)/2$ ). If we make this assumption here we get  $\epsilon_{fw}/k_B = 59.16 \text{ K}$  and  $\sigma_{fw} = 0.329 \text{ nm}$ , and  $\alpha \approx 2.0$ . However, in this work we wish to examine the effect on the pressure tensor for stronger fluid-wall interactions, such as those that occur for weak chemisorption. For example, both nitric oxide, NO, and nitric oxide dimer,  $(NO)_2$ , interact more strongly with carbon walls than expected from the LB rules,

due to interactions with the  $\pi$  electrons in the carbon. Recent MP2 quantum mechanical calculations for these interactions correspond to values of the wetting parameters of 32.0 for NO/C and 42 for (NO)<sub>2</sub>/C (the latter value corresponds to one site in the dimer, which is treated using a two-site model).

We studied the effect of  $\alpha$  by varying the strength of the fluid-wall interactions while keeping the fluid-fluid interactions constant. For each pore width and molecular geometry, we conducted simulations for  $\alpha = 10$  and  $\alpha = 39$ . These correspond to approximately 5 times and 20 times the value estimated by the Lorentz-Berthelot mixing rules<sup>29,30</sup>, with the second value being representative of a weak chemical bond. In both cases, the fluid-wall interactions are stronger than the fluid-fluid interactions, enabling us to better observe confinement and pressure effects.

### 2.2.2 Pressure calculations

While the pressure in a bulk homogeneous phase is a scalar,  $P_{bulk}$ , the fluid in a confined pore is inhomogeneous, causing the in-pore pressure,  $\mathbf{P}(r)$ , to become a second-order tensor.<sup>5</sup> In a slit pore at equilibrium, the pressure tensor is diagonal. As mentioned earlier, one of the diagonal elements is the normal pressure,  $P_N$ , which acts perpendicular to the walls, and the other two are equal to the tangential pressure,  $P_T$ , which acts parallel to the pore wall in the  $xy$  plane (see Figure 2.3).

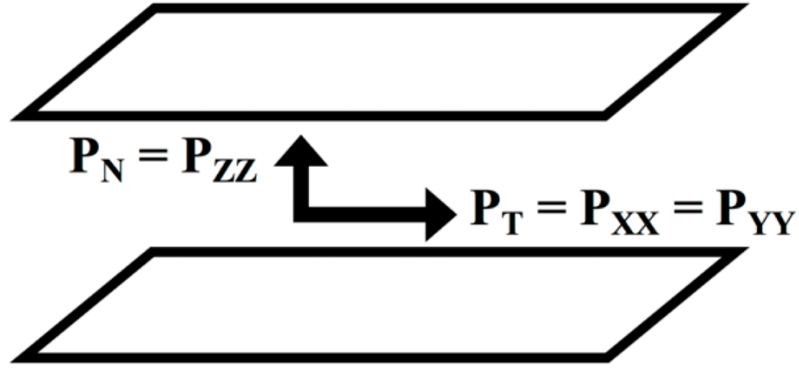


**Figure 2.3:** The normal and tangential pressure components in a slit pore.

The pressure tensor has two contributions: a kinetic contribution,  $\mathbf{P}_{kin}$ , and a configurational contribution,  $\mathbf{P}_{conf}$ . The kinetic contribution is a result of the convective momentum transport of molecules, and can be calculated using the ideal gas law:

$$\mathbf{P}_{kin} = \rho_{ad}(\mathbf{r})k_B T \mathbf{1} \quad (2.3)$$

where  $\rho_{ad}(\mathbf{r})$  is the number density of the adsorbate within the pore,  $k_B$  is the Boltzmann constant,  $T$  is the temperature, and  $\mathbf{1}$  is the second-order unit tensor.  $\mathbf{P}_{conf}$  arises from the interactions between the molecules and, in the case of spherical particles interacting in a purely pair-wise fashion,  $\mathbf{P}_{conf}$  can be derived from the microscopic law of momentum conservation (also known as the mechanical route)<sup>8</sup>:

$$\mathbf{P}_{conf} = -\frac{1}{2} \left\langle \sum_{i \neq j}^N \frac{du(r_{ij})}{dr_{ij}} \int_{C_{ij}} \delta(r - \tilde{l}) d\tilde{l} \right\rangle \quad (2.4)$$

Here,  $C_{ij}$  is an arbitrary contour from the center of mass position of particle  $i$ ,  $\mathbf{r}_i$ , to the center of mass position of particle  $j$ ,  $\mathbf{r}_j$ ,  $r_{ij} = |\mathbf{r}_j - \mathbf{r}_i|$  is the distance from  $\mathbf{r}_j$  to  $\mathbf{r}_i$ ,  $\delta$  is the Dirac delta-function and  $\langle \dots \rangle$  indicates an ensemble average. Due to the arbitrary nature of  $C_{ij}$ , the

configurational contribution is not uniquely defined, implying that there is no unique way of determining how the interactive forces between particles contribute to the local pressure tensor. The most widely-used method to calculate the contour integral,  $C_{ij}$ , is the Irving-Kirkwood method<sup>9,31</sup> which defines the integration path between two particles,  $i$  and  $j$ , to be a straight line along the vector  $\mathbf{r}_{ij}$  (see Figure 2.4).

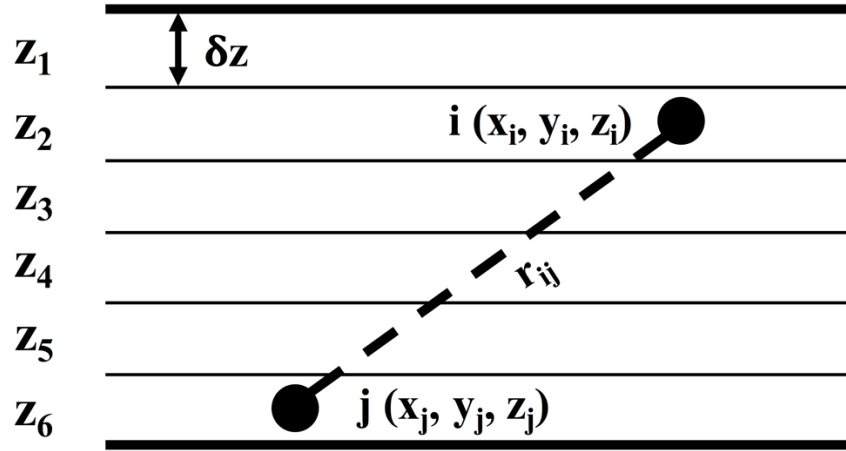


**Figure 2.4:** Example of the Irving-Kirkwood method where the pore is divided into bins of equal width. The interactive energy,  $u(\mathbf{r}_{ij})$ , contributes linearly to the bins between  $i$  and  $j$ . In this case,  $u(\mathbf{r}_{ij})$  would contribute to bins  $z_2$ ,  $z_3$ ,  $z_4$ ,  $z_5$ , and  $z_6$ .

With the Irving-Kirkwood definition, the pressure tensor can be expressed as

$$\mathbf{P}_{IK} = \mathbf{P}_{kin} + \mathbf{P}_{conf} = \rho(\mathbf{r})k_B T \mathbf{I} - \frac{1}{2} \left\langle \sum_{i \neq j}^N \frac{\mathbf{r}_{ij} \mathbf{r}_{ij}}{r_{ij}} \frac{du(\mathbf{r}_{ij})}{dr_{ij}} \int_0^1 \delta \lambda \delta(\mathbf{r}_i - \mathbf{r} + \lambda \mathbf{r}_{ij}) \right\rangle \quad (2.5)$$

We used a bin width of 0.1 Å to determine accurate pressure and density profiles.

## **2.3 Results and Discussion**

In this section, we present the results for Lennard-Jones monomers at different pore widths and wetting parameters, followed by the results for Lennard-Jones dimers and trimers. We then discuss the effect of varying these different parameters on the pressure tensor and packing inside the pores.

### 2.3.1 Lennard-Jones Monomers

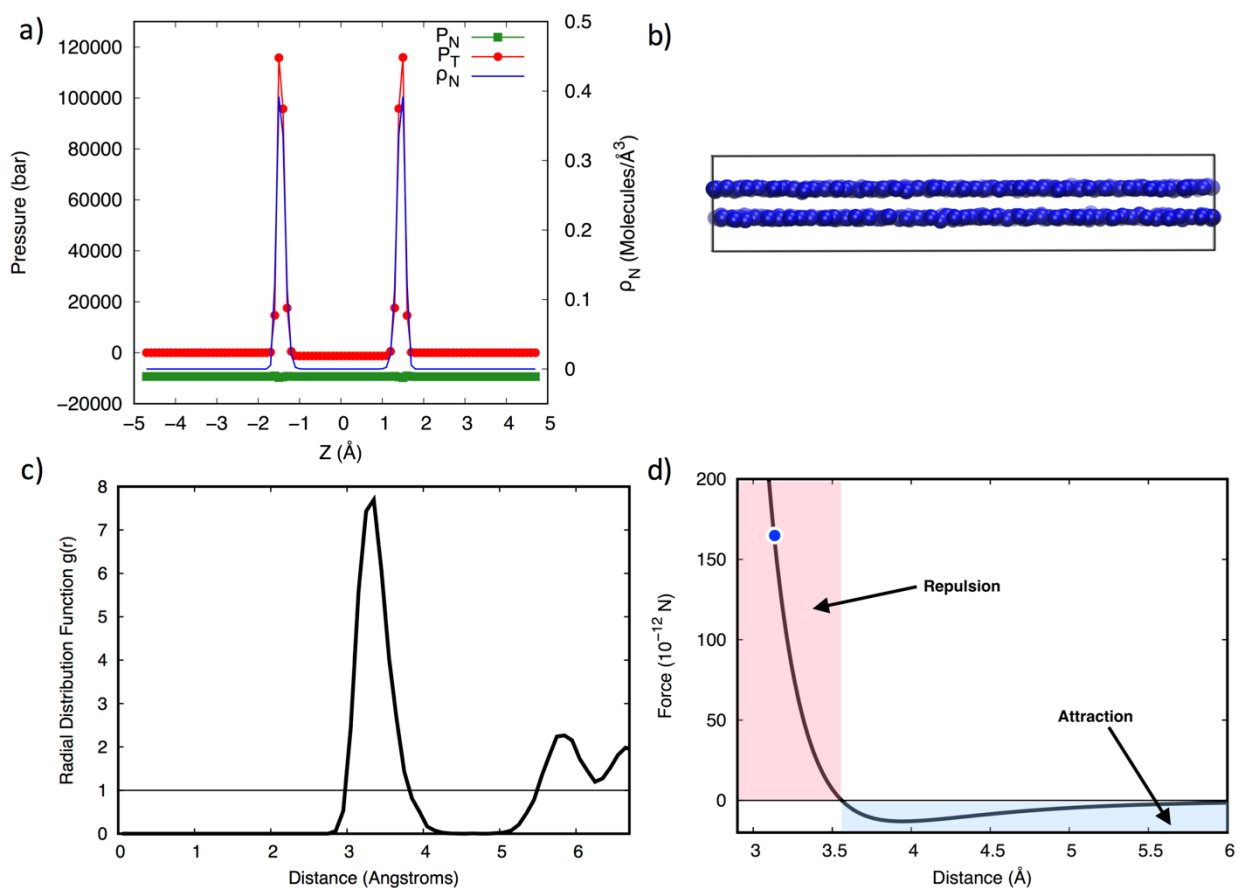


**Figure 2.5:** (a) Pressure and density profiles for the monomers in the pore of width  $3\sigma$ , at  $\alpha = 10$ . (b) Snapshot of the equilibrium configuration of the monomers in the  $3\sigma$  pore. (c) Radial distribution function in the  $xy$  plane for the contact layer in the  $3\sigma$  pore at  $\alpha = 10$ . (d) The intermolecular force between two monomer particles with the repulsive and attractive regions highlighted. The blue dot is the average nearest neighbor distance between two molecules in the  $xy$  plane for the  $3\sigma$  pore at  $\alpha = 10$ . In Fig. 2.5(a) the number densities plotted are the number of molecules,  $N_m$ , in a given bin of width  $0.1 \text{ \AA}$  divided by the bin volume.

In Figure 2.5(a), we show the pressure and number density profiles in the smaller ( $H = 3\sigma$ ) pore for  $\alpha=10$ .  $P_N$  is the normal pressure,  $P_T$  is the tangential pressure and  $\rho_N$  is the number density of molecules in a given bin centered about position  $z$ . The sharp peaks in the profiles are similar to the profile observed for LJ argon<sup>5,32</sup>, which is expected since both are single-site Lennard-Jones molecules. However, for LJ argon in a slit pore with (10,4,3) walls of width  $H = 3\sigma$  at 87.3 K and 1 atm. bulk pressure, the peak tangential pressure was found to be about 20,000 bar<sup>32</sup>, as compared to about 120,000 bar observed here. The primary reason for this much smaller peak tangential pressure in the case of LJ argon is that the wetting parameter for that system is much smaller,  $\alpha = 2.14$ , than that studied here,  $\alpha = 10$ . Due to the small size of the pore, only two layers of monomers fit into the pore and thus the layers interact directly with the pore wall (see Figure 2.5(b). The density profile peaks at 0.39 monomers/ $\text{\AA}^3$  at the same locations as the tangential pressure profile peaks, establishing a direct correlation between the two. The enhancement in the tangential pressure can therefore be attributed to the higher density of monomers near the wall, which results in the monomers being closer to each other and causing repulsive forces in the direction parallel to the wall. The radial distribution function,  $g(r)$ , of the bottom layer in the  $xy$  plane is shown in Figure 2.5(c). The first and largest peak identifies the most probable distance of a nearest neighbor monomer to be 3.35  $\text{\AA}$ . At this distance, the monomers are in the steeply repulsive region of the intermolecular pair force, as shown in the intermolecular force plot in Figure 2.5(d). The intermolecular pair force plot shows that any monomer that has a separation distance of less than 3.56  $\text{\AA}$  from another monomer would experience repulsive forces, leading to positive tangential pressures. The closer the molecules are packed, the larger the lateral repulsion forces, and the higher the

tangential pressures. The normal pressure is relatively constant throughout the width of the pore, satisfying the condition of hydrostatic equilibrium.

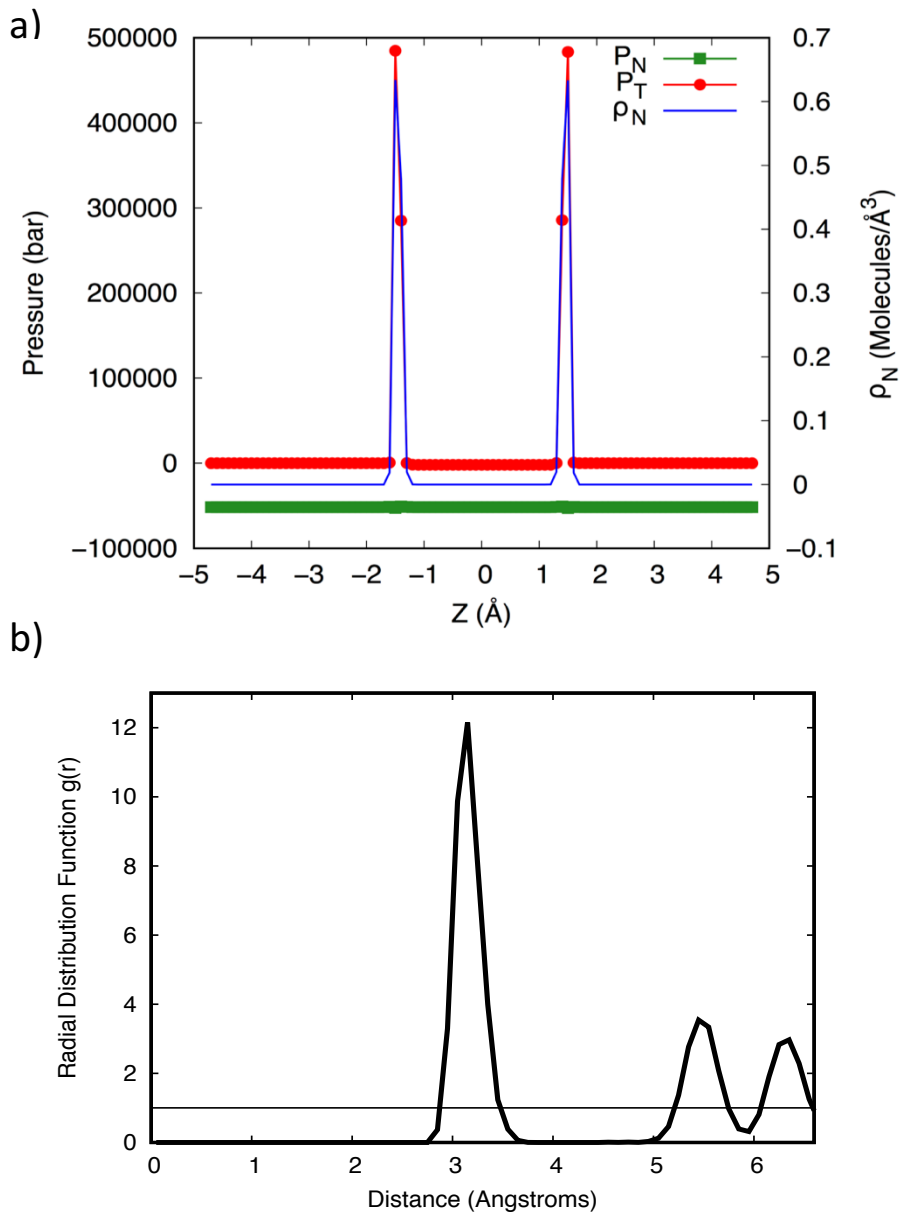


**Figure 2.6:** (a) Pressure and density profiles for the monomers in the  $3\sigma$  pore, at  $\alpha = 39$  (b) In-plane radial distribution function for the contact layer in the  $3\sigma$  pore at  $\alpha = 39$ .

In Figure 2.6(a) the pressure and density profiles for the smaller ( $H = 3\sigma$ ) pore for  $\alpha = 39$  are shown. The density profile shows that there are still only two molecular layers in the pore, with each layer now having a number density of  $0.63 \text{ monomers}/\text{\AA}^3$  in the bin corresponding to the center of the adsorbed layer. The tangential pressure continues to follow the same profile as the density, and has a peak value of almost 500,000 bar. The increase in the peak value is due to tighter packing of the monomers near the wall, as the stronger fluid-wall attraction compensates for the more repulsive fluid-fluid interaction at the higher density. The radial distribution function in Figure 2.6(b) identifies the most probable nearest neighbor separation distance to be  $3.15 \text{ \AA}$ , almost  $0.2 \text{ \AA}$  shorter than the probable distance in the  $H=3\sigma$  pore at  $\alpha = 10$ .

In Figure 2.7(a) are shown the pressure and density profiles in the larger ( $H = 5\sigma$ ) pore for  $\alpha = 10$ . At this pore width, the pore can accommodate 4 adsorbed layers – 2 layers close to the pore walls, and 2 layers near the center of the pore that interact more weakly with the wall, as shown in Figure 2.7(b). Once again, there is a strong correlation between the density and the tangential pressures, with the layers closest to the walls exhibiting both a high density of monomers and high tangential pressures. The density peaks to about  $0.43 \text{ monomers}/\text{\AA}^3$  in the contact layers and  $0.1$  in the middle layers while the tangential pressure peaks to about 160,000 bar in the contact layers. The inner layers closer to the center of the pore exhibit a lower but wider peak in the density, indicating less alignment and a smaller number of monomers, leading to smaller peaks in the tangential pressure. The in-plane radial distribution function of the contact layers (Figure 2.7(c)) identifies the highest probability of a nearest neighbor monomer to be around  $3.25 \text{ \AA}$ , well within the repulsive region of the potential.

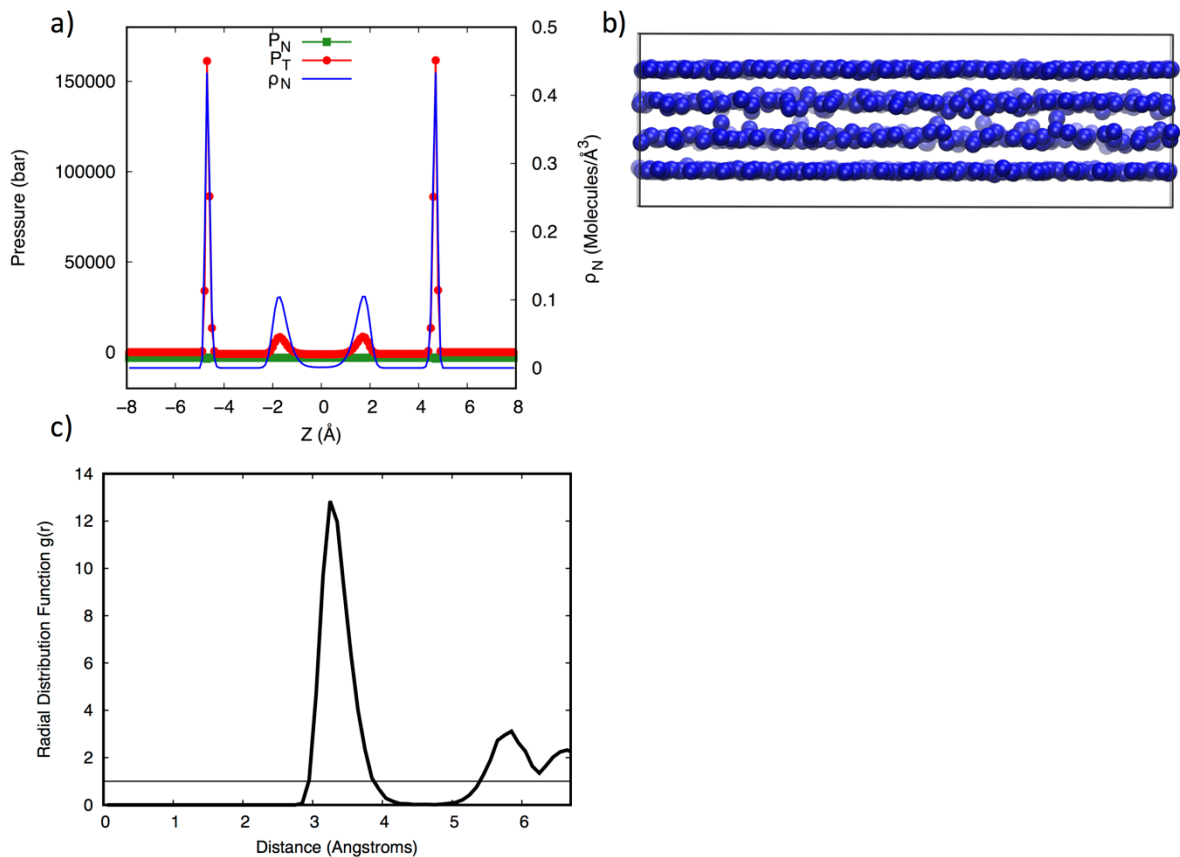


**Figure 2.7:** (a): Pressure and density profiles for the monomers in the pore of width  $5\sigma$  pore, at  $\alpha = 10$ ; (b) Snapshot of the equilibrium configuration of the monomers in the  $5\sigma$  pore; (c) In-plane radial distribution function in the contact layer in the  $5\sigma$  pore at  $\alpha = 10$ .

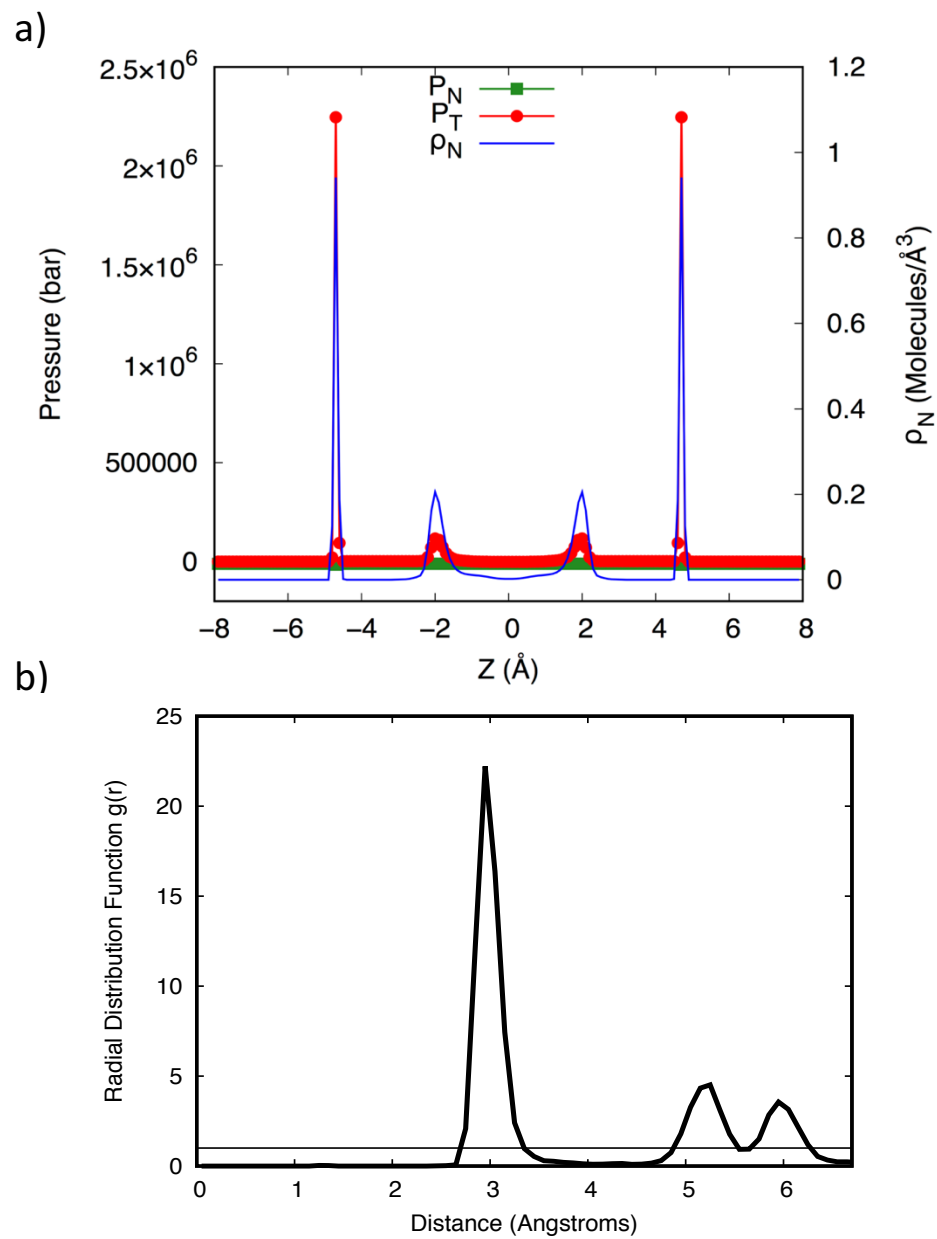


**Figure 2.8:** (a) Pressure and density profiles for the monomers in the pore of width  $5\sigma$ , at  $\alpha = 39$ ; (b) In-plane radial distribution function for the contact layer of monomers in the  $5\sigma$  pore at  $\alpha = 39$ .

In Figure 2.8(a), the pressure and density profiles are shown for the monomers in the  $5\sigma$  pore at  $\alpha = 39$ . The tangential pressure peaks to a considerably higher magnitude of around 2.3 million bar. Due to the stronger fluid-wall interactions and the larger pore width, a larger number of monomers are forced into the pore, thus increasing the density of monomers in the outer contact layers to over  $0.94 \text{ monomers}/\text{\AA}^3$ . This causes the tangential pressure to be significantly higher, due to the higher repulsive forces between the monomers within the layers. Figure 2.8(b) shows the in-plane radial distribution function plot for the monomers in the outer contact layer of the large pore at  $\alpha = 39$ . The highest probability of finding another monomer is at a separation distance of around  $2.95 \text{ \AA}$ , corresponding to very strong repulsion between neighbors.

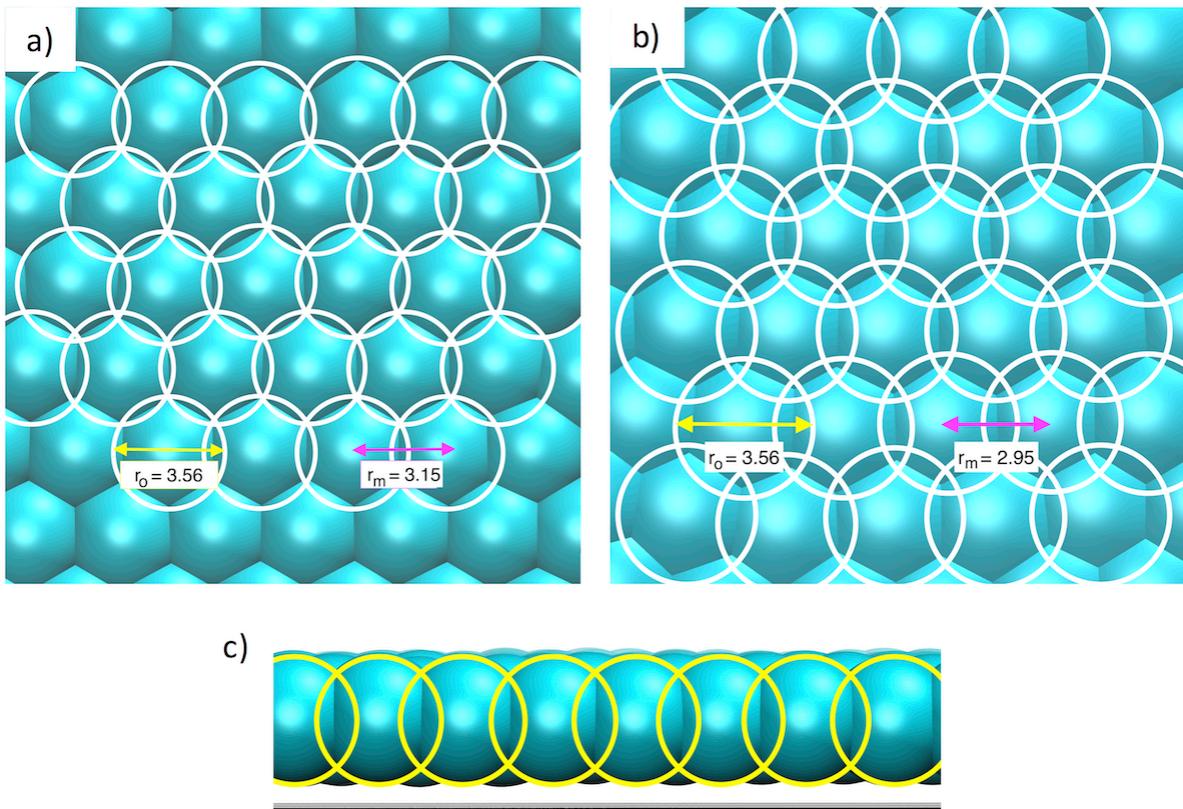


**Figure 2.9:** Snapshots of simulations, showing compression of the adsorbed contact layer next to the pore wall in  $xy$  plane for (a)  $r_{xy} = 3.15$  and (b)  $r_{xy} = 2.95$ , respectively. (c) Lateral compression in the adsorbed layer

Figures 2.9(a) and 2.9(b) above show typical molecular configurations of the contact layer, showing compression of the adsorbed monomer layer in the  $xy$  plane for  $r_{xy}$  values of 3.15 Å and 2.95 Å (represented as  $r_m$  in the figure), which are the mean separation distances in the  $xy$  plane between the centers of nearest neighbor molecules. The distance  $r_o$  is the separation distance between nearest neighbors when the pair force is zero, i.e. when the attractive dispersion and repulsive overlap forces are in balance. This is the case of no compression, and is very close to the average nearest neighbor separation in the bulk dense liquid at low pressure. Any separation distance less than  $r_o$  would result in repulsion between the molecules. As demonstrated in the figure, smaller separation distances would result in stronger compression and repulsion, leading to higher tangential pressures. Figure 2.9(c) shows the compression of the adsorbed layer in the lateral direction, and highlights the compression of the monomers in the tangential direction.

### 2.3.2 Lennard-Jones Dimers

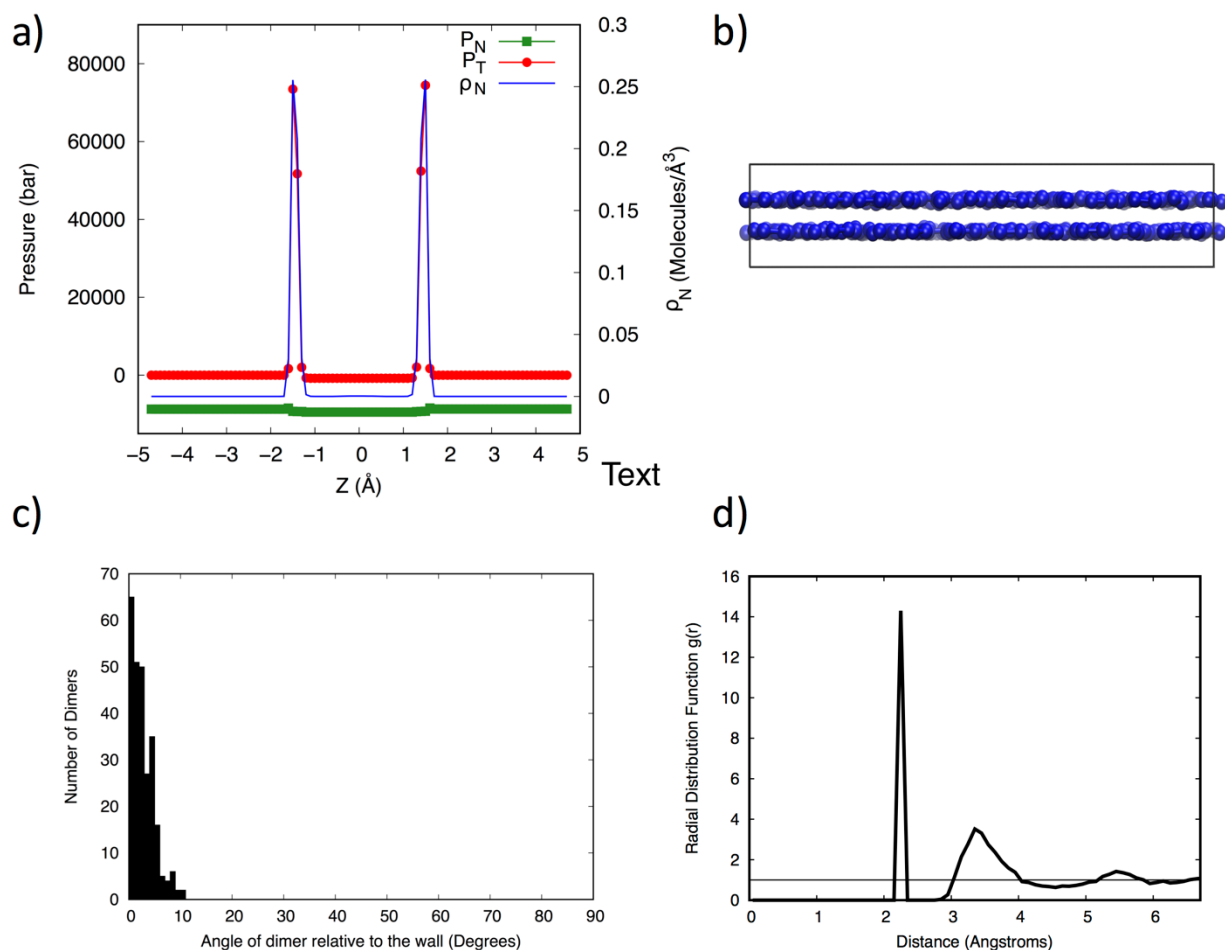


**Figure 2.10:** (a) Pressure and density profiles for the dimers in the pore of width  $3\sigma$ , at  $\alpha = 10$ ; (b) Snapshot of the equilibrium configuration of the dimers in the  $3\sigma$  pore at  $\alpha = 10$ ; (c) Histogram showing the distribution of the angles of the dimers relative to the pore wall; (d) In-plane radial distribution function for the dimer sites in the  $3\sigma$  pore, at  $\alpha = 10$ .

The pressure and molecular density profile for the dimers in the small pore at  $\alpha = 10$  are shown in Figure 2.10(a). The normal pressure is not constant, likely due to the rigid dimer

bonds that result in freezing in the small pore and the formation of a glassy or solid phase. In such cases, the condition of hydrostatic equilibrium no longer stands and the normal pressure can vary. There are only two molecular layers in the pore with a molecular density of 0.26 dimers/ $\text{\AA}^3$  in each layer and the tangential pressure peaks to almost 75,000 bar. It should be noted that a density of 0.26 dimers/ $\text{\AA}^3$  corresponds to a higher density of monomers/ $\text{\AA}^3$  since each dimer consists of two monomers. Because the dimers can orient themselves in different ways, there is now an additional degree of freedom in our system. The dimers can lie flat against the wall, forming separate linear layers like the monomers, which leads to the observed sharp peaks in the tangential pressure profile. They can, however, also rotate in different directions in the  $xz$  and  $yz$  planes, which would lead to broad shoulders arising from the sharp peaks. Since the dimers in the small pore are lying flat against the wall at  $\alpha = 10$  (see Figure 2.10(b)), the tangential pressure exhibits sharp peaks as observed for the monomers. A histogram of the angles of the dimers relative to the pore wall is shown in Figure 2.10(c). An angle of 0 degrees corresponds to a dimer lying flat against the pore wall, while an angle of 90 degrees indicates a dimer oriented perpendicular to the wall. The results show that all of the dimers lay at angles between 0 and 10 degrees with the wall, with the majority of them being very close to 0 degrees, showing that the dimers tend to lie flat against the wall, maximizing the favorable dimer-wall interaction. The site-site radial distribution function,  $g(r)$ , is shown in Figure 2.10(d). The first peak corresponds to the dimer bond length of 2.25  $\text{\AA}$  while the second peak shows that the most probable distance between nearest neighbor dimer sites is about 3.35  $\text{\AA}$ , which is in the repulsive region of the site-site potential (see Figure 2.5(d)).

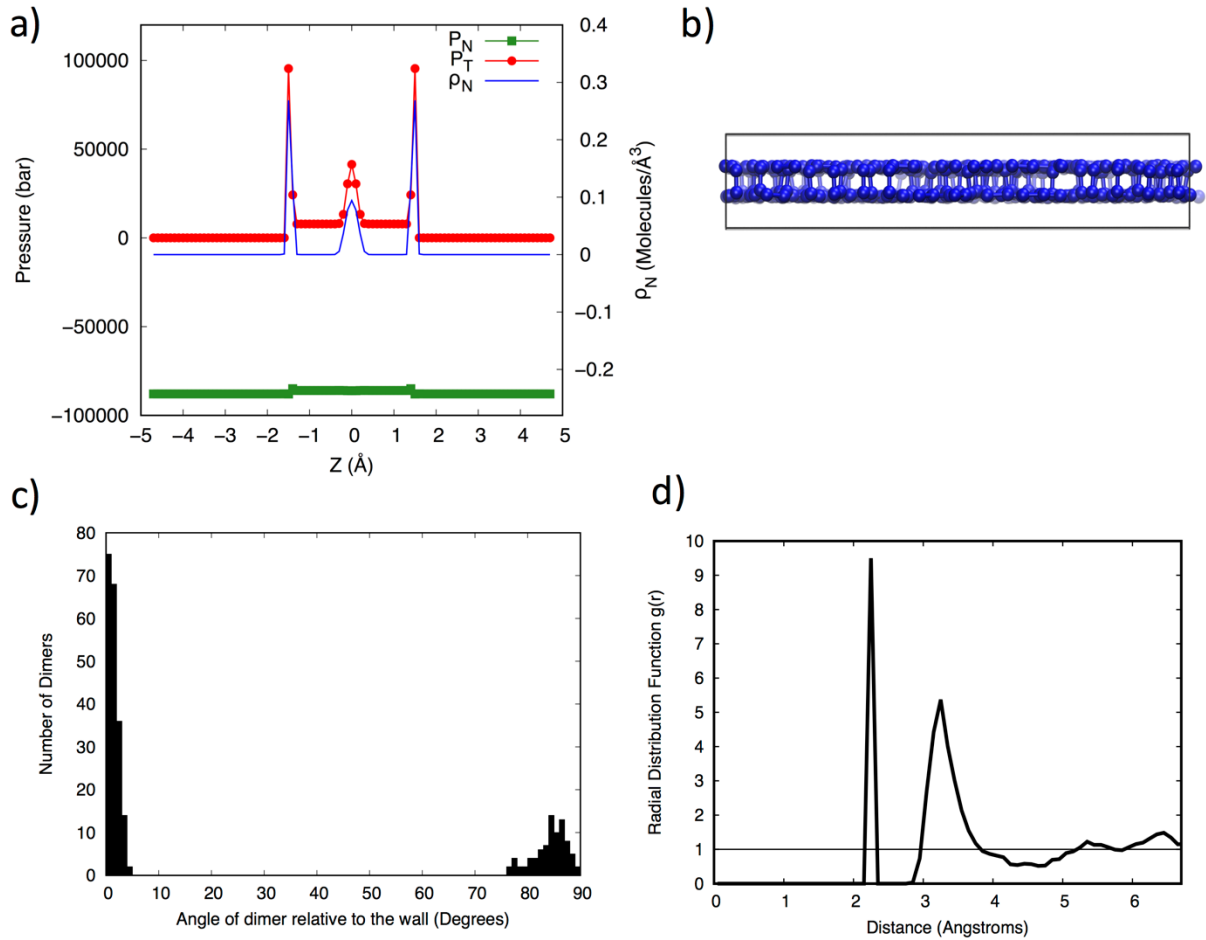


**Figure 2.11:** (a) Pressure and density profiles for the dimers in the pore of width  $3\sigma$ ,  $\alpha = 39$ ; (b) Snapshot of the equilibrium configuration of the dimers in the  $3\sigma$  pore,  $\alpha = 39$ ; (c) Histogram of the distribution of angles of the dimers relative to the pore wall; (d) In-plane radial distribution function for dimer sites in the  $3\sigma$  pore,  $\alpha = 39$ .

The pressure profiles for the dimers in the small pore at  $\alpha = 39$  are shown in Figure 2.11(a). The shape of the tangential pressure profile differs from the profiles observed so far. The normal pressure is again not constant, which is expected because a higher  $\alpha$  would enhance

any freezing phenomenon that was observed at the lower  $\alpha$ . The normal pressure is also very large in magnitude and extremely negative, indicating a strong attractive force within the dimer layers and between the fluid and the pore wall. A sharp peak in the tangential pressure is still seen close to the pore walls, with a maximum of around 95,000 bar, but there is also a smaller peak near the center of the pore. These peaks in the tangential pressure continue to correspond to maxima in the density profile, which peaks to about 0.27 dimers/ $\text{\AA}^3$  in the contact layers and 0.1 dimers/ $\text{\AA}^3$  in the center. We also see a higher tangential pressure in the region between these peaks (between -1  $\text{\AA}$  and 1  $\text{\AA}$ ), due to the close proximity of the center and contact layers, which leads to higher repulsive forces in that region. A snapshot of the pore in Figure 2.11(b) shows that a significant number of dimers are now aligning themselves vertically in the pore, with one site in each of the two layers so as to maximize their interaction with the pore walls. The histogram of the angles in Figure 2.11(c) also identifies a cluster of dimers in the pore that have an angle close to 90 degrees, indicating a vertical alignment in the pore for these dimers. The other dimers have an angle of less than 10 degrees, indicating that they're lying flat against the wall. The radial distribution function in Figure 2.11(d) shows the most probable distance between nearest dimer sites to be 3.25  $\text{\AA}$ .

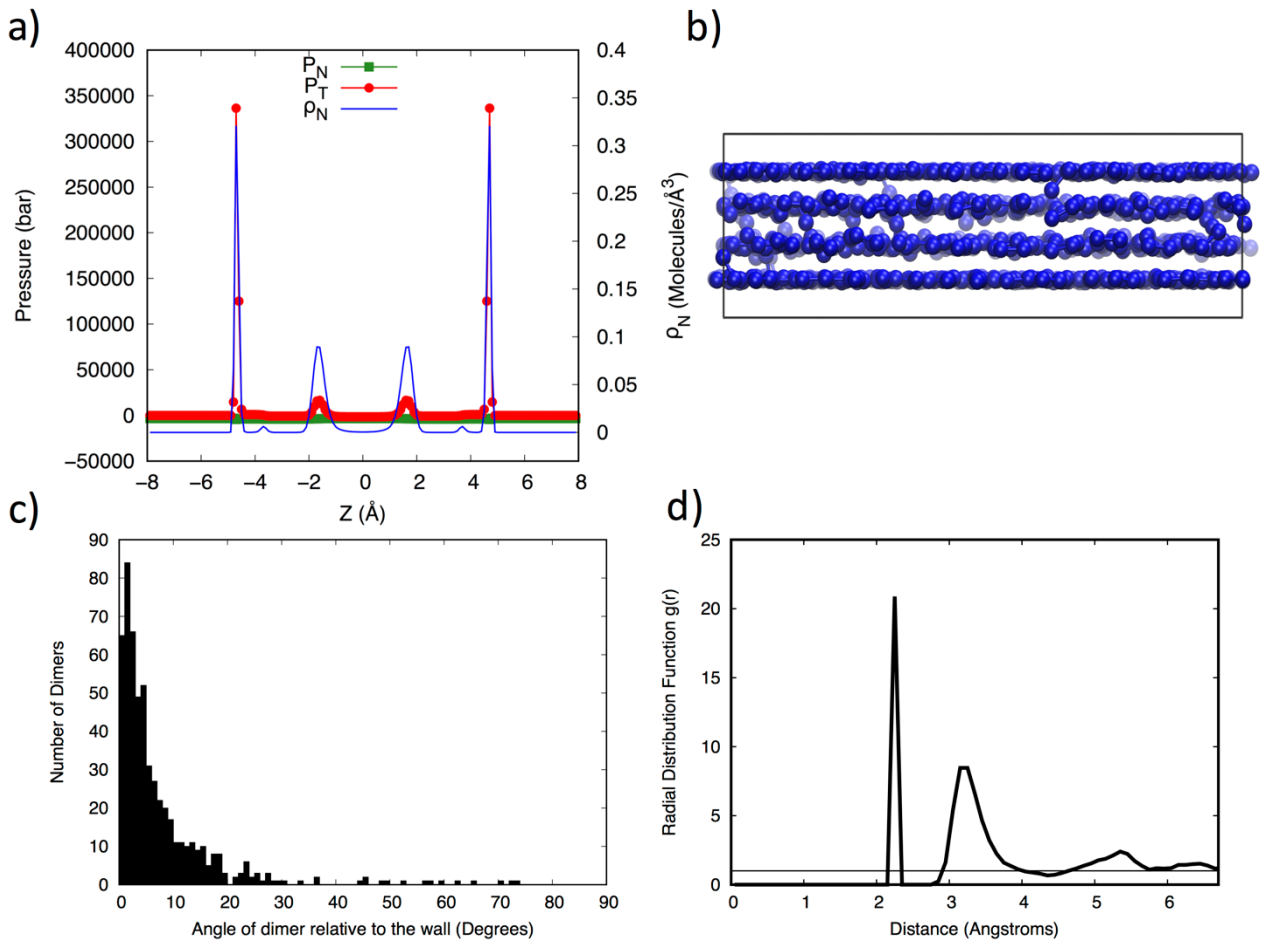


**Figure 2.12:** (a) Pressure and density profiles for the dimers in the  $5\sigma$  pore, at  $\alpha = 10$ ; (b) Snapshot of the equilibrium configuration of the dimers in the  $5\sigma$  pore,  $\alpha = 10$ ; (c) Histogram of the angles of the dimers relative to the pore wall; (d) In-plane radial distribution function for the dimer sites in the  $5\sigma$  pore,  $\alpha = 10$ .

The density and pressure profiles for the dimers in the large pore ( $H = 5\sigma$ ) at  $\alpha = 10$  are shown in Figure 2.12(a). With four separate layers, the majority of the dimers still gravitate towards the pore walls and the tangential pressure peaks to a maximum of 336,000 bar. The

normal pressure is constant due to the larger pore width, which makes it more difficult for freezing to occur and maintains the condition of hydrostatic equilibrium. The dimer number density in the contact layers is almost 0.33 dimers/Å<sup>3</sup> while the density in the center layers peaks to a little less than 0.1 dimers/Å<sup>3</sup>. Figure 2.12(b) shows that in the contact layers the molecules lie parallel to the wall, while the center layers have a less rigid structure. The histogram of the relative angles in Figure 2.12(c) also confirms a wider distribution of angles in the larger pore, with the majority of dimers oriented between 0 - 30 degrees, and a small number of dimers with a wider range of orientations. From the radial distribution function in Figure 2.12(d)), it is seen that the most probable distance between nearest neighbor dimer sites is about 3.25 Å, high in the repulsive region of the pair force.

The profiles for the dimers in the larger 5σ pore for α = 39 are shown in Figure 2.13(a). The tangential pressure exhibits a maximum of about 2.6 million bar with a molecular density of 0.545 dimers/Å<sup>3</sup> in each of the contact layers. The dimers in these contact layers are in extremely close proximity with each other as seen in the radial distribution function (Figure 2.13(d)), which shows that the most probable distance between nearest neighbor dimer sites is only 2.95 Å, very high in the repulsive region of the pair force. Along with the extremely high tangential pressures, slight broad shoulders are also observed in the tangential pressure profile. This is due to a larger number of dimers having a wider distribution of orientations relative to the wall, as can be seen in Figure 2.13(b) and 2.13(c). The histogram of the angles in Figure 2.13(c) also shows a wide distribution, with more dimers being rotated between 50- 80 degrees, along with a significant number still lying flat against the wall.

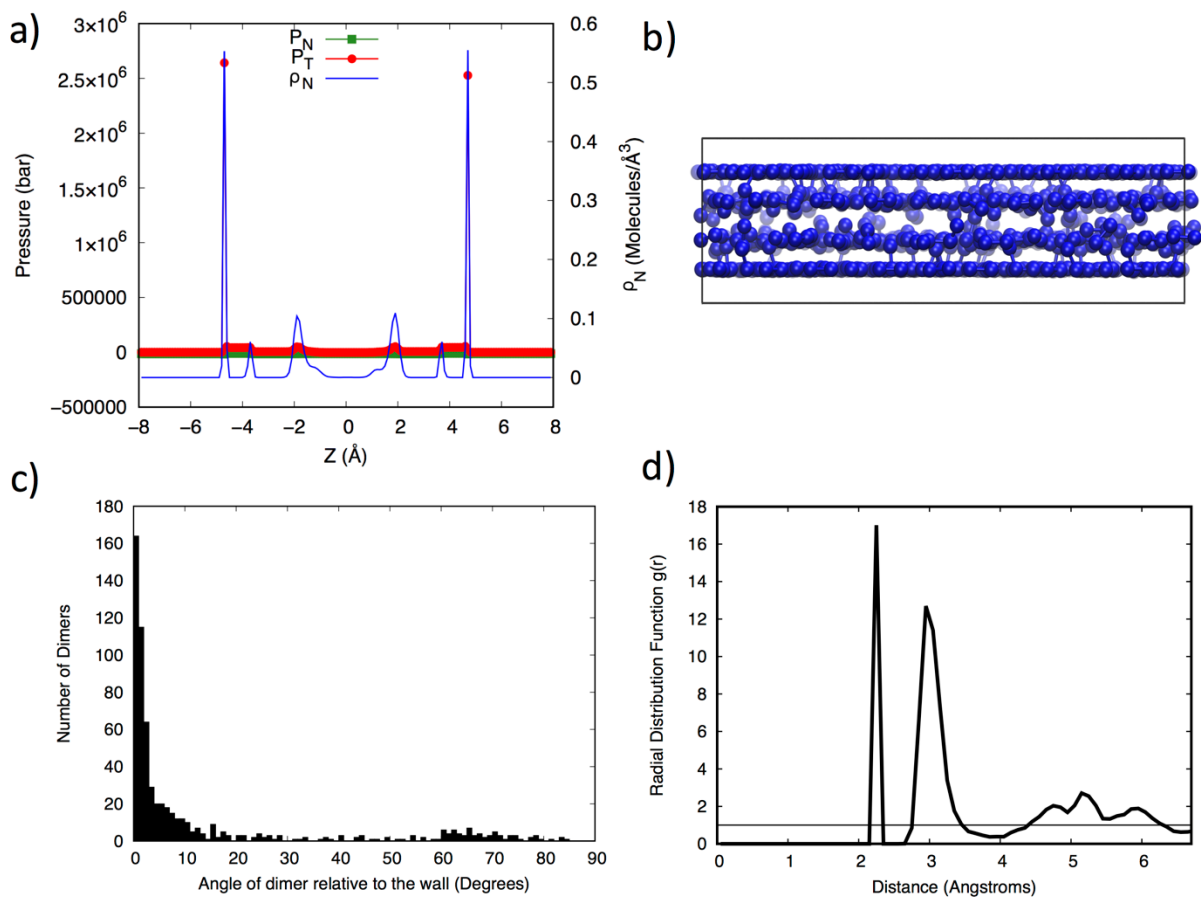


**Figure 2.13:** (a) Pressure and density profiles for the dimers in a pore width of  $5\sigma$ , at  $\alpha = 39$ ; (b) Snapshot of the equilibrium configuration of the monomers in the  $5\sigma$  pore,  $\alpha = 39$ ; (c) Histogram of the angles of the dimers relative to the pore wall; (d) In-plane radial distribution function for the dimer sites in the  $5\sigma$  pore,  $\alpha = 39$ .

### 2.3.3 Lennard-Jones Trimers

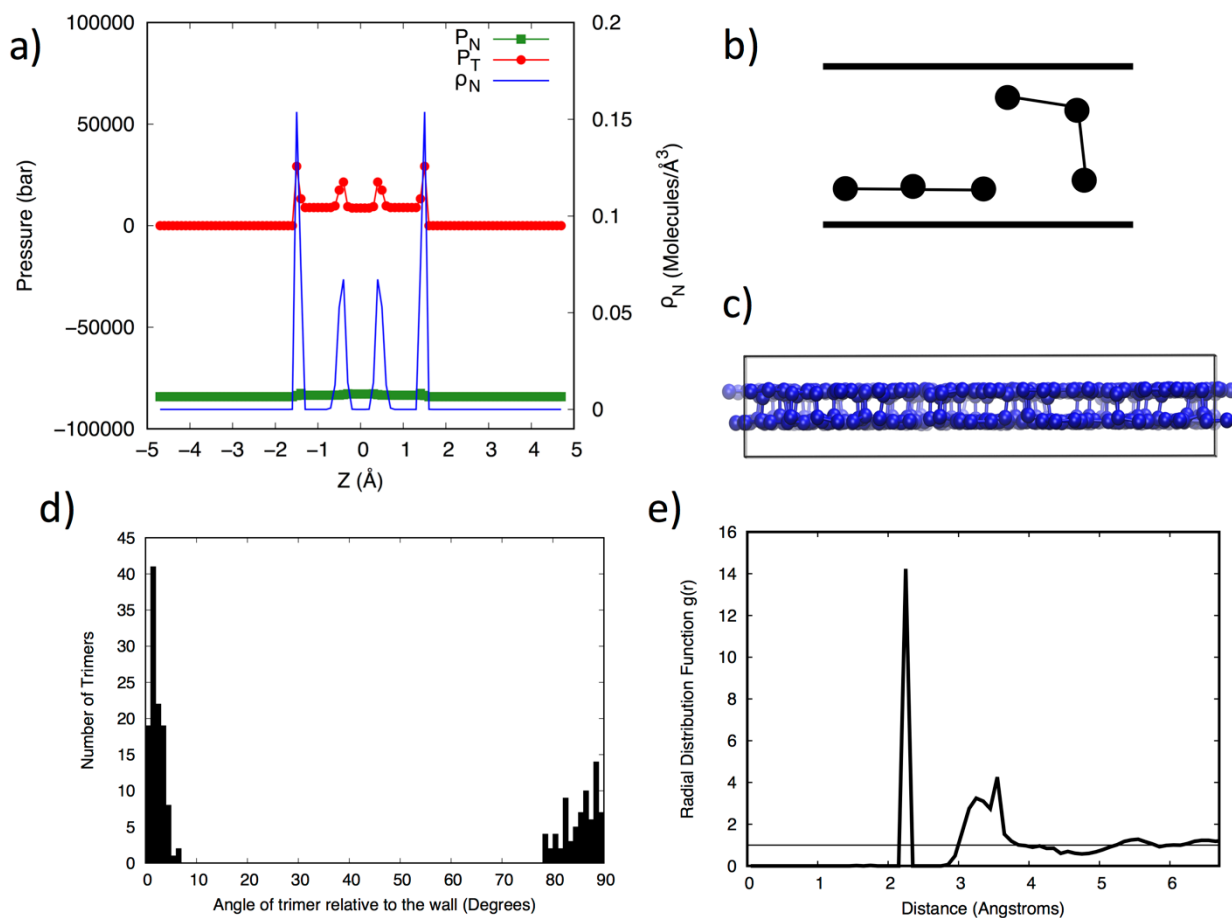


**Figure 2.14:** (a) Pressure and density profiles for the trimers in the  $3\sigma$  pore, at  $\alpha = 39$ ; (b) Two main orientations of the trimer in the  $3\sigma$  pore (c) Snapshot of the equilibrium configuration of the trimers in the  $3\sigma$  pore,  $\alpha = 39$ ; (d) Histogram of the angles of the trimers relative to the pore wall; (e) In-plane radial distribution function for the trimer sites in the  $3\sigma$  pore,  $\alpha = 39$ .

The pressure and density profiles for the trimers in the small  $3\sigma$  pore at  $\alpha = 39$  are shown in Figure 2.14(a). The normal pressure is, again, not constant in the small pore due to freezing. The tangential pressure peaks to about 29,000 bar while the molecular density peaks

to about  $0.15 \text{ trimers}/\text{\AA}^3$  in the contact layers. Due to the existence of a third site, the trimer molecule now has three rotational degrees of freedom which affects the shape of the tangential pressure profile. The trimers that have their center of mass in the contact layers are lying flat against the wall, with all three sites in contact with the pore wall. The plane of these trimers has an angle of 0 degrees relative to the pore wall (left trimer in Figure 2.14(b)). The density profile, which is based on the center-of mass, also shows two layers near the center of the pore. These layers represent trimers that have a relative angle closer to 90 degrees, indicating a more vertical alignment in the pore. In order to maximize the interaction of the three sites with the pore walls, the trimers generally align themselves in order to have 2 sites close to one of the contact layers and 1 site close to the other (right trimer in Figure 2.14b). Due to the center-of-mass layers being close together, the interactions between the two inner layers result in an additional plateau near the center of the pore. The histogram in Figure 2.14(d) shows the distribution of angles in the pore and confirms that the trimers in the pore are generally in one of these aforementioned two orientations. The radial distribution function for the trimers in the small pore is shown in Figure 2.14(e). The first sharp peak is the bond length between the bonded sites while the third sharp peak at around  $3.6 \text{ \AA}$  is the length between the two unbonded sites in the trimer. This indicates that the second peak prior to the third peak is the average separation distance, which is at  $3.25 \text{ \AA}$ .

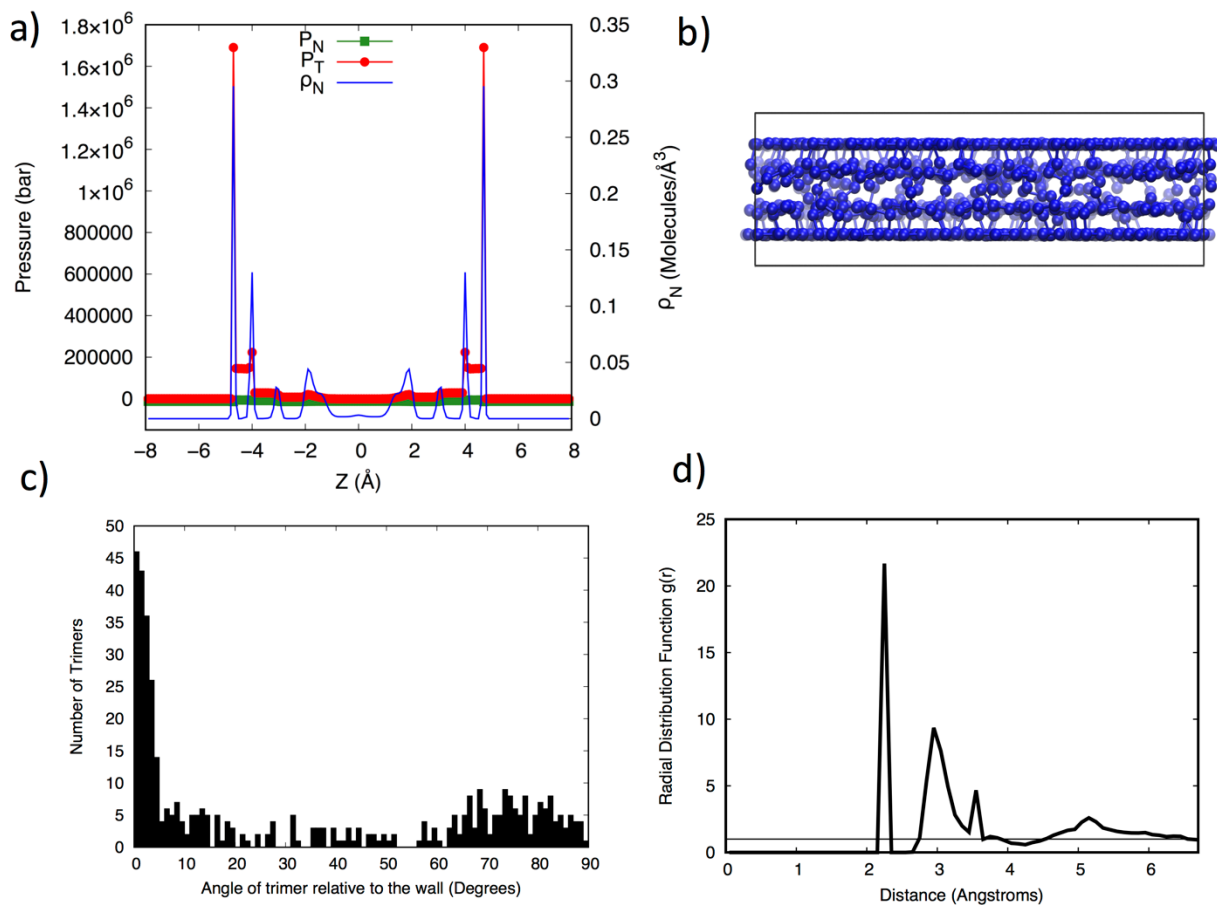


**Figure 2.15:** (a) Pressure and density profiles for the trimers in the  $5\sigma$  pore, at  $\alpha = 39$ ; (b) Snapshot of the equilibrium configuration of the trimers in the  $5\sigma$  pore,  $\alpha = 39$ ; (c) Histogram of the angles of the trimers relative to the pore wall; (d) In-plane radial distribution function for the trimer sites in the  $5\sigma$  pore,  $\alpha = 39$ .

Figure 2.15(a) shows the pressure and density profiles for the trimers in the large pore at  $\alpha = 39$ . The density profile clearly shows the presence of several layers in the pore and the visual snapshot in Figure 2.15(b) shows that while the contact layers are still strongly aligned, most of the inner layers are not. Due to the larger pore size, the trimers that are closer to the

center of the pore have a weaker interaction with the wall, allowing them to rotate in more orientations than the small pore. Due to the additional rotational degree of freedom that allows the trimers to rotate in three dimensions, broad shoulders are prominent in the tangential pressure profile, along with a second peak at the end of the shoulders at  $-4\text{\AA}$  and  $4\text{\AA}$ . From there, the tangential pressure tapers off as it extends towards the center of the pore. The wider distribution in trimer orientations is seen in the histogram in Figure 2.15(c) which now shows significantly more trimers rotated at angles between 10 and 80 degrees. The radial distribution function in Figure 2.15(d) shows the average separation distance in the contact layer to be around  $2.95\text{\AA}$ .

## 2.4 Summary and Discussion of Results

A summary of the main results is given in Table 2.1. In this table  $P_T$  and  $\rho_N$  are the peak values of the tangential pressure and the 3-D density of the contact layer next to the walls, while  $r_{xy}$  and  $F_{xy}$  are the mean separation distance and pair force between nearest neighbor molecules, respectively, in this contact layer. ‘Number of sites’ is the total number of molecular sites in the pore.

**Table 2.1:** Summary of the effect of molecular shape, fluid-wall interactions, and pore width on different parameters

	$P_T$ (bar)	$\rho_N = N/V$ (molecules / $\text{\AA}^3$ )	$r_{xy}$ ( $\text{\AA}$ )	Number of sites in pore	$F_{xy}$ ( $10^{-12}$ N)
<b>Monomers</b>					
<b>H=3<math>\sigma</math>, <math>\alpha = 10</math></b>	115,806	0.39	3.35	504	39
<b>H=3<math>\sigma</math>, <math>\alpha = 39</math></b>	484,662	0.63	3.15	576	$1.48 \times 10^2$
<b>H=5<math>\sigma</math>, <math>\alpha = 10</math></b>	161,244	0.43	3.25	904	80
<b>H=5<math>\sigma</math>, <math>\alpha = 39</math></b>	$2.25 \times 10^6$	0.94	2.95	1187	$4.53 \times 10^2$
<b>Dimers</b>					
<b>H=3<math>\sigma</math>, <math>\alpha = 10</math></b>	74,470	0.26	3.35	526	39
<b>H=3<math>\sigma</math>, <math>\alpha = 39</math></b>	95,483	0.27	3.25	556	80
<b>H=5<math>\sigma</math>, <math>\alpha = 10</math></b>	336,494	0.32	3.15	1118	$1.48 \times 10^2$
<b>H=5<math>\sigma</math>, <math>\alpha = 39</math></b>	$2.64 \times 10^6$	0.55	2.95	1266	$4.53 \times 10^2$
<b>Trimers</b>					
<b>H=3<math>\sigma</math>, <math>\alpha = 39</math></b>	29,211	0.15	3.25	561	39
<b>H=5<math>\sigma</math>, <math>\alpha = 39</math></b>	$1.69 \times 10^6$	0.30	2.95	1284	$4.53 \times 10^2$

The average separation distances between nearest neighbor monomer and dimer sites in the  $xy$  plane are shown in Figures 2.16(a) and 2.16(b) for all systems on the Lennard-Jones intermolecular force plot. By relating the average separation distance to the Lennard-Jones force, and comparing these values to those for a bulk Lennard-Jones fluid that undergoes no compression ( $F_{xy} = 0$ ), we can confirm the relationship between compression and high tangential pressures in the pores.

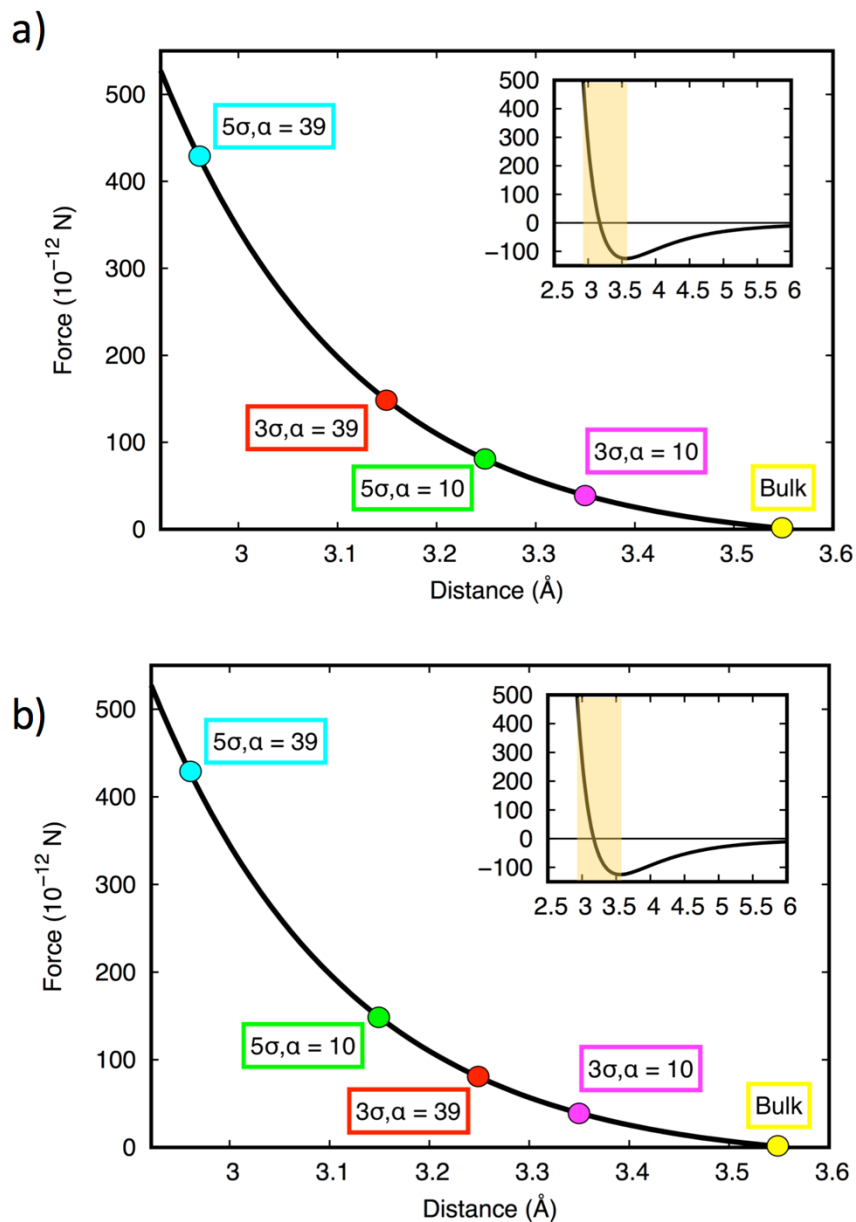


**Figure 2.16:** (a) The average separation distance between nearest neighbor monomer sites in the xy plane for all four monomer systems are shown on the Lennard-Jones intermolecular force plot as colored circles. Figure 2.5(d) is shown on the top right of each figure, with the shaded region identifying the area being plotted. (b) The average separation distance between nearest neighbor dimer sites in the xy plane for all four dimer systems are shown on the Lennard-Jones intermolecular force plot.

### 2.4.1 Effect of $\alpha$ parameter

An increase in the value of  $\alpha$  results from an increase in the attractive force exerted on the adsorbate molecules by the pore walls, and so leads to an increase in compression. For the contact layer next to the walls of the pore this is shown in Table 2.1 as an increase in the number density,  $\rho_N$ , the nearest neighbor pair force,  $F_{xy}$ , and the tangential pressure,  $P_T$ , and in a decrease in the nearest neighbor separation distance,  $r_{xy}$ .

For the monomers in the small pores, Figure 2.5(a) and Figure 2.6(a) show the tangential pressure for  $\alpha = 39$  to be almost 4 times larger than the tangential pressure for  $\alpha = 10$ , indicating an almost proportional relationship between  $\alpha$  and the tangential pressure. The radial distribution functions in Figure 2.5(c) and Figure 2.6(b) show the most probable distance between monomers at  $\alpha = 39$  to be about 0.2 Å shorter than at  $\alpha = 10$ . Since the monomers are in the steep repulsive region at these distances, a 0.2 Å difference has a significant impact on the repulsive forces (see Figure 2.5(d)), and consequentially on the tangential pressures.

For the monomers in the larger  $H = 5\sigma$  pores,  $\alpha$  has an even more significant effect on the magnitude of the tangential pressures. The larger pores allow the accommodation of a greater number of monomers stacked into 4 layers. The mean separation distance between nearest neighbors,  $r_{xy}$ , is now smaller than for the smaller pores, so that the repulsive force is increasing more steeply as the molecules become closer; also the decrease in  $r_{xy}$  on increasing  $\alpha$  is greater in this case. These two factors lead to a much larger effect of  $\alpha$  on the tangential pressure, as seen in Table 3.1. Increasing  $\alpha$  from 10 to 39 leads to an increase in  $P_T$  of more

than a factor of 13, with a peak tangential pressure of more than 2 million bar for the higher  $\alpha$  value.

The number density of monomers in the contact layers for the large pores at  $\alpha = 39$  are shown in Figure 2.8(a), and are almost double that shown in Figure 2.7(a) for  $\alpha = 10$ . The radial distribution functions in Figure 2.7(c) and Figure 2.8(b) show that the most probable distance between monomers in the contact layer is 0.25 Å shorter for the higher  $\alpha$  value. In the steep region of the intermolecular force plot, this difference would result in markedly stronger repulsive forces, and therefore notably larger tangential pressures. Figure 2.7(a) and Figure 2.8(a) show that the magnitude of the tangential pressure peaks is about 12 times larger for the higher  $\alpha$  value.

For the dimers, the effect of the  $\alpha$  parameter becomes more complex, as molecular orientation introduces another degree of freedom to the system. Since the small pores can only accommodate two molecular layers, Figures 2.10(a) and 2.11(a) show a visible difference in the shape of the tangential pressure with the modification of  $\alpha$ . At  $\alpha = 10$ , the dimers in the small pore are lying flat against the wall, verified by the configuration and histogram of the angles in Figure 2.10(b) and 2.10(c) respectively. At  $\alpha = 39$ , the stronger fluid-wall interactions force more dimers into the pore than at  $\alpha = 10$  for the same pore width. To pack more efficiently into the small space in the pore, the dimers at the higher  $\alpha$  now tend to also align themselves vertically, rather than just horizontally, allowing each dimer site to interact with the two pore walls. The dimers having a near vertical orientation allows them to be closer to each other, in spite of the great repulsion between the dimer sites, leading to larger repulsive forces. This histogram in Figure 2.11(c) shows that a number of dimers have an angle close to 90 degrees,

confirming the vertical orientation in the pore. It also leads to the small peak in the tangential pressure in the center of the pore, since the center of mass for these dimers is located near the center of the pore.

Because of the increased number of dimers in the smaller pore at  $\alpha = 39$ , the peaks in the tangential pressure are slightly higher than the peaks at  $\alpha = 10$ . Since the magnitude of the tangential pressure is largely dependent on how closely packed the dimers are to each other, it is also useful to compare the site-site radial distribution functions for the two cases. Figures 2.10(d) and 2.11(d) show the shortest distance between nearest neighbor dimer sites is around 0.1 Å shorter for the higher  $\alpha$  value, verifying that larger  $\alpha$  values consistently lead to closer proximity between molecules.

The  $\alpha$  parameter continues to have a significant effect for the dimers in the larger pores, with the tangential pressure being about 8 times larger at  $\alpha = 39$ , as demonstrated in Figures 2.12(a) and 2.13(a). The molecular density in the contact layers increases by a factor of 1.75 at the larger  $\alpha$  and more dimers are forced to rotate in different directions to better fit in the pore, as seen in Figures 2.13(b) and 2.13(c). The radial distribution functions in Figures 2.12(d) and 2.13(c) show that the most probable distance between dimers decreases from 3.15 Å (smaller  $\alpha$ ) to 2.95 Å (larger  $\alpha$ ). This results in a significant increase in the tangential pressure due to its position in the deeply repulsive region of the intermolecular force plot.

#### *2.4.2 Effect of molecular geometry*

Molecular geometry has a tangible impact on the shape and magnitude of the tangential pressure tensor profile. It is difficult to establish a direct relationship between the molecular

geometry and the magnitude of the pressure tensor because the geometry affects the crystallinity and ordering of the fluid systems in the pores. While pores with monomers can form ordered hexagonal crystalline phases, pores with multi-site molecules often consist of less-ordered or deformed glassy phases. In larger pores, if all other variables are kept constant, systems with dimers consistently show higher tangential pressures than systems with monomers. This could be due to a combination of multiple factors, such as closer or equivalent packing for the dimers in larger pores, and a significantly higher density of dimer molecular sites, leading to an overall higher contribution to the pressure tensor. The trimers, on the other hand, consistently show lower tangential pressures than the monomers and dimers. This could perhaps be attributed to the bulkiness of the trimers, which results in a less ordered phase and fewer site-site interactions.

Figures 2.8(a) and 2.13(a) compare the pressures for monomers and dimers in the large pore at  $\alpha = 39$ . In addition to the higher tangential pressure peaks for the dimers, there is now also a difference in the shape of the tangential pressure profile between the two systems. The tangential pressure profile for dimers in the contact layers still exhibits strong peaks, but small broad shoulders can be seen arising from those peaks and extending towards the center of the pore, as can be seen more clearly in Figure 2.17).

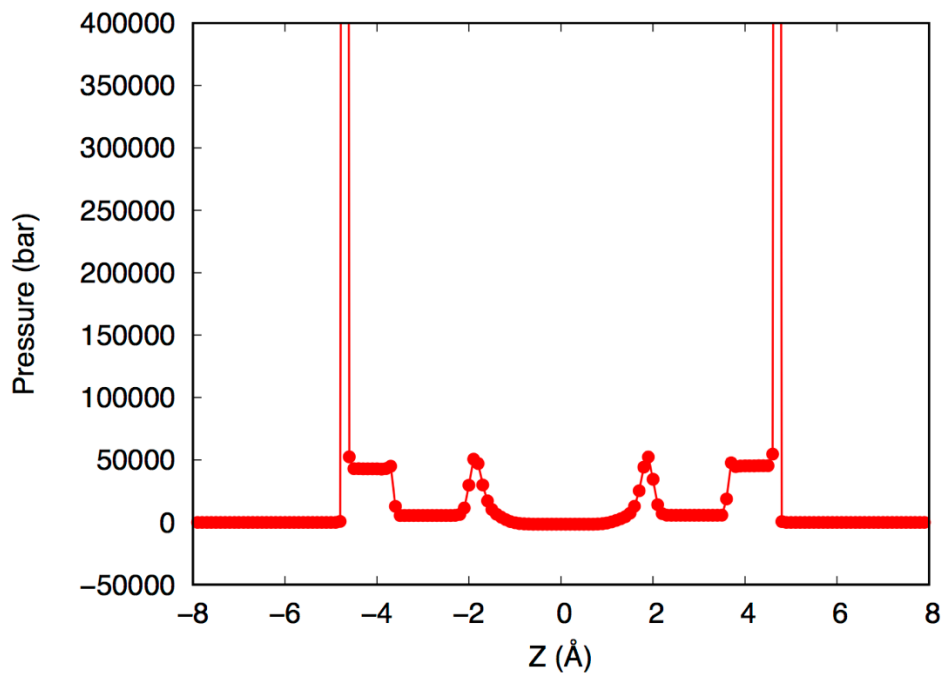


**Figure 2.17:** An enlarged view of the tangential pressure tensor profile for the dimers in a  $5\sigma$  pore at  $\alpha = 39$ , showing the broad shoulder effect.

This phenomenon, to our knowledge, has not been documented in the literature. The sharp peaks correlate to a high density of dimer molecules near the wall that are lying flat in order to maximize their interaction with the wall. The broad shoulders are likely an effect of a weaker interaction between the molecules closer to the center of the pore and the wall, which allows the dimers to rotate in different orientations. This results in a non-integer number of molecule site layers contributing to the broad shoulder effect, since the interaction energy is being distributed between the regions of molecular site interactions. This can be confirmed by visualizing the configuration inside the pore in Figure 2.13(b). While the top and bottom layers closer to the wall are extremely closely packed and linear, the center layers exhibit a less

structured configuration. Because monomers have zero rotational degrees of freedom, they result in an integer number of layers spaced apart from each other, which results in the sharp peaks that have been observed in literature.

The effect of molecular geometry in large pores is even more prominent when looking at trimers, as seen in Figure 2.14(a). The broad shoulders in the tangential pressure profile for trimers can again be observed and is now more pronounced. The pressure profile for the trimers shows a peak at the end of the shoulder, followed by a small shoulder that tapers off as it nears the center of the pore. This is due to the additional rotational degree of freedom resulting from the third site. Larger pores allow a higher number of trimers in the pore, leading to many more orientations that contribute to the more obvious appearance of the broad shoulders. The monomers under the same conditions in Figure 2.8(a) only see sharp peaks, due to their inability to have rotations.

In the smaller pores, the effect of molecular geometry on the shape of the tangential pressure is only apparent at  $\alpha = 39$ . The trimers were only studied at  $\alpha = 39$  due to sampling issues at lower  $\alpha$  values, a result of the bulky structure of the trimers. Figures 2.5(a) and 2.10(a) show similar shaped profiles for the tangential pressure at  $\alpha = 10$ ; *i.e.* both have sharp peaks with no broad shoulders even though they are systems with different molecular geometries. This is because, as mentioned earlier, the configuration of the dimers at  $\alpha = 10$  resembles the configuration for the monomers. The dimers are lying flat against the wall, resulting in an integer number of molecular layers. It's only at the higher  $\alpha$  value that more dimers pack into the small pore, forcing them to re-orient themselves in a vertical direction. This leads to the small shoulder effect that extends to the center of the pore (see Figure 2.11(a)).

### 2.4.3 Effect of pore size

Pore size is found to have a significant impact on the number of layers in the pore as well as on the shape and magnitude of the tangential pressure. For monomers, larger pores are able to accommodate 4 integer adsorbate layers, compared to the 2 layers in smaller pores (see Figures 2.5(a) and 2.7(a)). This increase in the number of layers correlates to a larger number of molecules in the pore and, therefore, higher in-pore tangential pressures. In the larger pore, the tangential pressure also exhibits 4 peaks, at the same locations as the peaks in molecular density. The effect is the same at both values of  $\alpha$ , although the increase in tangential pressure is much more substantial at  $\alpha = 39$  (see Figures 2.6(a) and 2.8(a)). The increase in tangential pressure with increasing pore size is different from the phenomenon observed by Long et al.<sup>5</sup> who studied the effect of pore size on argon in slit-shaped pores. Long et al. used Lorentz-Berthelot mixing rules to describe the fluid-wall interactions and studied a variety of pore widths, including  $H = 3\sigma$  and  $H = 4.5\sigma$ . They found the tangential pressure to be 10,000 bar lower in the larger pore when compared to the smaller pore. This is due to a weaker interaction of the argon molecules in the center layer of the larger pore with the wall, leading to a lower molecular density in the pore. We show here that when the fluid-wall interactions are stronger, it results in more molecules entering the larger pore. This increase in the number of molecules leads to higher tangential pressures.

The effect of pore width on the dimers at  $\alpha = 10$  can be seen by comparing Figures 2.10(a) and 2.12(a), which show results for the smaller and larger pore, respectively. Due to the larger size of the pore in Figure 2.12(a), it is able to accommodate a greater number of

dimer layers than the small pore in Figure 2.10(a). In addition, the dimers are also able to rotate more freely because of the weaker interaction of the center layers with the walls. The smaller pore is only able to accommodate two layers and because of the closer proximity of the dimers with the wall, they show little to no rotation. The higher number of dimers in the larger pore leads to higher tangential pressures, and the ability of more dimers to rotate results in the very slight broad shoulder effect in the tangential pressure profile, as seen in the enlarged view in Figure 2.18. At  $\alpha = 39$ , the effect of varying the pore size is even more substantial due to a larger number of dimers that are more closely packed. In Figure 2.13(a) it is seen that dimers in the larger pore experience very high tangential pressures, with the magnitude of the peak being about 25 times higher than for the small pore (see Figure 2.11(a)). As a result of more dimer rotations, the broad shoulder effect is also more prominent in the large pore at  $\alpha = 39$ .

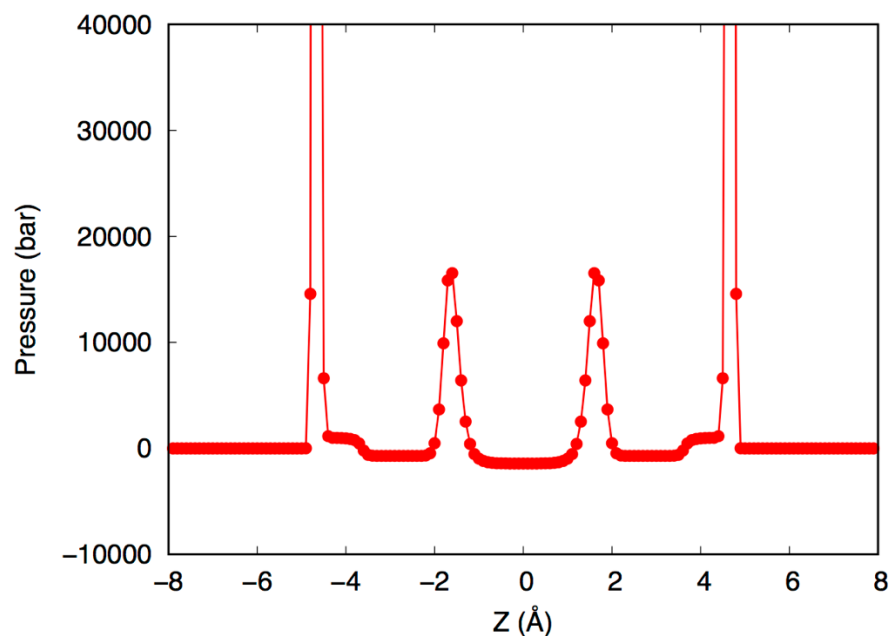


**Figure 2.18:** An enlarged of the tangential pressure for dimers in the  $5\sigma$  pore at  $\alpha = 10$ , showing the slight broad shoulder effect.

A similar effect is observed with the trimers in Figures 2.14(a) and 2.15(a). The trimers in the small pore are forced to either lie almost completely horizontally or completely vertically in the plane to maximize their interactions with the wall. In the larger pores, however, weaker interaction in the inner layers allow the trimers to rotate in all three dimensions, leading to multiple non-integer layers that are less structured. This results in broad shoulders due to the fluid-fluid interactions between the sites, as well as higher tangential pressures in the larger pore due to a greater number of molecules.

## 2.5 Conclusion

Through Monte Carlo simulations, we found that all three variables, a) wetting parameter,  $\alpha$ , b) the molecular geometry of the adsorbate molecules, and c) the width of the slit pore, had a large impact on the tangential pressure tensor in the pore, often changing the qualitative behavior of the pressure profiles. The monomer consistently showed sharp peaks in the tangential pressure but the magnitude of these peaks increased significantly with  $\alpha$  and with pore width, due to an increased number density of monomers in the pore. The multi-site molecules also experienced an increase in tangential pressure with  $\alpha$  and pore width, but due to additional rotational degrees of freedom, they often exhibited a non-integer number of molecular layers in the larger pores. This resulted in broad shoulders attached to the sharp peaks in the tangential profile, a unique phenomenon that is not observed with single-site Lennard Jones molecules.

## 2.6 Acknowledgement

We thank the National Science Foundation for their continued support and funding of this work through grant CBET-1603851. We would also like to acknowledge Dr. Yun Long from the National University of Singapore for helpful discussions, and for assisting us through his previous work on pressure tensors for argon.

## 2.6 References

- (1) Gregg, S. J.; Sing, K. S. W.; Salzberg, H. W. Adsorption Surface Area and Porosity. *J. Electrochem. Soc.* **1967**, *114*, 279C.
- (2) Huse, D. A. Incomplete Wetting by Adsorbed Solid Films. *Phys. Rev. B* **1984**, *29*, 6985–6987.
- (3) van Bavel, A. P.; Hopstaken, M. J. P.; Curulla, D.; Niemantsverdriet, J. W.; Lukkien, J. J.; Hilbers, P. A. J. Quantification of Lateral Repulsion between Coadsorbed CO and N on Rh(100) Using Temperature-Programmed Desorption, Low-Energy Electron Diffraction, and Monte Carlo Simulations. *J. Chem. Phys.* **2003**, *119*, 524–532.
- (4) Al-Sarraf, N.; King, D. A. Calorimetric Adsorption Heats on Low-Index Nickel Surfaces. *Surf. Sci.* **1994**, *307–309*, 1–7.
- (5) Long, Y.; Palmer, J. C.; Coasne, B.; Śliwinska-Bartkowiak, M.; Gubbins, K. E. Pressure Enhancement in Carbon Nanopores: A Major Confinement Effect. *Phys. Chem. Chem. Phys.* **2011**, *13*, 17163.
- (6) Long, Y.; Palmer, J. C.; Coasne, B.; Śliwinska-Bartkowiak, M.; Jackson, G.; Müller, E. A.; Gubbins, K. E. On the Molecular Origin of High-Pressure Effects in Nanoconfinement: The Role of Surface Chemistry and Roughness. *J. Chem. Phys.* **2013**, *139*, 144701.
- (7) Abaza, S.; Aranovich, G. L.; Donohue, M. D. Adsorption Compression in Surface Layers. *Mol. Phys.* **2012**, *110*, 1289–1298.
- (8) Schofield, P.; Henderson, J. R. Statistical Mechanics of Inhomogeneous Fluids. *Proc. R. Soc. Lond. A. Math. Phys. Sci.* **1982**, *379*, 231–246.

- (9) Gray, C.; Gubbins, K.; Joslin, C. Theory of Molecular Fluids 2. Applications. In *Oxford Science Publications*; Oxford University Press, 2011; Sec. 83.
- (10) Sliwińska-Bartkowiak, M.; Drozdowski, H.; Kempański, M.; Jażdżewska, M.; Long, Y.; Palmer, J. C.; Gubbins, K. E. Structural Analysis of Water and Carbon Tetrachloride Adsorbed in Activated Carbon Fibres. *Phys. Chem. Chem. Phys.* **2012**, *14*, 7145–7153.
- (11) Rowlinson, J. S.; Widom, B. *Molecular Theory of Capillarity*; Clarendon Press: Oxford, 1982; Vol. 167.
- (12) Irving, J. H.; Kirkwood, J. G. The Statistical Mechanical Theory of Transport Processes. IV. The Equations of Hydrodynamics. *J. Chem. Phys.* **1950**, *18*, 817–829.
- (13) Harasima, A. Molecular Theory of Surface Tension. In; John Wiley & Sons, Inc.; pp. 203–237.
- (14) Walton, J. P. R. B.; Tildesley, D. J.; Rowlinson, J. S.; Henderson, J. R. The Pressure Tensor at the Planar Surface of a Liquid. *Mol. Phys.* **1983**, *48*, 1357–1368.
- (15) Heinz, H. Calculation of Local and Average Pressure Tensors in Molecular Simulations. *Mol. Simul.* **2007**, *33*, 747–758.
- (16) Coasne, B.; Long, Y.; Gubbins, K. E. Pressure Effects in Confined Nanophases. *Mol. Simul.* **2014**, *40*, 721–730.
- (17) Fujimori, T.; Morelos-Gómez, A.; Zhu, Z.; Muramatsu, H.; Futamura, R.; Urita, K.; Terrones, M.; Hayashi, T.; Endo, M.; Hong, S. Y.; *et al.* Conducting Linear Chains of Sulphur inside Carbon Nanotubes. *Nat. Commun.* **2013**, *4*.
- (18) Luo, H.; Desgreniers, S.; Vohra, Y. K.; Ruoff, A. L. High-Pressure Optical Studies on Sulfur to 121 GPa: Optical Evidence for Metallization. *Phys. Rev. Lett.* **1991**, *67*, 2998–3001.

- (19) Steudel, R.; Eckert, B. Solid Sulfur Allotropes. In *Elemental Sulfur and Sulfur-Rich Compounds I*; 2003; pp. 1–79.
- (20) Addington, C. K.; Mansell, J. M.; Gubbins, K. E. Computer Simulation of Conductive Linear Sulfur Chains Confined in Carbon Nanotubes. *Mol. Simul.* **2017**, *43*, 519–525.
- (21) Kaneko, K.; Fukuzaki, N.; Kakei, K.; Suzuki, T.; Ozeki, S. Enhancement of Nitric Oxide Dimerization by Micropore Fields of Activated Carbon Fibers. *Langmuir* **1989**, *5*, 960–965.
- (22) Byl, O.; Kondratyuk, P.; Yates, J. T. Adsorption and Dimerization of NO Inside Single-Walled Carbon Nanotubes - An Infrared Spectroscopic Study. *J. Phys. Chem. B* **2003**, *107*, 4277–4279.
- (23) Panagiotopoulos, A. Z. Adsorption and Capillary Condensation of Fluids in Cylindrical Pores by Monte Carlo Simulation in the Gibbs Ensemble. *Mol. Phys.* **1987**, *62*, 701–719.
- (24) Panagiotopoulos, A. Z. Direct Determination of Phase Coexistence Properties of Fluids by Monte Carlo Simulation in a New Ensemble. *Mol. Phys.* **1987**, *61*, 813–826.
- (25) Frenkel, D.; Smit, B. *Understanding Molecular Simulation*; 2nd ed.; Academic Press: San Diego, 2002.
- (26) Steele, W. A. The Physical Interaction of Gases with Crystalline Solids. *Surf. Sci.* **1973**, *36*, 317–352.
- (27) Steele, W. A. *The Interaction of Gases with Solid Surfaces*; Pergamon Press: Oxford, 1974.

- (28) Jiang, S.; Rhykerd, C. L.; Gubbins, K. E. Layering, Freezing Transitions, Capillary Condensation and Diffusion of Methane in Slit Carbon Pores. *Mol. Phys.* **1993**, *79*, 373–391.
- (29) Lorentz, H. A. Ueber Die Anwendung Des Satzes Vom Virial in Der Kinetischen Theorie Der Gase. *Ann. Phys.* **1881**, *248*, 127–136.
- (30) Berthelot, D. Sur Le Mélange Des Gaz. *Comptes rendus Hebd. des séances l'Académie des Sci.* **1898**, *126*, 1703–1855.
- (31) Henderson, J. R. Potential-Distribution Theorem. *Mol. Phys.* **1983**, *48*, 715–717.
- (32) Long, Y.; Palmer, J. C.; Coasne, B.; Śliwinska-Bartkowiak, M.; Gubbins, K. E. Under Pressure: Quasi-High Pressure Effects in Nanopores. *Microporous Mesoporous Mater.* **2012**, *154*, 19–23.

## Chapter 3 : The Nitric Oxide Dimer Reaction in Slit-Shaped Pores and Carbon Nanotubes

### 3.1 Introduction

When carried out in a nano-porous catalyst or catalyst support, heterogeneous reactions are often strongly affected by the pore shape and width, surface heterogeneity, and by the interactions of the various reactant, product and activated species with the pore walls. These factors can have a large influence on the reaction yield<sup>1-4</sup>, the rate<sup>5</sup>, the activation barriers<sup>6-8</sup>, and in some cases can alter the reaction mechanism<sup>6,8,9</sup> or produce new product phases<sup>9-11</sup>. Other considerations in such heterogeneous reactions include surface defects in the solid substrate, which can form highly reactive sites<sup>6,12</sup>, high tangential pressures due to the strong force field from the solid substrate, thus promoting high pressure reactions<sup>9,13</sup> and shape-catalytic effects<sup>8</sup>. The latter effect occurs when the pore size and shape becomes similar to that of the molecules. For such reactions, when the transition state theory is appropriate, the pore size can enhance or hinder the reaction if the shape of the transition state is similar to that of the pore, leading to dramatic effects of pore size. Small changes in the pore width then have a large effect on the potential energy surface of the reaction and on the reaction rate, as shown by a study of the rotational isomerism of C<sub>4</sub> hydrocarbons in carbon pores<sup>8</sup>.

In this chapter, we report a study of the nitric oxide dimerization reaction,  $2\text{NO} \leftrightarrow (\text{NO})_2$ , in carbon nanopores. This reaction is of interest for several reasons: (a) reliable experimental data are available for this reaction in well-defined nanoporous carbons; (b) the results of these experimental studies are surprising, showing complete conversion to the dimer

in the nanopores, although there are almost no dimers in the bulk gas phase that is in equilibrium with the porous material; and (c) the failure of theoretical studies so far to provide a satisfactory explanation of these results.

In 1989, Kaneko et al.<sup>1</sup> reported a study of the nitric oxide dimer reaction in NO-adsorbed activated carbon fibers, for the temperature range 273-423 K under a nitric oxide gas pressure of 80 kPa. The carbon fibers, which have slit-shaped pores, had a relatively uniform pore width of 0.8-0.9 nm. The composition of the confined nano-phase was determined using magnetic susceptibility measurements (while the monomer is paramagnetic, the dimer is diamagnetic), and it was found that more than 98 mole % of the molecules consisted of (NO)<sub>2</sub> dimers, even though the fraction of dimers in the bulk phase in equilibrium with the pore was of the order a few mole % or less. This surprising result was confirmed in later experiments carried out by Byl et al.<sup>2</sup>, who studied the reaction in (10,10) single-walled carbon nanotubes having a diameter of 1.36 nm over the temperature range 103-136 K, under nitric oxide gas pressures up to a few torr. Equilibrium compositions within the SWNTs were determined using Fourier Transform Infrared Spectroscopy, and the mole fraction of dimers was shown to be 100%, within the experimental error, which was estimated to be 5%. The FTIR results suggested a strong interaction between the dimers and the walls of the SWNTs.

Theoretical calculations for the nitric oxide dimer reaction in the bulk phase were made by Johnson et al.<sup>14</sup>, using the reactive canonical Monte Carlo (MC) method, and found very good agreement with experimental results<sup>15,16</sup> for the saturated liquid NO temperature range from 110 to 140 K. For the NO monomer, they used a single-site LJ sphere model with potential parameters proposed by Kohler et al.<sup>17</sup>; they noted that although the NO molecule is

not spherical, its dipole moment ( $\sim 0.16 \times 10^{-18}$  esu) is negligibly small, its quadrupole moment ( $\sim 1.0 \times 10^{-26}$  esu) is also quite small and its overlap interactions depart only slightly from spherical, making a spherical LJ model reasonable. For the nitric oxide dimer they used a two-center LJ model, the LJ sites having the same potential parameters as for the NO monomer. Turner et al.<sup>3</sup> used the reactive canonical MC method in conjunction with the constant pressure Gibbs ensemble MC algorithm<sup>18,19</sup> to carry out two-phase reaction simulations that included a bulk gas phase in equilibrium with a pore phase. They studied the reaction in slit-shaped carbon pores for the temperature range 119 to 163 K under a constant bulk pressure of 0.16 bar, for a range of pore widths from  $2.5\sigma_{\text{NO}}$  to  $5.5\sigma_{\text{NO}}$  (0.79 to 1.74 nm). The carbon walls were modeled using the (10,4,3) potential of Steele<sup>20</sup>, obtained by integrating the adsorbate-wall interactions over the positions of the carbon atoms, and using the usual LJ interaction parameters for carbon<sup>20</sup>. The cross-term LJ interactions for both adsorbate-adsorbate and adsorbate-wall potentials were calculated using the Lorentz-Berthelot combining rules. The yield of the nitric oxide dimer in the carbon pores was found to be greatly enhanced over that in the bulk gas phase in equilibrium with the pore phase, by a factor of 40 or more at the lowest temperatures studied, with a yield of about 95 mole % in the smaller pores at 119 K. However, the predicted yields were significantly lower than those observed in the experiments and decreased rapidly as the temperature was increased, in contrast to the experimental results, which showed yields close to 100% for all of the temperature range studied. Lisal et al.<sup>21</sup> carried out more extensive reactive MC calculations for the reaction in slit pores of width 1.7 nm using the same models, and the reaction in carbon pores was also studied by Tripathi and Chapman<sup>4</sup> using classical density functional theory with slightly different models. The results of these studies agreed

with those of Turner et al<sup>3</sup>. However, in all cases the yield of dimer was lower, and the temperature dependence of the yield was quite different, from those found in the experiments. Similar reactive MC simulations of the NO dimer reaction were performed by Turner<sup>22</sup> for a (10,10) SWNT bundle at 130 K, using very similar models to those used for the slit-pore studies, for the same conditions as studied experimentally by Byl et al<sup>2</sup>. The predicted conversion was found to be about 60 mole % dimer, again considerably lower than the 100 mole % observed in the experiments. In all of these theoretical studies the increase in yield relative to that in the bulk phase at the same conditions was attributed to the increased density in the confined nano-phase.

Chapter 3 is arranged as follows. In Section 3.2 we describe the models used and the molecular simulation methods. Included in this section is a description of *ab initio* calculations for the intermolecular interactions between the NO monomer molecules and the carbon walls, and for the (NO)<sub>2</sub> dimers and the walls. In Section 3.3 we present the results for the *ab initio* calculations and for the reaction yield in pores of both slit and cylindrical geometry, and make comparison with the experimental results for activated carbon fibers and SWCNTs. We also present simulation results for the fluid structure and for the pressure tensor components in the confined nano-phase. Our conclusions are summarized in Section 3.4.

## 3.2 Simulation Methods

### 3.2.1 Monte Carlo Simulations

We used the Reactive Monte Carlo ensemble (RxMC) along with the Constant Pressure Gibbs Ensemble (CP-GEMC) mentioned in Sections 1.3 and 2.2 to study the nitric oxide dimerization reaction in a two-phase system. The CP-GEMC ensemble allows us to measure the equilibrium conversion without needing to define quantities such as chemical potentials or fugacities.

In the RxMC ensemble, moves are conducted to simulate the reaction by inserting and deleting molecules based on stoichiometry. These reactive moves are carried out in both the bulk and pore phases and ensure the reaction equilibrium criterion for the reaction is satisfied. Since the RxMC method minimizes the Gibbs energy at constant pressure, it allows us to determine the true equilibrium state. The general acceptance criteria for the forward and reverse reaction steps is shown in Equation 3.1.

$$P_{acc} = \min \left[ 1, \exp(-\beta\delta U) \prod_{i=1}^c q_i^{v_i} \prod_{i=1}^c \frac{N_i!}{(N_i + v_i)!} \right] \quad (3.1)$$

The RxMC method used with the CP-GEMC method consists of a combination of the following MC moves:

- i. random change in the position or orientation of a molecule,
- ii. forward reaction step, where one random NO monomer is deleted and another random NO monomer is changed to (NO)<sub>2</sub> dimer,

- iii. reverse reaction step, where one random (NO)<sub>2</sub> dimer is changed to an NO monomer and another NO monomer is randomly added to the system,
- iv. random change of volume in the bulk phase to keep the bulk pressure constant,
- v. transfer of NO monomers between the bulk phase and the pore phase.

By allowing the transfer of NO monomers between the two simulation boxes, chemical equilibrium is maintained within each phase and phase equilibrium is maintained between the two phase. Since the NO monomers are smaller and easier to transfer than the NO dimers and reaction moves are carried out in both phases, this method allows for enhanced sampling efficiency. Simulations were conducted at temperatures ranging from 120 K to 160 K and at a bulk pressure of 0.16 bar, which corresponds to a gas phase.

### 3.2.2 Pore Models

Carbon pores are modeled as slit-shaped pores and as carbon nanotubes. Slit-shaped pores are modeled with a variety of pore widths, ranging from  $3\sigma$  to  $5.5\sigma$ . The simulation box lengths in the x and y directions are  $L_x = 50 \text{ \AA}$  and  $L_y = 50 \text{ \AA}$ , each more than twice the cutoff length of  $5\sigma$  (i.e.  $15.8575 \text{ \AA}$ ). The carbon walls in the slit pore are simulated using the same 10-4-3 Steele potential<sup>23</sup> described in Section 2.2 for the fluid-wall (*fw*) interactions. The effective Lennard-Jones parameters used for carbon are:  $\sigma_w = 0.34 \text{ nm}$  and  $\epsilon_w/k_B = 28.0 \text{ K}$ . Standard Lorentz-Berthelot mixing rules<sup>24,25</sup> are then used to calculate the  $\sigma_{fw}$  parameter ( $\sigma_{fw} = \frac{\sigma_{ff} + \sigma_w}{2}$ ) which is calculated to be  $0.329 \text{ nm}$ . The  $\epsilon_{fw}$  parameter is calculated using the *ab initio* techniques outlined in the next section. The other parameters in the 10-4-3 Steele potential are  $\rho_w = 114 \text{ nm}^{-3}$  and  $\Delta = 0.335 \text{ nm}$ .

The carbon nanotubes are modeled as single-walled rigid carbon nanotube bundles arranged in a hexagonal array (Figure 3.1). The nanotube walls are simulated using explicit carbon atoms and the interactions between the adsorbate molecules and carbon atoms are calculated using the Lennard-Jones potential. Electrostatic interactions are ignored. Figure 3.1 shows the carbon nanotubes are simulated as bundles with two different helicities: (a) (8,8) and (b) (10,10). Their respective diameters are 1.09 nm and 1.36 nm, as measured between the center of the nanotube and the center of a carbon atom. The simulation box lengths are  $L_x = 42.7$ ,  $L_y = 49.3$  Å, and  $L_z = 32$  Å for the (8,8) bundle and  $L_x = 50.8$  Å,  $L_y = 57.2$  Å, and  $L_z = 32$  Å for the (10,10) bundle. Periodic boundary conditions are applied in all three directions and the intertubular distance for both nanotube bundles is 0.335 nm. Adsorption and reaction are allowed to occur in the interstitial spacing between the individual nanotubes.

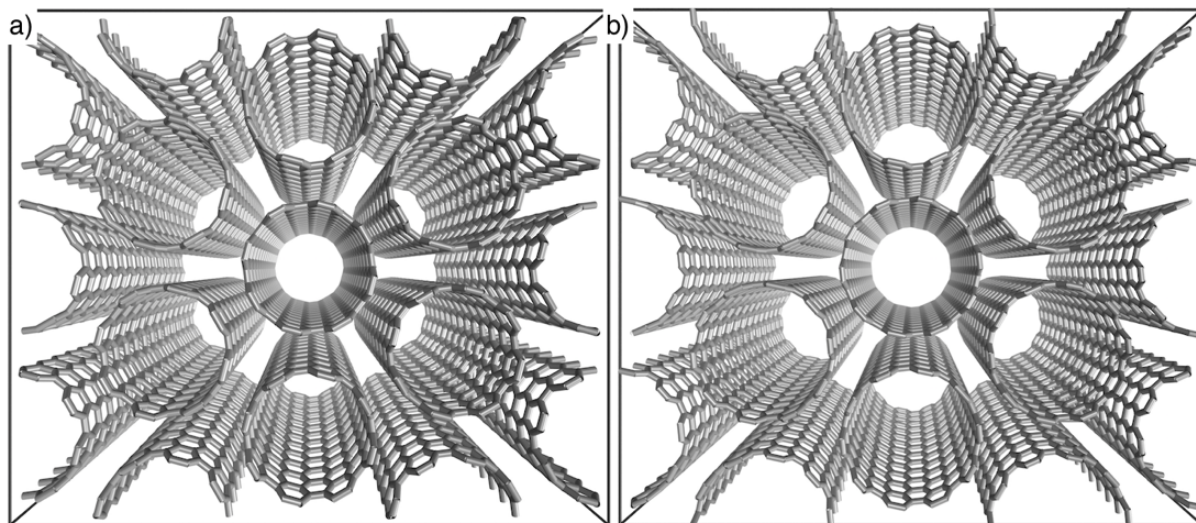


**Figure 3.1:** Simulation snapshots of the (a) (8,8) and (b) (10,10) nanotube bundles. The nanotube diameters are (a) 10.9 Å and (b) 13.6 Å and the intertubular distance is 3.35 Å for both bundles.

The NO monomer is modeled as a one-site Lennard-Jones molecule with the following parameters:  $\sigma_{\text{ff}} = 0.31715$  nm and  $\epsilon_{\text{ff}}/k_{\text{B}} = 125.0$  K. The NO dimer is modeled as a 2-site Lennard-Jones model with each site having the same parameters as the NO monomer, and a fixed bond length of  $2.237\text{\AA}^{26}$ . Since the monomer has a very small dipole and quadrupole moment<sup>27</sup>, electrostatic forces are neglected. In order to calculate the acceptance criteria for the reactive moves, translational, vibrational, rotational, and electronic partition functions for the monomer and dimer are obtained using the equations in Table 3.1.

**Table 3.1:** Partition functions for the NO monomer and (NO)<sub>2</sub> dimer

Partition Function	NO	(NO) <sub>2</sub>
Translational	$\left(\frac{2\pi mkT}{h^2}\right)^{1.5} V$	$\left(\frac{2\pi mkT}{h^2}\right)^{1.5} V$
Rotational	$\frac{8h^2IkT}{\sigma h^2}$	$\frac{\sqrt{\pi}}{\sigma} \left(\frac{T^3}{\theta_A\theta_B\theta_C}\right)^{0.5}$
Vibrational	$\frac{1}{1 - e^{-\beta h\nu}}$	$\prod \frac{1}{1 - e^{-\beta h\nu}}$
Electronic	$g_0 e^{-E_0/kT} + g_1 e^{-E_1/kT}$	$e^{D_b/T}$

In the equations for the translational partition function,  $m$  is the mass of the molecule,  $k$  is the Boltzmann constant,  $T$  is the temperature,  $h$  is Planck's constant, and  $V$  is the volume of the system. For the rotational partition functions,  $I$  is the moment of inertia of the molecule,  $\sigma$  is the symmetry factor, and  $\Theta_A$ ,  $\Theta_B$ ,  $\Theta_C$  are the rotational temperatures, defined as  $\theta_i = \left(\frac{8\pi^2 I_i kT}{h^2}\right)^{0.5}$ . For the vibrational partition functions,  $\beta = 1/kT$ ,  $\nu$  represents the vibrational

frequencies obtained from Smith et al.<sup>28</sup>, and the product runs over all the normal modes. For the electronic partition functions,  $g_0 = 2$  and  $g_1 = 4$  are the degeneracies while  $E_0 = 0$  and  $E_1 = 121.1 \text{ cm}^{-1}$  are the electronic energies, referred to the zero-point vibrational energy. Since the NO monomer has a low-lying electronic state, the second term in the electronic partition function for the monomer, which is usually ignored, is also accounted for. We used a value of 10.9 kJ/mol for  $D_b$ , the binding energy of the dimer<sup>3</sup>. The interactions between fluid molecules are calculated using Lorentz-Berthelot mixing rules, which have been shown to be accurate for like-like molecules.

In order to determine more accurate interaction energies between the carbon pore wall and the NO molecules, we conducted *ab initio* calculations using Gaussian 09. We used a single benzene ring to determine the effect of an aromatic environment on the NO monomer and dimer<sup>29</sup>. We performed the calculations using Møller-Plesset perturbation theory at the MP2 level using the aug-cc-pVDZ basis set. The counterpoise correction was used to limit the effect of the basis set superposition error (BSSE). We conducted calculations for NO, (NO)<sub>2</sub>, C<sub>6</sub>H<sub>6</sub>, NO-C<sub>6</sub>H<sub>6</sub>, and (NO)<sub>2</sub>-C<sub>6</sub>H<sub>6</sub> and used the results to estimate the interaction energies for both the monomer and dimer interactions with the carbon walls.

The slit-pore pressure tensor was calculated using the same method outlined in Section 2.2. We used a bin width of 0.1 Å to determine accurate density and pressure profiles.

### **3.3 Results and Discussion**

#### *3.3.1 Sensitivity Analysis and Ab Initio Calculations*

In order to determine whether the solid-fluid interaction energies could be the reason for the discrepancy between experiments and simulations, we first determined how sensitive the equilibrium reaction conversion is to changes in these energies. To examine this relationship, we conducted a sensitivity analysis in the  $4\sigma$  slit pore at 160 K and 0.16 bar by modifying the interaction energies for the NO-wall and  $(\text{NO})_2$ -wall gradually and studied the effect of this change on the reaction conversion. The results are shown in Figures 3.2 and 3.3.

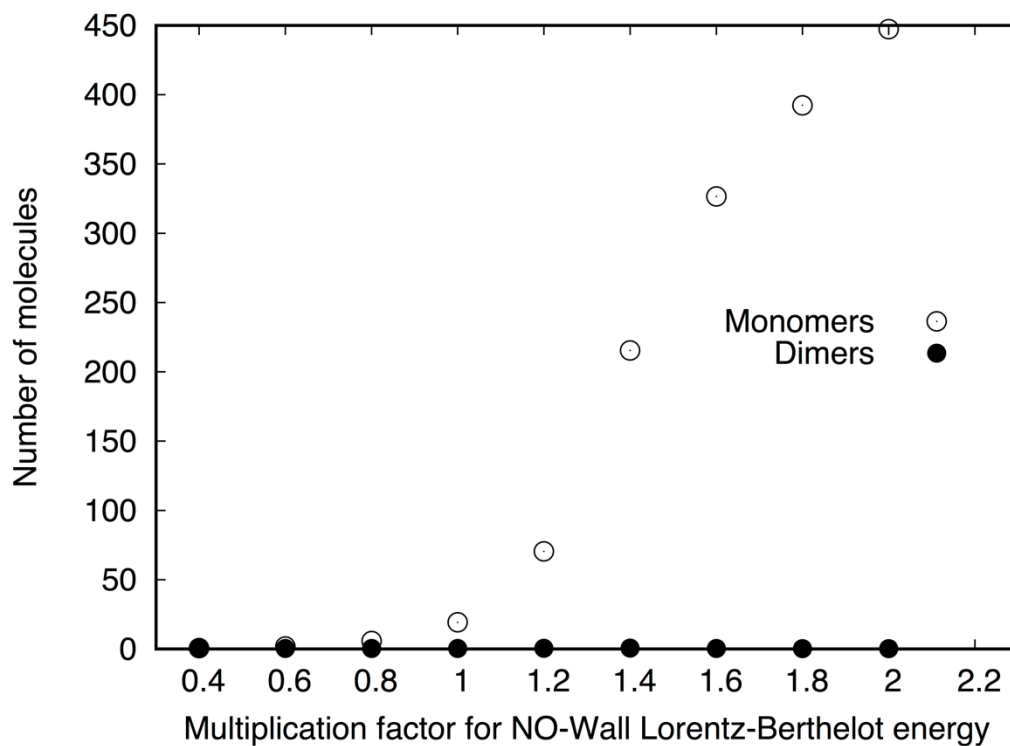


**Figure 3.2:** A sensitivity analysis on the effect of changing the interaction energy for the NO-wall interaction on the reaction conversion. A multiplication factor of 1 corresponds to the NO-wall interaction energy predicted by the Lorentz-Berthelot mixing rules. The  $(\text{NO})_2$ -wall interaction energy in these calculations was kept constant at the value predicted by the Lorentz-Berthelot rules.

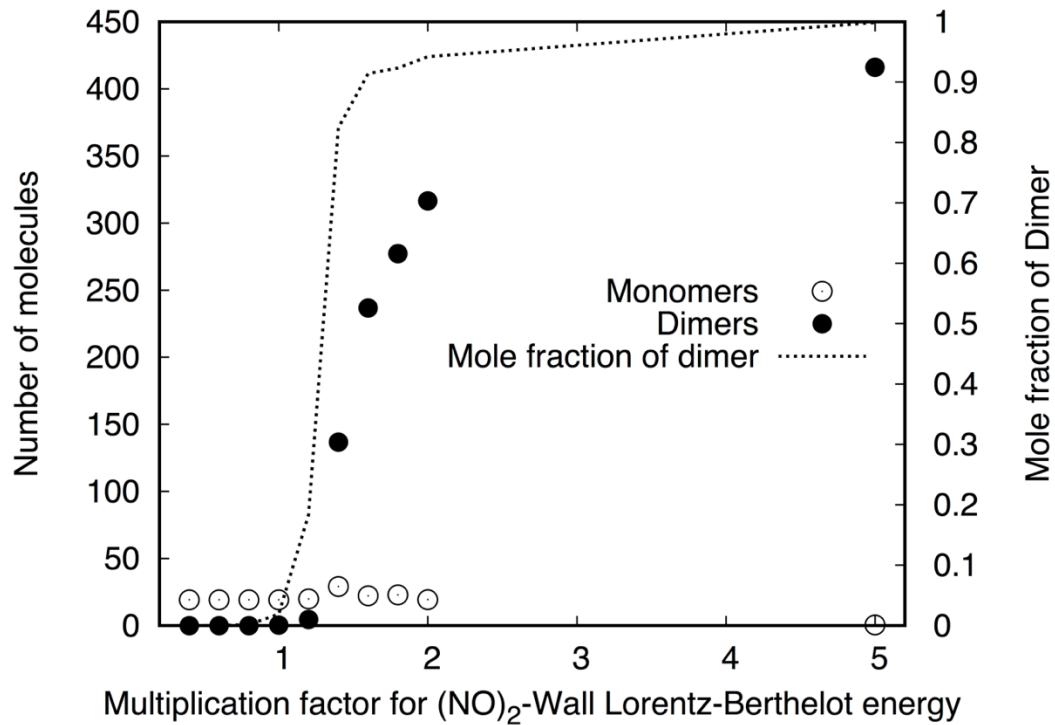


**Figure 3.3:** A sensitivity analysis on the effect of changing the interaction energy for the  $(\text{NO})_2$ -wall interaction on the reaction conversion. A multiplication factor of 1 corresponds to the  $(\text{NO})_2$ -wall interaction energy predicted by the Lorentz-Berthelot mixing rules. The  $\text{NO}$ -wall interaction energy in these calculations was kept constant at the value predicted by the Lorentz-Berthelot rules. The points show the number of molecules in the pore, and should be read on the left axis. The dotted line shows the mole fraction of dimer in the pore.

Both sensitivity plots show the reaction conversion to be quite sensitive to changes in the solid-fluid interaction energies. The reaction conversion displays high sensitivity to changes in the  $\text{NO}$ -wall interaction energy, which is expected since it is easier for them to transfer in and out of the pore due their smaller size. Simply doubling the Lorentz-Berthelot energy for the  $\text{NO}$ -wall interaction causes a more than 20-fold increase in the number of monomers in the pore, resulting in a system only consisting of monomers. The dimers also

exhibit notable sensitivity with the conversion increasing from nearly zero to a 94% dimer conversion when the energy of the dimer-wall interaction is doubled from the value obtained from the Lorentz-Berthelot mixing rules. It is important to recognize that while the conversion is affected by the magnitude of the adsorbate-wall interaction energies, it is also affected by the ratio of these energies. A higher  $\epsilon_{(\text{NO})_2}/\epsilon_{\text{NO}}$  ratio (*i.e.* a stronger  $(\text{NO})_2$ -wall energy compared to the  $(\text{NO})$ -wall energy) will favor the formation of dimers in the pore, leading to a greater dimer conversion. In Figure 3.3, when the interaction energy is increased to 5 times the Lorentz-Berthelot energy for the  $(\text{NO})_2$ -wall interactions, we see an almost 100% conversion in the pore. This implies that the energy of the dimer-wall interaction has to be at least 5 times stronger than the energy of the monomer-wall interaction in order for simulations to achieve the same reaction conversion as experiments.

In order to determine accurate interaction energies, we used MP2-level *ab initio* quantum mechanics theory to calculate the interaction energies for the adsorbate-wall interactions. These values are determined to be:

NO monomer and benzene ( $\epsilon_{\text{NO-w}}$ ): 966.28 K

$(\text{NO})_2$  and benzene, both sites ( $\epsilon_{(\text{NO})_2-w}$ ): 2536.64 K

$(\text{NO})_2$  and benzene, each site: 1268.32 K

The large magnitude of  $\epsilon_{(\text{NO})_2-w}$  signifies a weak chemical bond between the  $(\text{NO})_2$  dimer and the carbon wall, which is an effect not accounted for by the Lorentz-Berthelot mixing rules used in previous simulation studies of the NO dimerization reaction. Standard Lorentz-Berthelot combining rules yield a much smaller interaction energy for each interaction site of the monomers and dimers,  $\epsilon_{i\text{w}}/k = 59.16$  K, which is more indicative of a van der Waals

interaction. The stronger interaction energy for the dimer can be attributed to better charge-transfer stabilization due to  $\pi$ -binding between the  $(\text{NO})_2$  and the highest occupied molecular orbital (HOMO) of the benzene<sup>29</sup> (See Figure 3.4 below). The NO-benzene complex shows weaker electrostatic interactions, thus resulting in a lower interaction energy than the  $(\text{NO})_2$ -benzene complex.

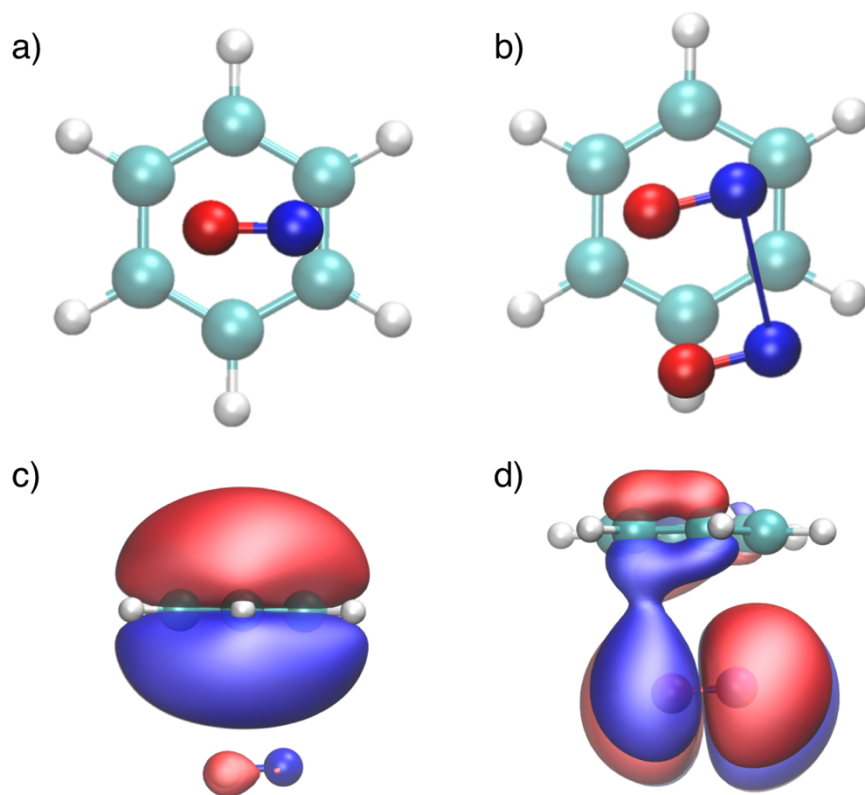


**Figure 3.4:** Left: Visualization of the (a) structure and (c) HOMO orbitals for the NO monomers. Right: Visualization of the (b) structure and (d) HOMO orbitals for the NO dimers.

### 3.3.2 Effect on Reaction Conversion

In order to account for the strong attractive interactions of the NO monomer and the (NO)<sub>2</sub> dimer with the carbon walls, we used LJ site-carbon interactions. The  $\sigma_{\text{NO-w}}$  and  $\sigma_{(\text{NO})_2\text{-w}}$  parameters were given by the Lorentz rule ( $\sigma_{\text{NO-w}} = \frac{\sigma_{\text{NO}} + \sigma_{\text{w}}}{2}$  and  $\sigma_{(\text{NO})_2\text{-w}} = \frac{\sigma_{(\text{NO})_2} + \sigma_{\text{w}}}{2}$ ), and  $\epsilon_{\text{NO-w}}$  and  $\epsilon_{(\text{NO})_2\text{-w}}$  parameters were determined in the MP2 calculations and given in the previous sub-section. In Figure 3.5, we show the NO dimerization conversion over the range of temperatures and pore sizes studied. As expected from experiments and previous simulation studies, confinement is shown to have a significant impact on the yield of the NO dimerization reaction. While reaction conversion in the bulk is consistently close to 0%, it is at least 120 times greater in the pores over the temperature range. This increase in conversion is a direct result of the stronger interaction between (NO)<sub>2</sub> and the pore walls, leading to an increased density of (NO)<sub>2</sub> molecules in the pore.

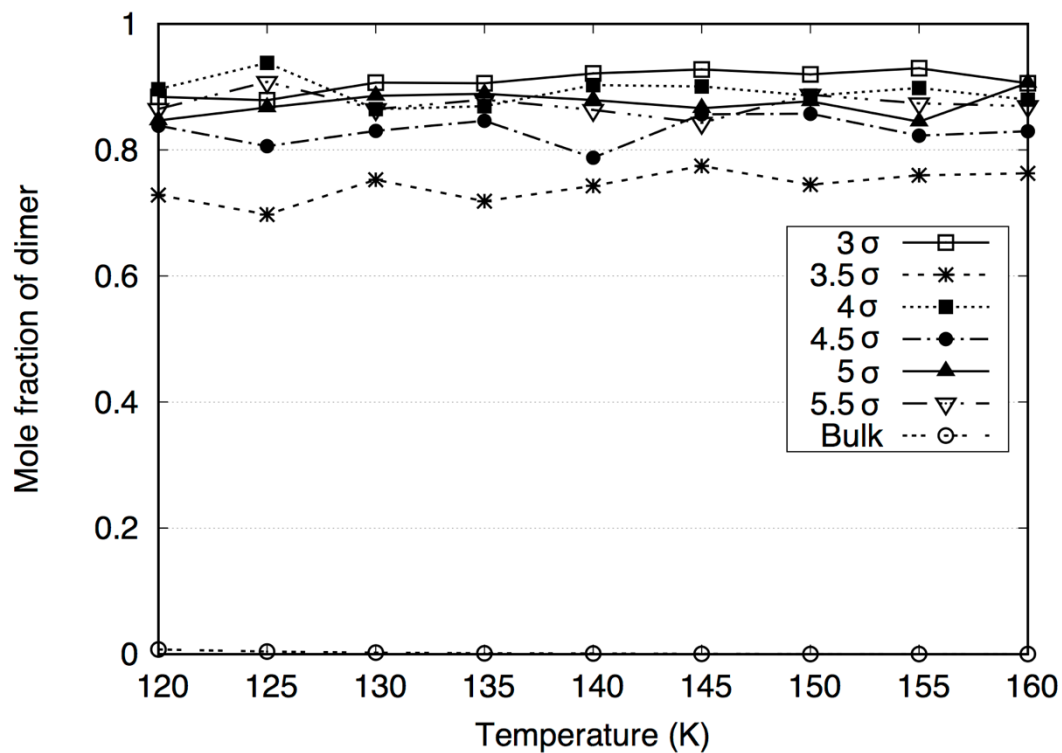


**Figure 3.5:** Reaction conversion in the bulk phase and different pore sizes from 120 K to 160 K.

While previous simulations showed the conversion of the reactions to decrease with increasing temperatures<sup>3,4</sup>, we observed very little temperature dependence on the reaction yield over the range of temperatures studied. The stronger interaction of the fluid molecules with the carbon walls makes it considerably more difficult for molecules to migrate from the pore phase to the bulk phase, leading to consistently high conversions. Furthermore, there does not seem to be a linear correlation between pore size and conversion, although the width of the pore does seem to affect the reaction yield to some extent. In general, we found that pore widths of  $3\sigma$ ,  $4\sigma$ , and  $5\sigma$  exhibit the highest reaction yield, with the reaction conversion hovering

close to 90%. A pore width of  $3.5\sigma$  shows the lowest reaction yield, with the average reaction conversion being around 74%. We believe these differences in yield for pore widths of integral and non-integral multiples of  $\sigma$  are a result of packing effects, with the overall density in the pores being higher for the integral sigma widths. Figure 3.6 shows a plot of the average conversion over the studied temperature range vs pore width, demonstrating that the magnitude of the oscillations in conversion becomes smaller with increasing pore width i.e. for pore sizes greater than  $4\sigma$ , further increases in the pore width have a smaller influence on the conversion. This is expected because as the pore width expands, the interaction between the pore walls and the molecules closer to the center becomes weaker.

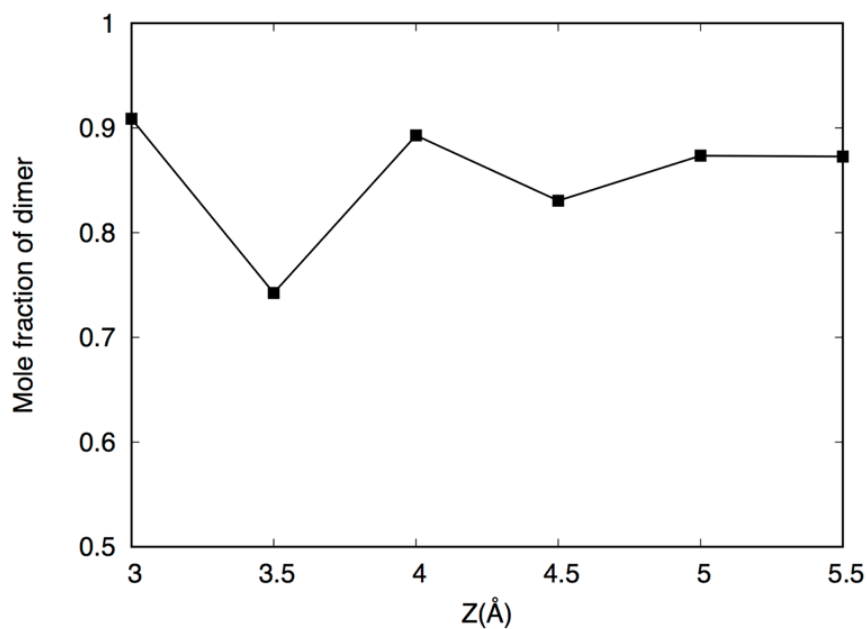


**Figure 3.6:** Average reaction conversion vs. pore width at  $P_{\text{bulk}} = 0.16$  bar.

In order to better understand the oscillatory behavior in smaller pores, it is helpful to look at the configurations in the pore (see Figure 3.7). The green spheres represent the centers of mass

for the  $(\text{NO})_2$  dimer, the purple spheres are the NO monomers, and the blue spheres are the LJ interaction sites for both the monomers and dimers.

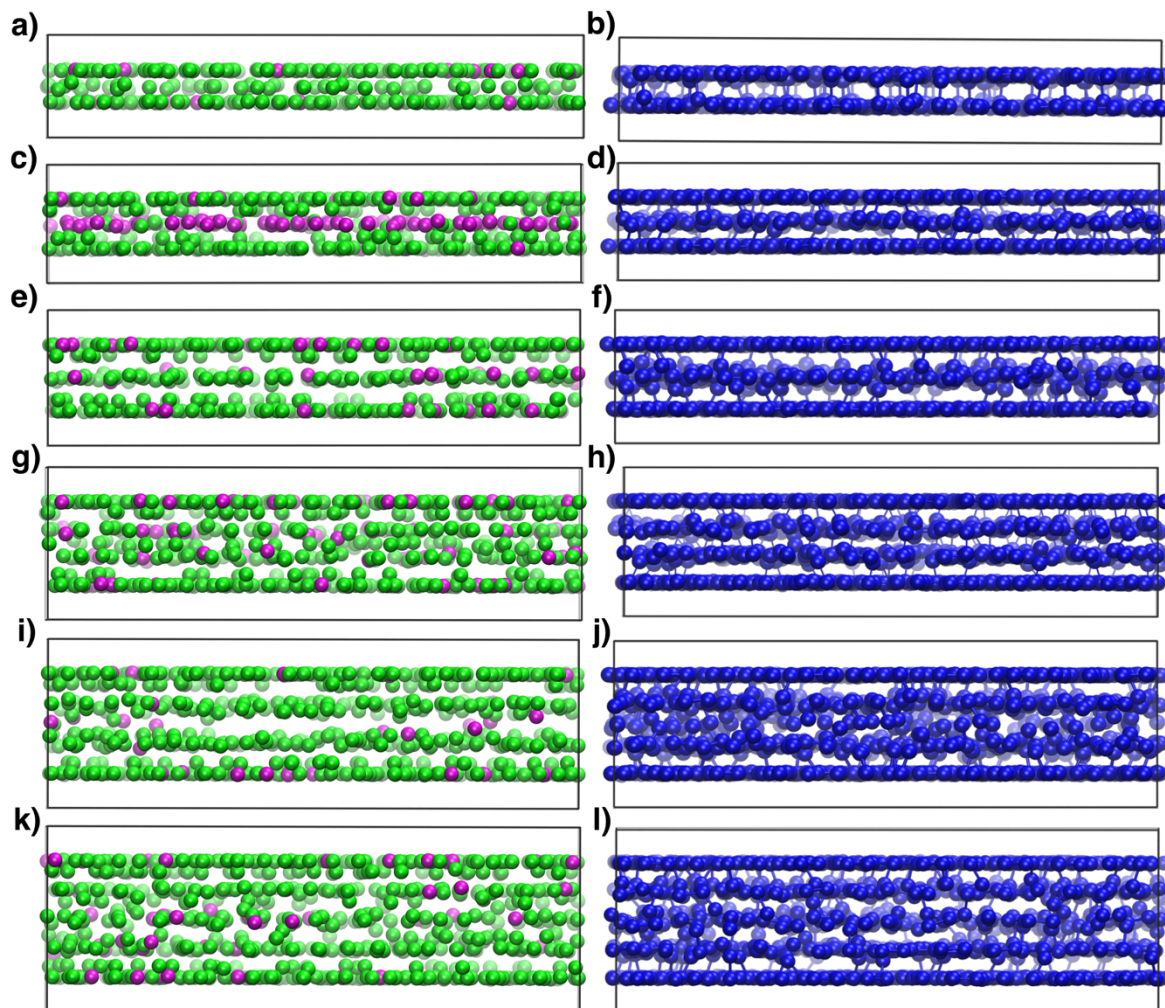


**Figure 3.7:** *Left:* Configurations of the center of mass in (a)  $3\sigma$ , (c)  $3.5\sigma$ , (e)  $4\sigma$ , (g)  $4.5\sigma$ , (i)  $5\sigma$  and (k)  $5.5\sigma$  pore, respectively at 160 K. Orange molecules are monomers and blue molecules are dimers. *Right:* Configurations of the molecular sites in (b)  $3\sigma$ , (d)  $3.5\sigma$ , (f)  $4\sigma$ , (h)  $4.5\sigma$ , (j)  $5\sigma$  and (l)  $5.5\sigma$  pore, respectively at 160 K. The green spheres represent the centers of the  $(\text{NO})_2$  dimers, while purple spheres indicate the NO monomers. The dark blue spheres are the LJ sites in the NO and  $(\text{NO})_2$  molecules.

In the  $3\sigma$  pore (Figure 3.7(a) and 3.7(b)), the pore is just wide enough to allow two layers of molecule sites to fit into the pore. Firstly, it is important to recognize that due to the extremely strong interaction of the dimers with the pore wall, the equilibrium inside the pore will always attempt to shift towards dimer conversion as long as they can fit into the pore. In the  $3\sigma$  pore, the distance between the two layers ( $\sim 3 \text{ \AA}$ ) is just large enough to allow dimers to rotate vertically and have each site be close to a pore wall, maximizing packing efficiency in the  $xy$  plane (Figure 3.7(b)). However, if the pore size is increased by  $0.5\sigma$  as shown in Figures 3.7(c) and 3.7(d), the pore becomes just big enough to accommodate three site layers that are more closely packed together in the  $z$  direction. The dimers tend to gravitate towards the outer layers and lie flat against the pore walls to maximize their interactions with them. The interlayer spacing is now smaller ( $\sim 2.3 \text{ \AA}$ ), which is only slightly larger than the dimer bond length of  $2.25 \text{ \AA}$ . This makes it significantly more difficult for dimers to fit near the center of the pore, and allows the less bulky monomers to fill in that space, effectively decreasing the reaction conversion. As the pore size increases to  $4\sigma$  in Figures 3.7(e) and 3.7(f), the larger interlayer spacing ( $\sim 3 \text{ \AA}$ ) allows more dimers to enter the pore and rotate to increase packing efficiency, thereby increasing the pore density and bringing the conversion back up closer to 90%. This leads to a less aligned center layer as seen in Figure 3.7(f).

While the  $3.5\sigma$  pore exhibited the start of the formation of 3 layers, a similar situation is seen with the  $4.5\sigma$  pore in Figure 3.7(g) and 3.7(h), which see the formation of 4 molecular layers in the pore. The layers are, again, forced to be more closely packed together resulting in an interlayer distance of roughly  $2.6 \text{ \AA}$ . Because the close proximity of the layers to each other

is still quite restrictive for the dimers, we see a slight decrease in conversion for the  $4.5\sigma$  pore when compared to the  $4\sigma$  pore. However, we see a higher conversion for the  $4.5\sigma$  when compared to the  $3.5\sigma$  pore due to the larger pore width which can accommodate more dimers in the center layers. In the case of  $5.5\sigma$  in Figure 3.7(k) and 3.7(l), the pore is large enough to allow more distance between the layers, leading to a slightly higher conversion than the  $4.5\sigma$  pore and almost the same conversion as the  $5\sigma$  pore. It's a well-documented trend that as the pore size gets larger, the wall effects get less prominent for the center layers. However, in previous studies, this resulted in molecules getting out of the pore leaving little to no molecules in the center layers. We show here that when the fluid-wall interactions are stronger, multi-site molecules such as NO dimers are able to move more freely to maximize their interactions with the carbon walls, thus still maintaining a high reaction conversion even at higher temperatures, which is significantly different from the effect observed in previous simulation studies. We also studied the reaction in a pore of width  $8.5 \text{ \AA}$  at a temperature of 298 K and a pressure of 0.8 bar, the same conditions used by Kaneko *et al.*<sup>1</sup> experimentally. We obtained a conversion of 77%, which is significantly higher than the 22% conversion found by Turner *et al.*<sup>3</sup> in the previous simulation study. However, while the discrepancy between simulations and experiments has been reduced enormously, the conversions we see are still lower than the 98% conversion observed experimentally. This is likely due to the fact that the interaction between the adsorbate molecules, especially the  $(\text{NO})_2$  dimer, and the graphene sheet is expected to be stronger than the interaction predicted by using a single benzene molecule in the MP2 simulations. A stronger dimer-wall interaction would make it more difficult for dimers to

convert into monomers. and would decrease the likelihood of molecules migrating out of the pore, even at higher temperatures and would result in a higher conversion.

### *3.3.3 Effect on Slit-Pore Pressure Tensor*

We have shown in Chapter 2 that confinement effects in the pore can also affect the in-pore pressure. However, while studies have focused on the effect of pore shape, size, and temperature on the pressure tensor for one-component fluids, the effect of confinement on the pressure for mixtures is still a relatively unexplored area. Figure 3.8 shows our results for the in-pore pressure tensor in various pores for the NO dimerization reaction at 160 K. In general, the normal pressure is constant, as expected from the condition of hydrostatic equilibrium, whereas the tangential pressures peak to extremely high values ranging from 500,000 bar to 2.3 million bar. The tangential pressures follow the same profile as the reduced density,  $\rho^* = (N/V)\sigma^3$ , indicating that the peaks in the tangential pressure profile are directly related to the layers of fluid molecules. The high tangential pressures can be explained by looking at the average separation distance between molecular sites in the contact layer. Figure 3.9(a) shows the radial distribution function for the  $5\sigma$  pore at 160 K in the  $xy$  plane. The first peak correlates to the dimer bond length of 2.25 Å while the second peak at 2.95 Å correlates to the most likely separation distance between neighboring LJ interaction sites on two nearest neighbor molecules in the contact layer next to the wall. In Figure 3.9(b), we highlight this distance on the intermolecular force plot for NO and it is obvious that it falls in the steeply repulsive region of the Lennard-Jones force profile. The high repulsive forces between the fluid molecules in the  $xy$  plane leads to the extremely high tangential pressure peaks in the contact layers.

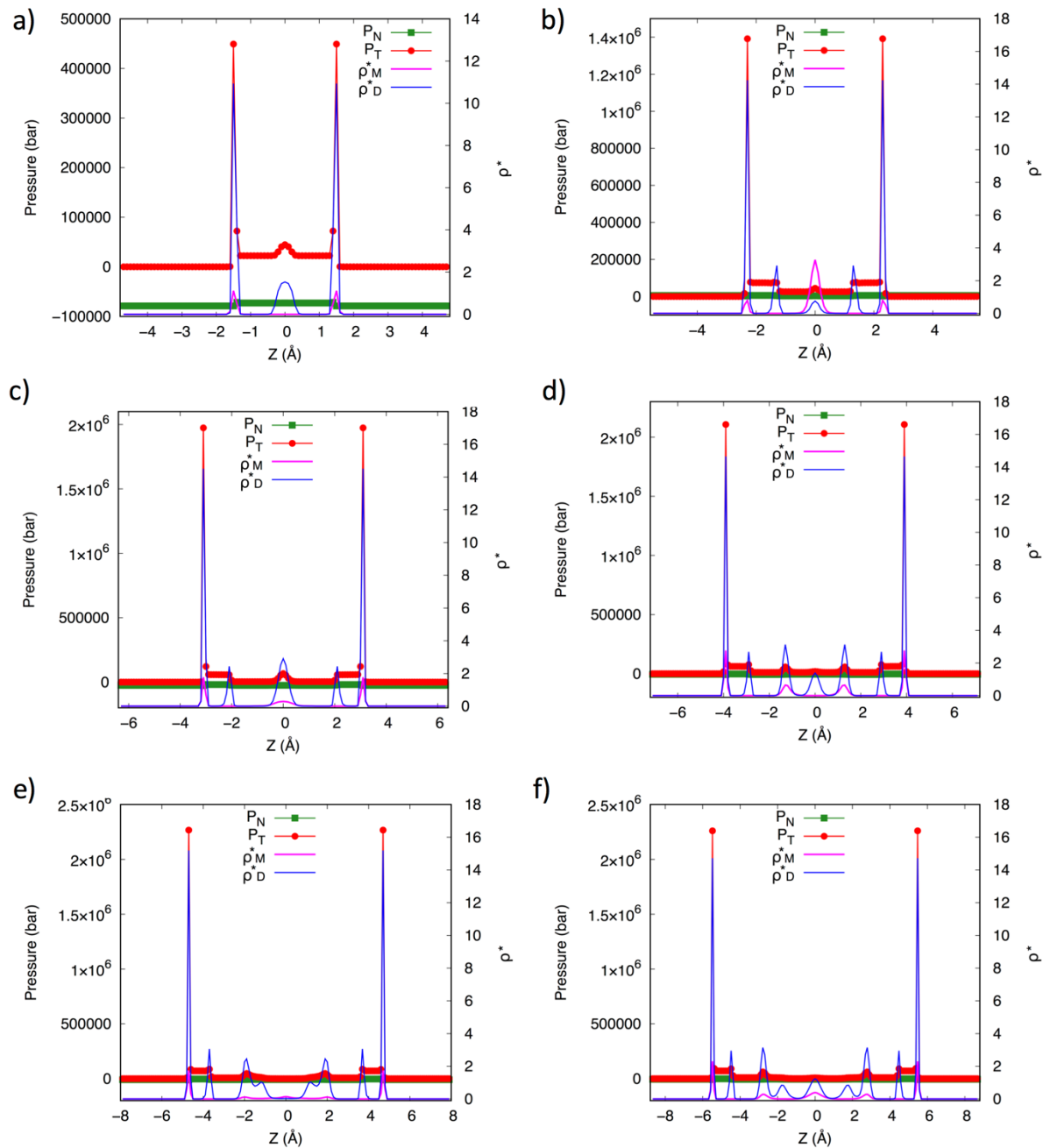


**Figure 3.8:** Pressure and density profiles for all 6 pore sizes at 160 K:  $3\sigma$  (top left),  $3.5\sigma$  (top right),  $4\sigma$  (center left),  $4.5\sigma$  (center right),  $5\sigma$  (bottom left),  $5.5\sigma$  (bottom right). Blue lines represent the NO dimer reduced density and orange lines represent the NO monomer reduced density. The red lines are the tangential pressure and green lines are the normal pressure.

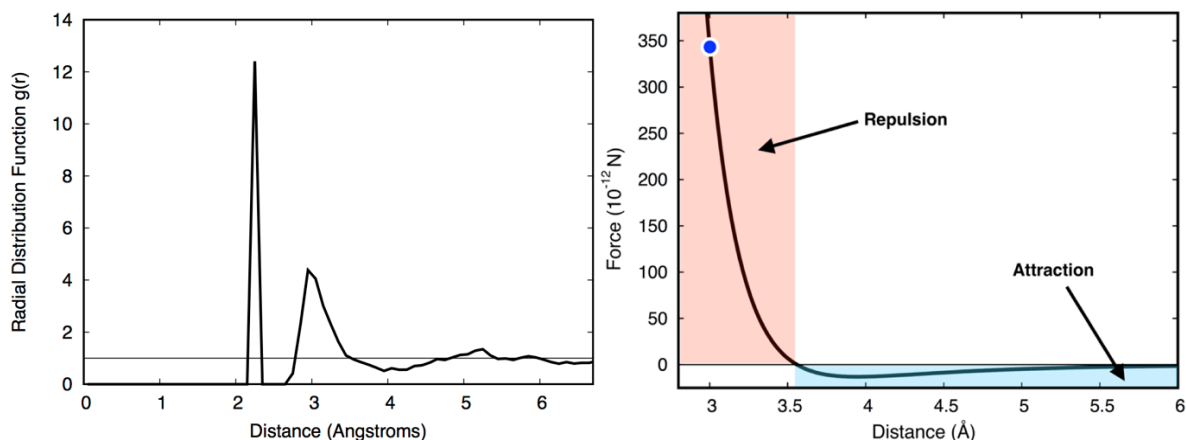


**Figure 3.9:** (a) Left: radial distribution function for the LJ sites for the  $5\sigma$  pore at 160 K in the xy plane. (b) Right: Intermolecular force plot for the interaction between two LJ sites on different molecules, showing the repulsive and attractive regions. The blue dot indicates the most probable site separation distance for  $5\sigma$  pore at 160 K.

There are three configurational contributions to the tangential pressure in our Steele slit-pore model: interactions between two monomers (NO-NO interactions), interactions between two dimers ( $(\text{NO})_2$ - $(\text{NO})_2$  interactions) and interactions between monomers and dimers (NO- $(\text{NO})_2$ ). The interactions of the NO and  $(\text{NO})_2$  molecules with the pore walls do not contribute directly to the tangential pressure, since for the (10,4,3) wall model these forces act only in the  $z$  direction. The individual contributions to the tangential pressure for the  $5\sigma$  pore at 160 K are shown in Figure 3.12. It can be seen that the most prominent contribution to the tangential pressure is from the  $(\text{NO})_2$ - $(\text{NO})_2$  interactions. This is due mainly to the much larger number of dimers than monomers in the pore. In addition, each dimer consists of two interacting sites, leading to even more contributions and the fluid-wall interaction energy for the dimer is also stronger. The contributions from the NO- $(\text{NO})_2$  interactions and the NO-NO

interactions are almost negligible, which makes sense given the low number of NO monomers in the pore. In general, as the pore width gets larger, the pressure in the pore also increases due to the increased number of molecules in the pore, allowing for more fluid-fluid interactions contributing to the tangential pressure. A similar phenomenon is observed in our study of the pressure tensor in Chapter 2.

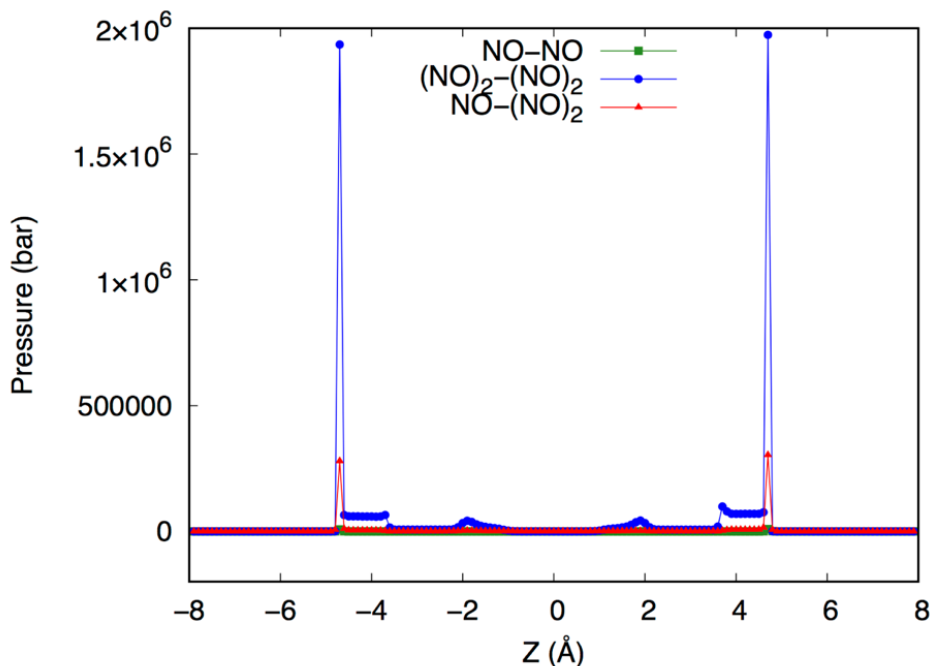


**Figure 3.10:** Individual configurational contributions to the tangential pressure tensor for the  $5\sigma$  pore at 160 K.

In addition to being able to accommodate a higher number of layers, larger pores also allow for more dimer rotations enabling the molecules to maximize their interaction with the walls. This not only enables more dimers to enter the pore, but also results in closer packing in the contact layers and uneven layering in the center. In Figure 3.8, the sharp peaks in the

tangential pressure near the pore walls indicate well-aligned layers that line up perfectly with the peaks in the density profile. Most of the dimers in this layer are lying flat against the wall to maximize their interaction. The broad shoulders arising from the sharp peaks is a recently discovered effect that has been discussed in our other study of multi-site molecules in Chapter 2. It is due to the rotation of the dimer molecules which results in a non-integer number of molecular layers in the pore. This effect is not observed for single-site molecules since their lack of orientation results in well-aligned layers throughout the pore width. In general, the prominence of the broad shoulders is dependent on the ratio of dimers that are oriented in non-horizontal directions to the dimers that are lying flat against the wall.

The  $3\sigma$  pore is a particularly interesting case because it's the only scenario where the normal pressure isn't constant, as dictated by the condition of hydrostatic equilibrium. It is important to note that the hydrostatic equilibrium condition is only valid for fluids, and not for solids or crystalline phases. Due to the small width of the  $3\sigma$  pore, it is likely that the fluid in the pore is freezing into a crystalline phase. Looking at the configuration in the  $xy$  plane in Figure 3.11, there are clearly regions of alignment with the dimers, which could indicate the formation of a defective crystal due to the rigidity of the bonds in the dimer. The extremely negative pressure indicates a strong attractive force between the fluid layers and between the layers and the pore wall.

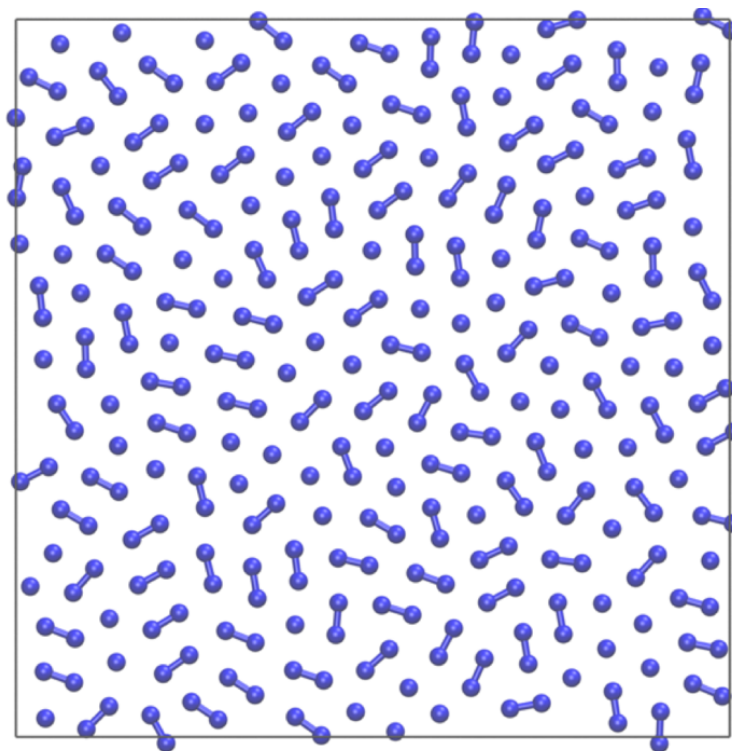


**Figure 3.11:** Configuration of NO molecules in the  $xy$  plane for the  $3\sigma$  slit pore at 160 K.

### *3.3.4 NO Dimerization in Cylindrical Pores*

The effect of confinement on the NO dimerization in cylindrical pores is expected to be more pronounced for a given pore size, than for slit-pores, because the system is now confined in two dimensions than one. In Figure 3.12, shows the conversions for our simulations of the NO dimerization in the (8,8) and (10,10) nanotube bundles under the same conditions as those used for the slit-shaped pores. We find the NO conversion to stay between 86 and 89% for the (10,10) bundle, again not showing any significant temperature dependency. The (8,8) bundle shows a higher conversion ranging from 94 to 98%, indicating that the diameter of the nanotubes has an appreciable impact on the reaction conversion. In comparison, experimental

studies by Byl et al.<sup>2</sup> of the NO dimerization reaction in the (10,10) nanotube bundle under similar temperatures (103 – 136 K) and found an almost 100% conversion, with no detectable temperature dependence in the range studied.

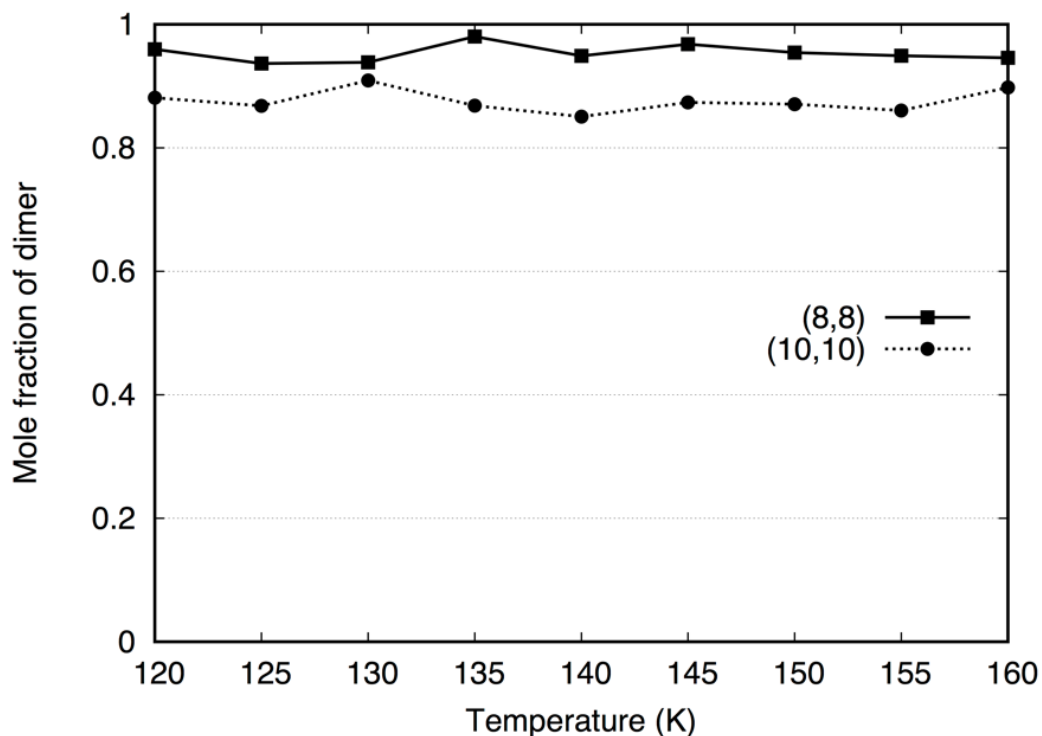


**Figure 3.12:** Conversion of the NO dimerization reaction in (8,8) and (10,10) nanotube bundles. Simulation temperatures ranged from 120 – 160 K. The bulk pressure was kept constant at 0.16 bar.

In order to understand the effect of the nanotube diameter on the conversion, it is useful to look at the configurations in the bundles. Figure 3.15 shows simulation snapshots of the NO molecules for the (8,8) and (10,10) nanotube bundles. Figure 3.13(a) and Figure 3.13(b) show the configurations for the molecular interaction sites and centers of mass, respectively, in the

(8,8) nanotube bundle. Figures 3.13(c) and (d) show the configurations for the molecular interaction sites and centers of masses, respectively, in the (10,10) nanotube bundle. The blue molecules represent the molecular sites (with each site representing a LJ site in a nitric oxide monomer or in a dimer), the purple molecules represent the NO monomers and the green molecules represent the center of mass for the NO dimers.

Figures 3.13a) and 3.13c) show that while the (8,8) nanotubes are able to accommodate only one ring of molecular sites, the larger diameter of the (10,10) nanotubes allows additional molecular sites to accumulate near the center. Figures 3.13(b) and 3.13(d) confirm that the vast majority of molecules inside the nanotubes are NO dimers (green) with a select few NO monomers (purple) scattered around the bundle. The confinement effect in the (8,8) nanotubes is more enhanced than in the (10,10) bundle due to the existence of only one layer of adsorbate molecules interacting with the carbon wall. Similar to slit pores, layers closer to the center of the nanotube would experience a weaker interaction with the wall resulting in fewer dimers and therefore, a lower conversion. In addition, the (10,10) bundle also allows molecules to adsorb in the interstitial space between neighboring nanotubes, and Figure 3.13(d) shows that the molecules in this space can be either monomers or dimers. Even though the intertubular distance for the (8,8) and (10,10) bundles is the same (3.4 Å), the larger diameter in the (10,10) bundle creates a larger space at the intersection of three nanotubes.

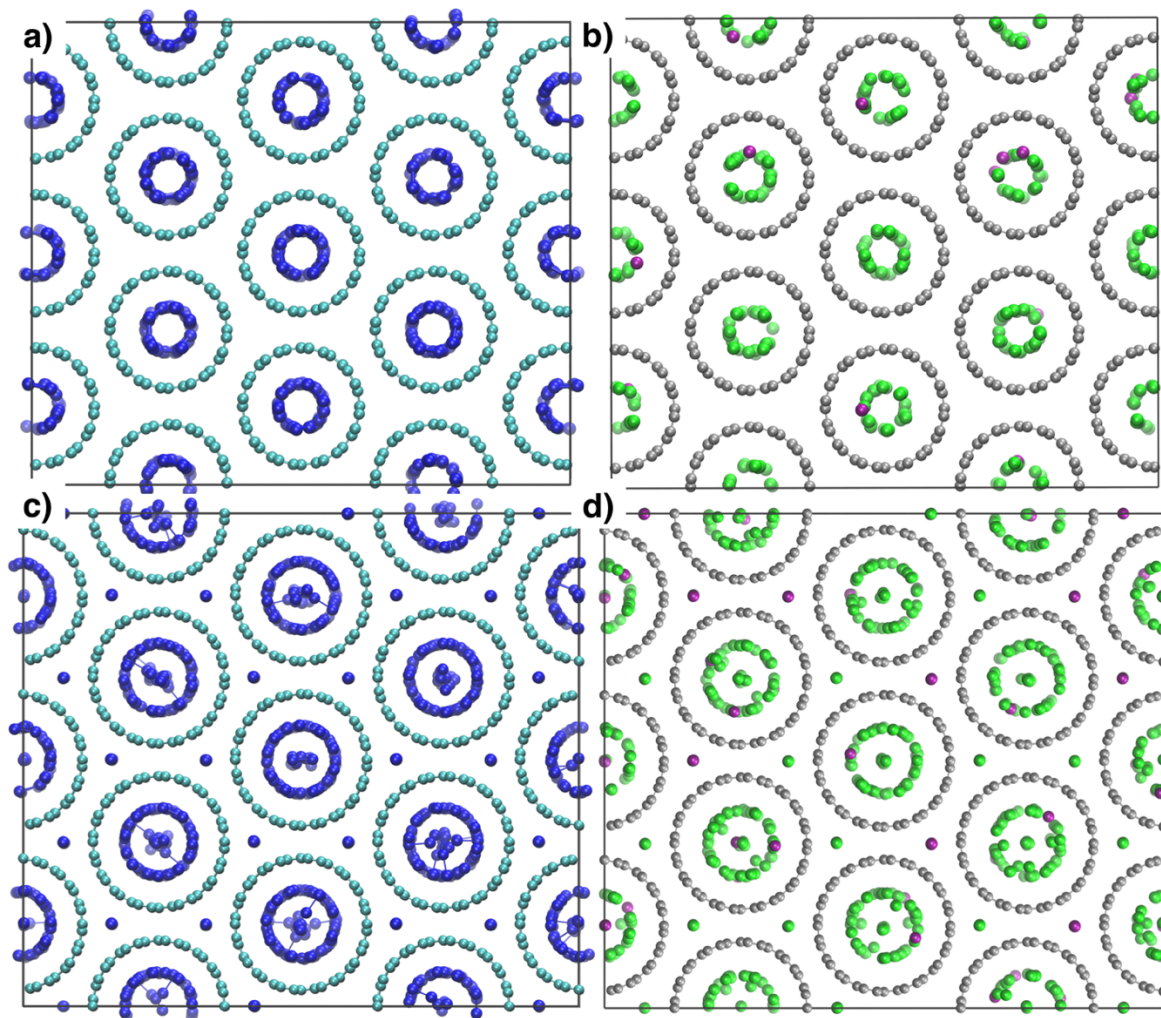


**Figure 3.13:** Simulation snapshots of the NO dimerization reaction in the carbon nanotube bundles. a) configuration of the molecular interaction sites in the (8,8) bundle, b) configuration of the centers of mass in the (8,8) bundle, c) configuration of the molecular interaction sites in the (10,10) bundle, d) configuration of the centers of mass in the (10,10) bundle. In Figures (a) and (c), the dark blue spheres are the LJ sites in the NO and  $(\text{NO})_2$  molecules. In Figures (b) and (d), green spheres represent the centers of the  $(\text{NO})_2$  dimers, while purple spheres indicate the NO monomers.

It is interesting to note that the conversion in the center nanotube is higher than the overall conversion in the nanotube bundle. Figures 3.14(a) and 3.14(b) show the number density profile for the (8,8) and (10,10) center nanotubes, respectively. For the x-axis,  $r = 0$  is the center of the nanotube. It can be seen that the (8,8) nanotube consists exclusively of dimers while the (10,10) nanotube contains more than 98% dimers.

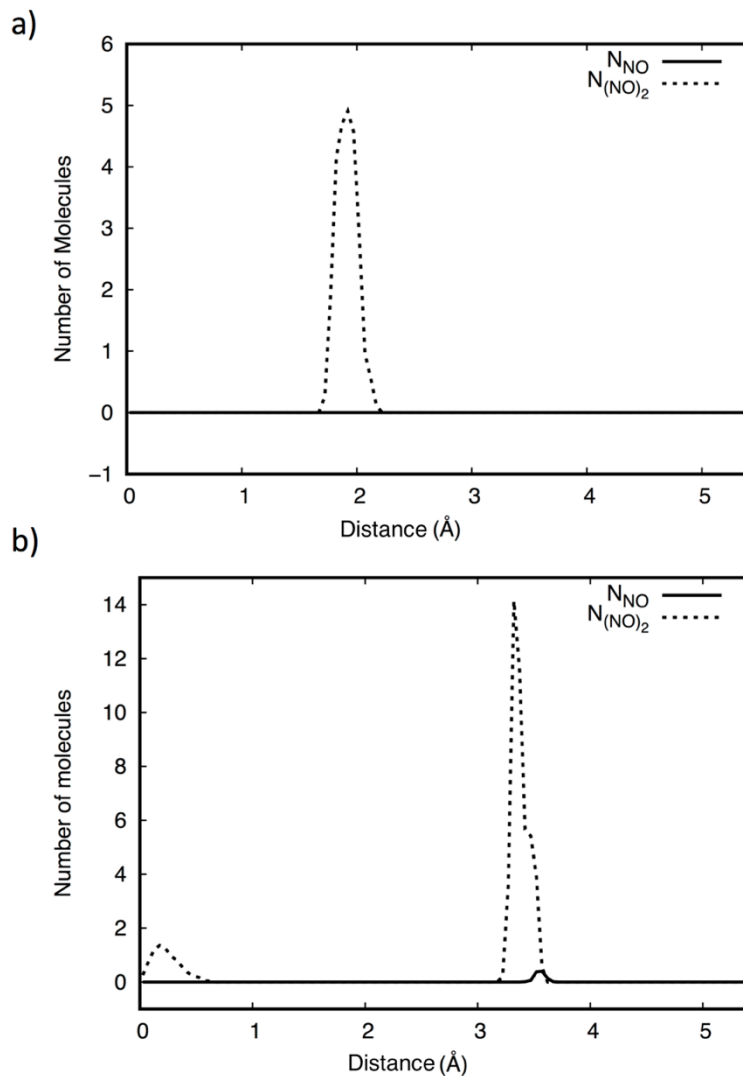


**Figure 3.14:** (a) Number density profile for the (8,8) center nanotube (b) Number density profile for the (10,10) center nanotube

While periodic boundaries are applied in all 3 directions, it is possible that slight edge effects come into play due to the cutting of the hexagonal lattice bundle to fit a rectangular simulation. These could potentially cause the nanotubes closer to the edges of the bundle to feel a marginally smaller confinement effect than the nanotube in the center, resulting in a higher conversion in the nanotube in the center.

### **3.4 Conclusion**

Through *ab initio* calculations and Reactive Monte Carlo simulations, we have identified the presence of strong interaction energies between the nitric oxide dimer and the carbon atoms present in the graphene wall. Using Gaussian 09, we obtain significantly more accurate energy parameters for these strong interactions between the nitric oxide dimer molecules and the carbon wall. Accounting for these strong interaction energies notably lowers the discrepancy between prior simulations and experimental data, and yields reaction conversions within 10% of the experimental conversions in slit-shaped pores. In addition, no temperature dependency was observed over the temperature range studied, again consistent with experimental data. Greatly increased reaction conversion was also observed in carbon nanotubes, and the confinement effect was significantly as the nanotube diameter decreased, with conversions reaching as high as 98% in the (8,8) nanotube bundle.

### **3.5 Acknowledgement**

We thank the National Science Foundation for their continued support and funding of this work through grant CBET-1603851. We would also like to acknowledge Dr. Heath Turner

from the University of Alabama for helpful discussions, and for assisting us through his previous work on the nitric oxide dimerization reaction.

### 3.5 References

1. Kaneko, K., Fukuzaki, N., Kakei, K., Suzuki, T. & Ozeki, S. Enhancement of nitric oxide dimerization by micropore fields of activated carbon fibers. *Langmuir* **5**, 960–965 (1989).
2. Byl, O., Kondratyuk, P. & Yates, J. T. Adsorption and Dimerization of NO Inside Single-Walled Carbon Nanotubes - An Infrared Spectroscopic Study. *J. Phys. Chem. B* **107**, 4277–4279 (2003).
3. Turner, C. H., Johnson, J. K. & Gubbins, K. E. Effect of confinement on chemical reaction equilibria: The reactions  $2\text{NO} \rightleftharpoons (\text{NO})_2$  and  $\text{N}_2 + 3\text{H}_2 \rightleftharpoons 2\text{NH}_3$  in carbon micropores. *J. Chem. Phys.* **114**, 1851–1859 (2001).
4. Tripathi, S. & Chapman, W. G. A density functional approach to chemical reaction equilibria in confined systems: Application to dimerization. *J. Chem. Phys.* **118**, 7993–8003 (2003).
5. Turner, C. H., Brennan, J. K., Johnson, J. K. & Gubbins, K. E. Effect of confinement by porous materials on chemical reaction kinetics. *J. Chem. Phys.* **116**, 2138–2148 (2002).
6. Kostov, M. K., Santiso, E. E., George, A. M., Gubbins, K. E. & Nardelli, M. B. Dissociation of Water on Defective Carbon Substrates. *Phys. Rev. Lett.* **95**, 136105 (2005).
7. Santiso, E. E., Kostov, M. K., George, A. M., Nardelli, M. B. & Gubbins, K. E. Confinement effects on chemical reactions—Toward an integrated rational catalyst design. *Appl. Surf. Sci.* **253**, 5570–5579 (2007).

8. Santiso, E. E., Buongiorno Nardelli, M. & Gubbins, K. E. A remarkable shape-catalytic effect of confinement on the rotational isomerization of small hydrocarbons. *J. Chem. Phys.* **128**, 34704 (2008).
9. Fujimori, T. *et al.* Conducting linear chains of sulphur inside carbon nanotubes. *Nat. Commun.* **4**, (2013).
10. Fujimori, T. *et al.* Formation and Properties of Selenium Double-Helices inside Double-Wall Carbon Nanotubes: Experiment and Theory. *ACS Nano* **7**, 5607–5613 (2013).
11. Santiso, E. E. Understanding the effect of adsorption on activated processes using molecular theory and simulation. *Mol. Simul.* **40**, 664–677 (2014).
12. Huang, L., Santiso, E. E., Nardelli, M. B. & Gubbins, K. E. Catalytic role of carbons in methane decomposition for CO- and CO<sub>2</sub>-free hydrogen generation. *J. Chem. Phys.* **128**, 214702 (2008).
13. Addington, C. K., Mansell, J. M. & Gubbins, K. E. Computer simulation of conductive linear sulfur chains confined in carbon nanotubes. *Mol. Simul.* **43**, 519–525 (2017).
14. Johnson, J. K., Panagiotopoulos, A. Z. & Gubbins, K. E. Reactive canonical Monte Carlo. *Mol. Phys.* **81**, 717–733 (1994).
15. Smith, A. L. & Johnston, H. L. The Magnetic Susceptibility of Liquid Nitric Oxide and the Heat of Dissociation of (NO)<sub>2</sub><sup>1</sup>. *J. Am. Chem. Soc.* **74**, 4696–4698 (1952).
16. Guedes, H. J. R. Propriedades Termodinamicas de Sistemas Liquidos. Simples. (Universidade Nova de Lisboa, 1988).

17. Kohler, F., Bohn, M., Fischer, J. & Zimmermann, R. The excess properties of nitric oxid mixtures. *Monatshefte für Chemie Chem. Mon.* **118**, 169–182 (1987).
18. Panagiotopoulos, A. Z. Adsorption and capillary condensation of fluids in cylindrical pores by Monte Carlo simulation in the Gibbs ensemble. *Mol. Phys.* **62**, 701–719 (1987).
19. McGrother, S. C. & Gubbins, K. E. Constant pressure Gibbs ensemble Monte Carlo simulations of adsorption into narrow pores. *Mol. Phys.* **97**, 955–965 (1999).
20. Steele, W. A. The physical interaction of gases with crystalline solids. *Surf. Sci.* **36**, 317–352 (1973).
21. Lísal, M., Brennan, J. K. & Smith, W. R. Chemical reaction equilibrium in nanoporous materials: NO dimerization reaction in carbon slit nanopores. *J. Chem. Phys.* **124**, 64712 (2006).
22. Turner, C. H. Computer Simulation of Chemical Reactions in Porous Materials. Ph.D. Dissertation. (North Carolina State University, 2002).
23. Steele, W. A. *The Interaction of Gases with Solid Surfaces*. (Pergamon Press, 1974).
24. Lorentz, H. A. Ueber die Anwendung des Satzes vom Virial in der kinetischen Theorie der Gase. *Ann. Phys.* **248**, 127–136 (1881).
25. Berthelot, D. Sur le mélange des gaz. *Comptes rendus Hebd. des séances l'Académie des Sci.* **126**, 1703–1855 (1898).
26. Kukolich, S. G. Structure of the NO Dimer. *J. Am. Chem. SOC* **104**, 4715–4716 (1982).
27. Gray, C., Gubbins, K. & Joslin, C. in *Oxford Science Publications* Sec. 83 (Oxford

University Press, 2011).

28. Smith, A. L., Keller, W. E. & Johnston, H. L. The Infrared and Raman Spectra of Condensed Nitric Oxide. *J. Chem. Phys.* **19**, 189–192 (1951).
29. Zhao, Y. L. *et al.* Theoretical evidence for enhanced NO dimerization in aromatic hosts: Implications for the role of the electrophile (NO)<sub>2</sub> in nitric oxide chemistry. *J. Am. Chem. Soc.* **127**, 7964–7965 (2005).

## **CHAPTER 3 : Computationally mapping pKa shifts due to the presence of a polyelectrolyte chain around milk proteins**

### **4.1 Introduction**

Since the initial application of statistical mechanics to the study of atomic and molecular fluids in the earlier 70's<sup>1</sup>, practical applications in industry and biomedical sciences continue to drive the field of complex fluids to a broad, challenging and inherently multidisciplinary arena. Experiments have observed new effects in molecular phenomena, especially in mixtures involving more complicated microstructures, such as charged macromolecules with colloidal dimensions (e.g. proteins, polyelectrolytes, nucleic acids, etc.). The phase behavior of systems containing such macromolecules is of great interest in areas related to food and bioprocess technology, such as food science, brewing, pharmaceuticals, cosmetics and biomaterials.<sup>2-6</sup> Protein-polyelectrolyte complexation is a central topic in this context. Examples of applications include the encapsulation of active ingredients for food and medicinal drugs, stabilization of food emulsions (used in the production of soft drinks and ice cream products) and bioseparation processes. Moreover, protein-polysaccharide interactions also play important roles in living cells.<sup>7-19</sup> Consequentially, the understanding of protein-polyelectrolyte association mechanisms is essential in order to rationalize the molecular organization determining protein functionality in the aforementioned applications.

Despite the tremendous amount of experimental work conducted in both applied and model systems, there is still relatively little theoretical and modeling data to aid in the understanding of the molecular mechanisms of protein-polyelectrolyte complexation.

Simulation studies carried out by Linse, Stoll, de Vries and collaborators provide valuable contributions in enhancing our theoretical understanding of such complex systems.<sup>20</sup> Most of these works invoke a simplified colloidal-like molecular description of the system, which explores particular aspects of the problem. Nevertheless, simulations need a higher level of detail, within reasonable computing requirements, in order to be useful in designing practical functionalized systems. A delicate aspect in the simulation of protein-polyelectrolyte systems is the accurate description of the pH effects, which play a major role in practical applications, without hampering the computational costs.<sup>21</sup> Since pH is directly related to electrostatic interactions, it controls a diversity of molecular mechanisms, from enzyme activity to product stability,<sup>3,22,23</sup> making it fundamental to include a proton titration scheme in molecular models. From an applied perspective, a current issue for the food protein community is the relative difficulty in using existing theoretical data from the physical chemical literature for practical interpretation and use. Part of this struggle is due to the oversimplified idealization assumed in the physical chemical approaches and the different hierarchical structural scales<sup>24</sup> between molecular physical descriptions and real food macroscales where a desired function should be achieved. Moreover, the use of high-level theory from statistical and mechanical theories often makes it difficult for data to be understood by different communities. It is our intention to study the interactions between whey proteins and polyelectrolytes at different pH regimes and provide simplified data that is of interest to help to rationalize, in a simpler manner, important processes in food chemistry.

Theoretical attempts to address this class of problems started a long time ago<sup>25</sup>. After the success of the first study of complexation of oppositely charged biopolymers led by Voorn

& Overbeek<sup>26,27</sup>, experiments during the last two decades have started to challenge the physical interpretations of this work. Based on the Coulombic forces, it seems natural that unlike-charged macroparticles would attract each other while like-charged macroparticles would repel. However, the electrostatic interactions between biomolecules can also include counter-intuitive phenomena. In fact, there are two different coupling regimes that can be used to describe electrostatic phenomena in macromolecular solutions: a) the weak coupling regime, and b) the strong coupling regime. They are distinguished by the electrostatic coupling parameter,  $\Xi$  ( $\Xi = 2\pi z_k^3 l_B^2 \sigma_s$ , where  $l_B = e^2/4\pi\epsilon_0\epsilon_s kT$  is the Bjerrum length,  $k$  is the Boltzmann constant,  $T$  is the temperature,  $\epsilon_0$  is the vacuum permittivity,  $\epsilon_s$  is the relative dielectric permittivity,  $z_k$  is the counterion valency and  $\sigma_s$  is the surface charge density). The weak coupling regime (wcr), described by  $\Xi$  approaching 0, is where repulsive forces between the charged macromolecules characterize the system as predicted by the Coulombic interpretation. The strong coupling regime (scr), characterized by  $\Xi$  being much greater than 1, is observed when the system is influenced by strong attractive forces that could bring together two like-charged macroparticles due to the ion-ion interactions.<sup>28,29</sup> This normally happens in the presence of multivalent counterions (changing the valency of the counterions from monovalent to trivalent implies increasing  $\Xi$  by a factor 27) or in a solvent with a low dielectric permittivity (affecting  $l_b$ , which describes the solvent's ability to screen electrostatic interactions). The macromolecular surface charge can also increase the ion-ion correlation effect in these conditions as seen in the definition of  $\Xi$ .<sup>30</sup>

Nevertheless, relatively modern experimental findings revealed an even more peculiar behavior in these biomolecular mixtures, increasing the difficulty for a clear and unified

theoretical understanding. Experimental studies of Dubin, Kruif, Jacquier and co-workers have demonstrated the apparently paradoxical formation of soluble complexes in the *wcr* (where a pure repulsive Coulombic regime should be observed accordingly to the Netz's coupling theory), even when the net charges of the protein and the polyelectrolyte (or charged peptides) have the *same* sign.<sup>11,13,31-33</sup> Since the experimental conditions typically only have monovalent counterions (1:1 electrolyte solution) and the protein surface charge is not far from unity,  $\Xi \rightarrow 0$  and therefore ion-ion correlation is not expected to be a relevant contribution in this situation. This new attractive phenomenon has become known as “the complexation on the wrong side of pI”.<sup>31,33-37</sup> In this case, a positively charged polyelectrolyte forms a stable complex with a like-charged macromolecule in a solution where the pH is below the isoelectric point (pI) of this macromolecule. This defies the common sense view given by the Coulombic law (and the DVLO theory<sup>25,38,39</sup>) where like-charges should repel each other. The initial molecular interpretation of such experimental results has focused on the assumption of “charged patches” on the surface of the protein. In this interpretation, a polyelectrolyte binds to an oppositely heterogeneous charged protein region (e.g. a concentration of glutamic acids at the protein surface as seen in calcium binding sites<sup>40</sup>). Computer simulations carried out by de Vries and recently by Dzubiella and collaborators have also supported this view.<sup>11-13,41-43</sup> At first glance, this seems to be a reasonable explanation. However, the long-range nature of electrostatic interactions would require stronger charge-dipole interactions to compensate the direct charge-charge repulsion.

Another theory for this attraction of like-charged particles was analytically suggested by Kirkwood & Shumaker (KS)<sup>44</sup> based on proton fluctuations resulting from the mutual

rearrangement of the distributions of the charged groups. These rearrangements are due to local perturbations of the acid-base equilibrium due to charged moieties in the macromolecules. This is the core premise of the “charge regulation mechanism”. A practical interpretation is that the acid-base equilibrium in macromolecule A is shifted in such a way that there is an instantaneous partial charge inversion in A that starts to attract B. This shift is due to the presence of the electrical field from macromolecule B. When looking at KS's structure-sensitive electrostatic forces, there are two mechanisms that contribute to the attractive forces: Coulombic interactions and charge regulation. Equation (4.1), based on the KS theory, shows the electrostatic free energy,  $A(R)$ , in a very dilute salt regime, for the complexation between an ionizable protein and a non-ionizable polyelectrolyte at a separation distance,  $R$ , from each other.<sup>44,45</sup>

$$\beta A(R) = l_B Z_\alpha \left( \frac{\langle Z \rangle_0}{R} \right) - l_B Z_\alpha^2 \left( \frac{C}{2R^2} + \frac{\langle \mu \rangle_0^2}{6R^4} \right) \quad (4.1)$$

In Equation (4.1),  $\beta$  is equal to  $1/kT$ ,  $Z_\alpha$  is the mean valency of the polyelectrolyte chain,  $\langle Z \rangle_0$  is the average valency of the protein,  $C$  is the protein charge capacitance (or the protein charge regulation parameter) and  $\langle \mu_0 \rangle$  is the average dipole number moment at a given solution pH value. The first term on the side of Equation (4.1) is the ordinary Coulombic contribution,  $A_{\text{cou}} = \left( \frac{l_B Z_\alpha \langle Z \rangle_0}{R_p + R_{pc}} \right) / \beta$ , that disappears when the solution pH is equal to the protein's pI since  $\langle Z \rangle_0$  is equal to zero at this condition. The second term describes the two mechanisms contributing towards attractive interactions. The term with the  $1/R^4$  dependence quantifies the charge-dipole contributions,  $A_{\text{dip}} = - \frac{l_B Z_\alpha^2 \langle \mu \rangle_0^2}{6(R_p + R_{pc})^4} / \beta$ , which describes the “charged patches”

mechanism. The other attractive term containing  $C$  is the charge-induced interaction,  $A_{\text{reg}} = -\frac{l_B Z \alpha^2 C}{2(R_p + R_{pc})^2} / \beta$ , resulting from the proton fluctuations. This intrinsic physical property of an ionizable macromolecule measures its ability for charge regulation. By definition<sup>30</sup>,  $C \equiv \langle Z^2 \rangle_0 - \langle Z \rangle_0^2 \alpha - \frac{\partial Z}{\partial \text{pH}}$ . Since the charge-induced interaction has a  $1/R^2$  dependence instead of the  $1/R^4$ , it is usually the dominant contribution. Prior studies have quantified the magnitude of the charge regulation ( $A_{\text{reg}}$ ) and charge-dipole ( $A_{\text{dip}}$ ) terms at contact for different proteins (including several milk proteins, insulin, and pectin methylesterase) at pI in a model that focuses on electrostatic interactions.<sup>45</sup> For most of the protein-polyelectrolyte systems in the low salt regime, the main attractive force comes from the charge regulation mechanism. Proteins like lysozyme, which have a small dipole moment, gain their capacity to attract other charged molecules almost exclusively by this mechanism. For lysozyme, it was found that the charge regulation contribution was ca. 30 times larger than the patch term. Conversely, for proteins that have considerable dipole moments, such as albumin, the charge-dipole contribution is larger than the charge regulation term.<sup>45</sup> The total attraction can be enhanced to a greater degree by the combination of both effects that will encourage macromolecular association. Biesheuvel & Cohen Stuart<sup>46</sup>, using mean-field theory, also suggested that charge regulation is a relevant mechanism to describe protein-polyelectrolyte complexation on the wrong side of the pI.

When a polyelectrolyte approaches or even binds to a protein, its charge can induce changes in the pKa values of the nearby surface amino acids on the protein. Such pKa shifts provide valuable information, and can be measured experimentally. They can be graphically

mapped on the molecular surface revealing the existence of any preferential binding spots, if any. A lack of preferential binding spots would provide another descriptor to indicate the main importance of the charge regulation mechanism. Therefore, using visual molecular representations is a pragmatic approach to illustrate the role of the charge regulation mechanism for protein complexation. A molecular visualization of pKa shifts can be used to map all the titratable protein groups that are affected by the visit of the charged polymer chain during a simulation run.

Through the work described in this chapter, we provide a visual interpretation for information usually given by means of statistical mechanics descriptors. This interpretation would hopefully be of interest for a food chemist and can also provide a complementary picture for the physical chemistry community. We aim to show that the proton fluctuations of residual titratable groups on proteins can result in dominant *nonspecific* attractive interactions, forming a driving mesoscopic force for protein complexation. The chapter is organized as follows. In Section 4.2, we present the classical statistical mechanics approach that will be used to support and validate the molecular visualizations. Subsequently, we focus on the pKa shifts in the amino acid side chains, providing a visual representation of the interactions between the studied proteins and the polyelectrolyte to show the absence of any preferential “charged patches” on the protein surface. We complete our analysis by plotting the coordinates of the polyelectrolyte beads around the protein. This analysis is repeated at different pH values exploring repulsive and attractive complexation regimes.

## 4.2 Simulation Methods

Fully atomistic constant-pH simulations of large complexes including explicit water molecules are extremely difficult and time-consuming, even with the computing power that exists today. In such cases, coarse-grained models can be useful in resolving slow convergence issues by eliminating unnecessary atomistic details and allowing the repetition of the calculations under several different experimental conditions (varying pH, salt, mutations, etc.). Such simplified computer models can be well applied on macromolecular systems that involve more than one titrating object and contain multiple ionizable sites.<sup>21,47</sup> This allows us to achieve greater computational efficiency while still calculating accurate characteristics, such as pH effects and other physical and biological parameters. Such simplified models have been very successful in describing biomolecular phenomena in general, and made possible to reach the desired sampling properties to probe protein-polysaccharide complexation in constant-pH computer simulations.<sup>21</sup>

The cell model used in this study is the same coarse-grained (CG) model used before by Barroso da Silva et al.<sup>45</sup> This model offers the appropriate condition to explore the protein complexation problem with a focus on electrostatic interactions. Semi-grand canonical ensemble Monte Carlo (MC) simulations are used to solve this CG constant-pH model, consisting of the charged species being confined in an electroneutral spherical cell. The simulation cell contains one single protein molecule at the center (or a protein and a polyelectrolyte), along with scattered mobile electrolytes (counterions and added salt). The macromolecule modeled without internal details (i.e. bond lengths, angles, and dihedral angles are fixed) is set at the center of the simulation cell as shown in Figure 4.1a). The radius of the

cell,  $R_{\text{cell}}$ , is determined by the protein concentration. A further advantage is that all electrostatic interactions are fully taken into account in this model without the need for any truncation or additional possible artifacts. Each ion  $k$  is treated explicitly as a charged hard sphere particle with radius  $R_k$  ( $=2.125\text{\AA}$ ) and valency  $z_k$ . This corresponds to the so-called “restricted primitive model” in the classical fluids literature<sup>48,49</sup> for modeling electrolyte solutions. Both the ions and the polymer monomers (see Figure 4.1b)) are free to move inside the simulation box. The solvent is simulated as a structureless dielectric medium and is allocated the same relative dielectric permittivity,  $\epsilon_s$ , as the mobile ions, protein, and polyelectrolyte. We used here  $\epsilon_s = 78.7$  for  $T = 298\text{ K}$ .

The minimum cutoff distance for the interaction potential energy between two particles or sites,  $i$  and  $j$ , is the sum of their radii ( $R_i + R_j$ ), following the hard-sphere model. This prevents the Coulombic collapse ( $r_{ij} \rightarrow 0$ ) and allows us to define particle sizes. If the separation distance ( $r_{ij}$ ) between sites  $i$  and  $j$  is greater than the cutoff distance, the interaction energy is

$$u(r_{ij}) = \frac{q_i q_j}{4\pi\epsilon_0\epsilon_s r_{ij}} \quad (4.2)$$

where  $\epsilon_0$  is the vacuum permittivity and  $q_i = z_i e$  and  $q_j = z_j e$  are the charges on particles  $i$  and  $j$ , respectively ( $e$  is the elementary charge). No van der Waals interaction term is included in the model in order to focus on electrostatic effects. Any observed attraction in the system is a result of the multipolar interactions and the charge regulation mechanism, as discussed above for the KS equation which provides a theoretical validation for our simulations results.

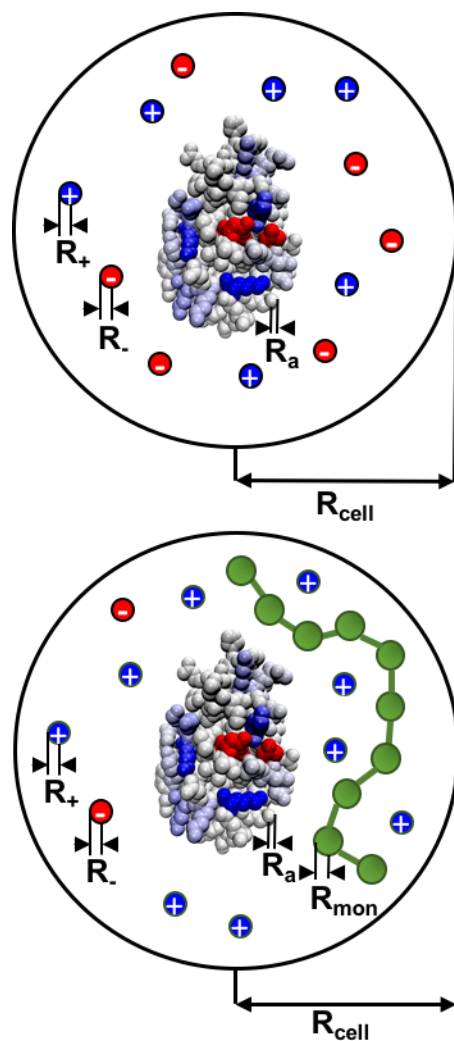


**Figure 3.1:** Schematic representation of the model system in explicit salt. a) *Top:* System with no polyelectrolyte. Protein is surrounded by counterions and added salt particles. b) *Bottom:* A polyanion, consisting of 21 negatively charged monomers, is also present with the protein system. Simulations with both models were carried out at different pH regimes<sup>45</sup>.

### 4.2.1 Protein model

Two different whey proteins,  $\alpha$ -lactalbumin ( $\alpha$ -LA) and lysozyme (LYZ), are studied here.  $\alpha$ -LA is a milk protein found in most mammalian species and is responsible for the production of lactose in the mammary gland, while LYZ is an active enzyme found in several bodily fluids such as human milk, tears, and mucus. Apart from their biological importance and practical applications in many food products<sup>6,24</sup>, these proteins are quite appealing from a physicochemical point of view. Both proteins are similar in size and radii; however,  $\alpha$ -LA has a higher dipole moment (at pI,  $\mu_{\text{LYZ}} = 24$  and  $\mu_{\alpha\text{-LA}} = 82$ <sup>50</sup>) and larger capacitance in comparison with LYZ. Previous studies have already indicated that the complexation properties of LYZ are directly related to its charge regulation parameter.<sup>45,50</sup> On the other hand,  $\alpha$ -LA has a reasonably large dipole moment that can well contribute to its binding capabilities.<sup>41</sup>

The proteins were modeled as rigid bodies in full atomistic detail according to the X-ray structures provided by the Protein Data Bank (PDB identities are 1HFY and 2LZT for  $\alpha$ -LA and LYZ, respectively). The PDB files were used without any manipulation as in previous studies.<sup>45,50,51</sup> Only the records for atoms and their corresponding coordinates were used as input. The PDB id 1HFY is from the goat organism (*Capra hircus*). Ideally, for food applications, the bovine  $\alpha$ -LA (PDB id 1F6S) would be a better choice. However, for the sake of comparison with the calculations done before by de Vries, we have chosen to use the same coordinates used in his work (PDB id 1HFY).<sup>48</sup> Despite having the same number of amino

acids, there are slight differences in the main physical chemical properties of the proteins; for example, the bovine  $\alpha$ -LA has a larger C and  $\mu$ .<sup>50</sup>

Each protein atom available in the PDB file is assigned a radius of 2.0 Å. Partial charges are defined and allowed to vary during the simulation run according to the solution pH and the acid-base equilibrium. A proton titration scheme with explicit ions<sup>52-54</sup> is followed. The central idea behind such a titration protocol is to transform the ionization process into a MC movement, where the acceptance or rejection of an attempt to change the protonation state of a given residue is based on a trial energy:

$$\Delta U_{\text{titra}} = \Delta U_c \mp kT \ln 10 (\text{pH} - \text{pK}_0) \quad (4.3)$$

In Equation (4.3),  $\Delta U_c$  is the corresponding change in Coulomb energy, and  $\text{pK}_0$  is the dissociation constant of the model compound (i.e. the isolated amino acids). These values are given in Table 4.1 and are taken from the experimental work of Nozaki & Tanford.<sup>55</sup> The reader is referred to refs. 45,50,51 for more details on this method. We note that this titration model allows us to include the most relevant details of the chemical heterogeneity of the proteins in our calculations. The inclusion of the details of the  $[\text{OH}^-]$  and  $[\text{H}^+]$  association and dissociation equilibria is crucial to fully incorporate the charge fluctuations in the computer simulations.

**Table 3.1:** Titrating residues in the proteins studied. The dissociation constants ( $pK_0$ ) for the isolated amino acids are given in the second row followed by the number of occurrences of each ionizable amino acid in both proteins. The data was taken from the experimental work of Nozaki & Tanford.<sup>55</sup>

Protein	Residues	ASP	GLU	HIS	TYR	LYS	CYS <sup>(a)</sup>	ARG
$pK_0$		4.0	4.4	6.3	9.6	10.4	10.8	12.0
<b>LYZ (2LZT)</b>	129	7	2	1	3	6	0	11
<b><math>\alpha</math>-LA (1HFY)</b>	123	14	4	3	4	13	0	1

<sup>(a)</sup> Only cysteine residues not engaged in sulfide bridges can titrate.

#### 4.2.2 Polyanion model

The polyelectrolyte used in these simulations is the same flexible chain model used in Barroso da Silva et al.<sup>50</sup> It is intended to mimic pectin, and consists of 21 units of negatively charged monomers connected by harmonic springs. The monomer units have a radius  $R_{\text{mon}}=2$  Å and a fixed valency  $z_{\text{mon}}=-1$ , indicating its non-titratable nature. Considering the typical low  $pK_a$  for pectin ( $pK_a \approx 2.9$ <sup>56</sup>), this is a reasonable assumption for most of the studied pH values. Furthermore, this is convenient to separate the charge regulation contributions from the different macromolecules, enabling us to focus on the protein. If the polymer beads were allowed to titrate, the attractive term of Eq. (4.1) will be enhanced. The polyelectrolyte is flexible and free to move within the cell, interacting the protein and all monovalent free ions (see Figure 4.1b). The bond interaction potential between neighboring monomer units can be calculated using Equation (4.4).

$$\beta u^{bond} = \frac{l_B}{2r_{min}^3} \sum_{i=1}^{N_{mon}-1} (r_{i,i+1})^2 \quad (4.4)$$

where  $r_{i,i+1}$  is the distance between monomer  $i$  and monomer  $i+1$  and  $r_{min}$  is the separation distance corresponding to the minimum energy for a dimer, calculated to be around 4 Å. The potential in Equation (4.4) is balanced by electrostatic repulsion, also calculated between bonded beads, resulting in a reasonable separation between the beads. The total energy for the system at a given configuration is

$$U = \sum_{i=1}^{N_{mob}} v^{ex}(r_i) + \frac{1}{2} \sum_{i=1}^N \sum_{j=1}^N u(r_{ij}) + u^{bond} \quad (4.5)$$

where  $N_{mob}$  is equal to the total number of mobile particles, which includes counterions, added salt ions, and polyanion beads but does not include the protein atoms.  $N$  is equal to the total number of particles in the system, *including* the protein atoms.  $v^{ex}(r_i)$  is the cell constraint potential, which is equal to zero when the  $i^{th}$  molecule is within the radius of the spherical simulation cell and equal to infinity otherwise, as shown in Equation (4.6).

$$v^{ex}(r_i) = \begin{cases} 0 & r_i \leq R_{cell} \\ \infty & otherwise \end{cases} \quad (4.6)$$

### 4.2.3 System details

We carried out several different sets of simulations:

- Set A - A single protein immersed in an aqueous electrolyte solution (see Fig. 1a). These simulations were used to quantify the main physical chemical properties of each protein ( $Z$ ,  $\mu$  and  $C$ ) and pKa's for all the titratable groups.
- Set B - A single protein together with a polyelectrolyte chain immersed in an aqueous electrolyte solution (see Fig. 1b). In these simulations, the distance between the centers of mass of the polyelectrolyte and the protein was biased to provide the computed free energy of interaction. To efficiently sample the conformational space of the system, we followed the penalty function protocol as done previously.<sup>45</sup> The bin size of the histograms used to calculate the potential of mean force [ $w(R)$ ] from the measured radial distribution function is 1 Å. For LYZ at pI, we repeated previous calculations<sup>45</sup> exploring all four possible charges for a neutral macromolecule: *i*) a “fully neutral” protein with all atoms having a null charge (multipolar contributions are also removed), *ii*) a protein with fixed charges at each amino acid residue obtained from a previous titration run (dipole and high order moments are kept constant), *iii*) a protein with an ideal dipole at its center of mass taken from the fixed charge model (high order moments are removed), and *iv*) a protein with charge fluctuations as provided by the titration scheme (all electrostatic contributions are present). These models will be referred as *i*) “neutral”, *ii*) “non-titrating”, *iii*) “dipole” and *iv*) “titrating”. They allow specific electrostatic interactions to be disabled,<sup>45</sup> permitting us to compute individual contributions to the total free energy
- Set C - A single protein together with a polyelectrolyte chain immersed in an aqueous electrolyte solution (see Fig. 1b). These simulations measured the pKa's in

the presence of the charged polymer chain. They provide information for the visualization of the pKa shifts. Since it is an unbiased sampling simulation, the outcomes can be directly used without any need for additional correction to remove artifacts introduced by the use of the radial penalty function. In order to make a clear difference between the pKa's obtained in the presence or in the absence of the polyelectrolyte in the simulation cell, we shall refer to them, respectively as  $pK_{aPPol}$  and  $pK_{aP}$ .

All constant-pH MC simulations were performed in a low salt regime (1:1 electrolyte solution). The salt concentration was fixed at 1.2 mM, while the protein concentration was set to 58.7  $\mu$ M. Neutralizing counterions were added in all systems, and the solution pH was varied from 2 to 13. All studied proteins were in the monomer state. At least  $10^9$  MC steps were necessary for equilibration and production runs depending on the solution pH. For set B, a pre-equilibration phase with  $10^8$  MC steps was carried out to give the initial approximate  $w(r)$  for the penalty function protocol<sup>50</sup>.

From the runs for sets A and C, we determined  $pK_{aP}$  and  $pK_{aPPol}$  by analyzing the simulation data. The MC simulations provide the average charge number for all amino acid side chains at a given pH solution. The determination of the pKa's is based on such charges. The criterion is to monitor the pH values and identify the pH where the absolute charge was equal to 0.5. When this condition is observed, pKa can be identified as equal to pH. This approach has been used in previous titration studies.<sup>21</sup> The same criterion was followed for the single protein case (set A) and the protein + polyelectrolyte case (set B). Results were compared among themselves as well as with the ideal  $pK_0$  values of amino acid side chains.

Upon visualizing the differences between  $pK_{aP}$  and  $pK_{aPPol}$  values on the protein, we were able to visually identify the areas of the protein that undergo a change in  $pK_a$ , signaling protein surface groups that are more perturbed by the presence of the charged polymer chain. These areas can be easily spotted on the protein surface maps to provide a visual and practical representation of the interactions between the protein and the polyanion. Complementary visual analyses are done by plotting the polyelectrolyte beads location around the proteins at different pH conditions from saved configurations. These snapshots are recorded after each  $10^3$  MC steps during the production runs of the set C.

## 4.3 Results and Discussion

### 4.3.1 Main physical chemistry parameters

We shall start our discussion with the main physicochemical properties of the proteins such as the net charge number ( $Z$ ), charge capacitance ( $C$ ) and dipole moment number ( $\mu$ ) that are used in Equation (4.1) to predict the free energy of interactions using the KS theory. These physical quantities for LYZ were computed in the MC simulations for set A under low salt conditions. The simulations were conducted for three selected solution pH values and are listed in Table 2. Using them as input variables in Eqn. (1) lets us quantify the theoretical contributions from the direct Coulombic term as well the charge regulation and charge-dipole (patch) terms in the three regimes: a) attractive, when the protein and the polyelectrolyte chain have charges of opposite signs (pH 7); b) neutral, when the protein is at pI (pH 10.9), and c) repulsive, when both biomolecules have charges of the same sign (pH 13). From this KS theory analytical analysis, it can be seen that the charge regulation mechanism ( $A_{reg}$ ) contributes to

enhance attraction in all regimes. The patch term ( $A_{\text{patch}}$ ) helps but contributes a quite modest additional attraction (ca. -0.2 kT). The ratio  $A_{\text{reg}}/A_{\text{patch}}$  varies from 7.5 to 60.7 depending on the solution pH, indicating that the charge regulation mechanism, not the “patch” contribution, is the main factor in the complexation. This is in perfect agreement with what was observed before at pI.<sup>50</sup>

**Table 3.2:** Computed protein net charge number ( $Z$ ), charge capacitance ( $C$ ) and dipole moment number ( $\mu$ ) for LYZ at different pH regimes. These data were obtained from the MC runs with set A. The Coulombic, charge regulation and patch contributions were analytically calculated in kT units using the equations for  $A_{\text{cou}}$ ,  $A_{\text{reg}}$ , and  $A_{\text{dip}}$ , respectively. The total contribution was obtained by adding these three terms. The ratio Regulation/Patch was given by  $A_{\text{reg}}/A_{\text{dip}}$ . Radii for LYZ and the polyelectrolyte were estimated as 28 and 30 Å, respectively.<sup>50</sup>

pH	Z	C	$\mu$	Coulombic	Charge Regulation	Patch	Total	Regulation /Patch
7.0	7.5	0.5	26.0	-19.3	-1.7	-0.2	-21.2	7.5
10.9	0.0	1.6	24.0	0.0	-5.3	-0.2	-5.5	28.0
13.0	-11.4	1.3	14.7	29.3	-4.3	-0.1	24.9	60.7

#### 4.3.2 Free energy of interactions

A numerically more rigorous partitioning of contributions to the potential of mean force can be achieved by means of simulations with the different four charge models cited above (Set B). The pI condition is ideal for such theoretical scrutiny for multiple reasons. It offers the possibility to explore different manners to distribute partial charges that give the same neutral system. At the same time, it is also the only situation where the definition of the dipole moment

is well defined in terms of the reference. Figure 4.2 shows the results for LYZ at pI with the same simulation parameters and details as in Barroso da Silva et al.<sup>45</sup> The presence of a minimum in  $w(r)$  indicates the formation of a stable protein-polyelectrolyte complex. As would be expected, a simple “neutral” macromolecule model, which essentially only describes the molecular shape of the protein, cannot attract a charged polymer. If our model included contributions from van der Waals forces this would result in a weak attraction, but our goal in this work is focus only on the electrostatic interactions. Enabling the dipole contributions (“dipole” curve) and even the higher order multipolar interactions (“non-titrating” curve) does not produce an attraction strong enough to lead to complexation. The difference between “dipole” and “non-titrating” is minimal, showing that the contribution of higher order electrostatic moments is very small for this protein system. The results from these simulations confirm that the charge-dipole and higher multipolar interactions give a very small attractive contribution to the total free energy in this case, as anticipated by the KS analysis. The only model showing complexation is the one where the charge can fluctuate as a function of pH (“titrating” curve). This result is not only important to understand the behavior of lysozyme for protein complexation, but it also indicates that, without constant-pH simulations, the fundamental physical mechanisms leading to complexation are not properly described. Simply assigning partial charges for a given pH and keeping them constant during the simulation run (as often done even in more sophisticated simulations) is equivalent to our “non-titrating” case. For  $\alpha$ -LA, the picture is a bit more complex, since this protein has a larger dipole moment that will play a key role as well. Previous computational studies with the same charged models<sup>45</sup> report that the “titrating” and “dipole” cases give virtually the same result for  $\alpha$ -LA at pI. In

fact, it is also observed that high order moments (charge-quadrupole interactions and so on) can add repulsive contributions to the interaction. The results for the fixed charge model (“non-titrating” case) in previous studies show a minimum for  $w(r)$  at an intermediate depth between the “titrating” and “neutral” cases.

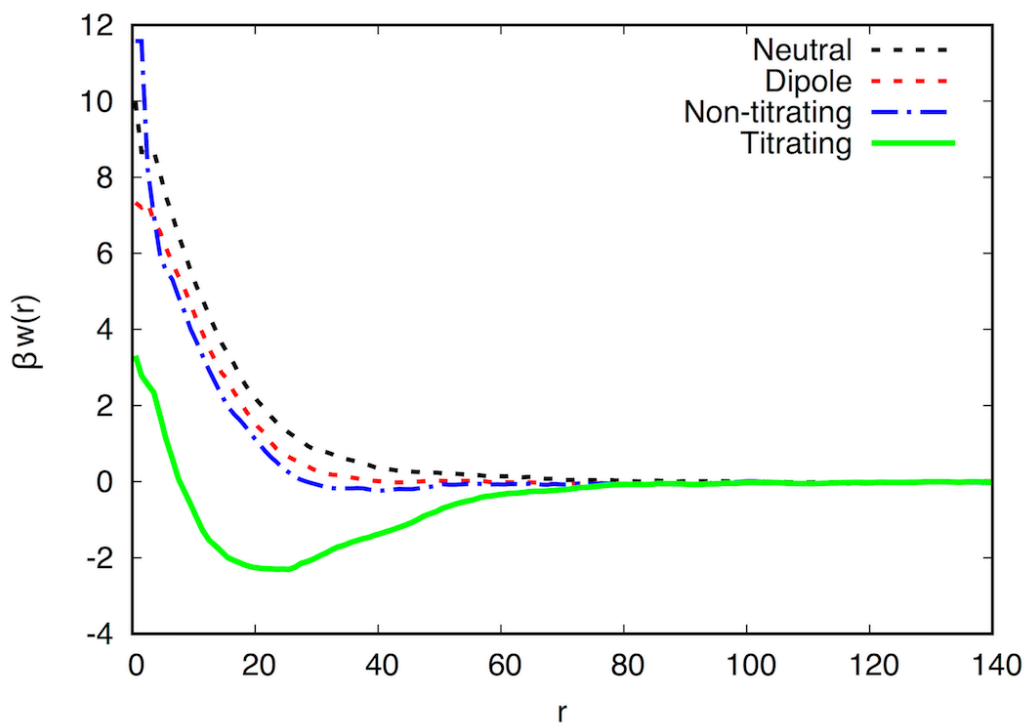


**Figure 3.2:** Computed potentials of mean force between the centers of mass of lysozyme and the polyelectrolyte chain. Data are from the MC runs with set B at pI assuming different charge models. Simulation parameters and details are chosen as in Barroso da Silva et al.<sup>45</sup> pH regimes where a negative minimum for  $\beta w(r)$  is observed are shown with solid lines while repulsive cases are shown with dashed lines for all three panels.

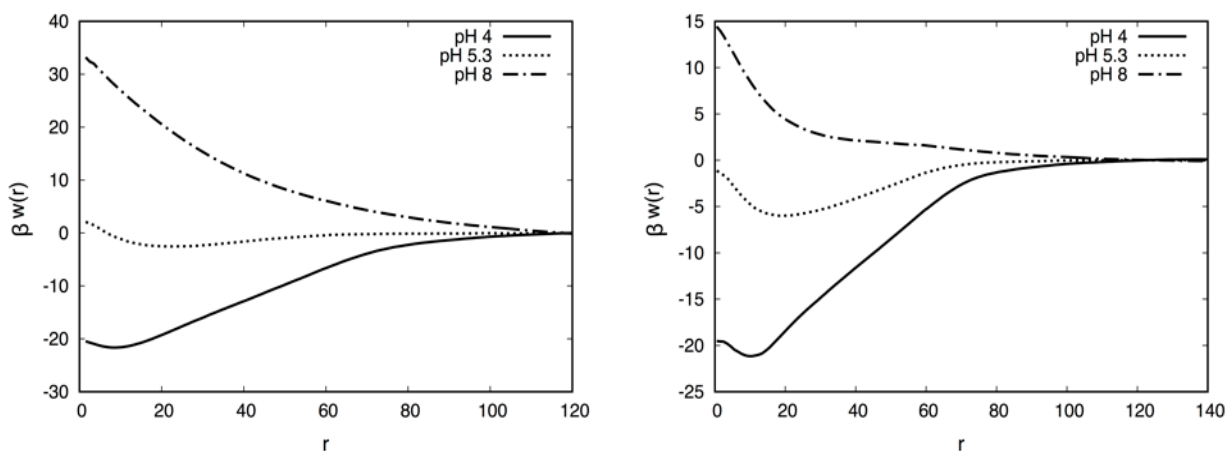


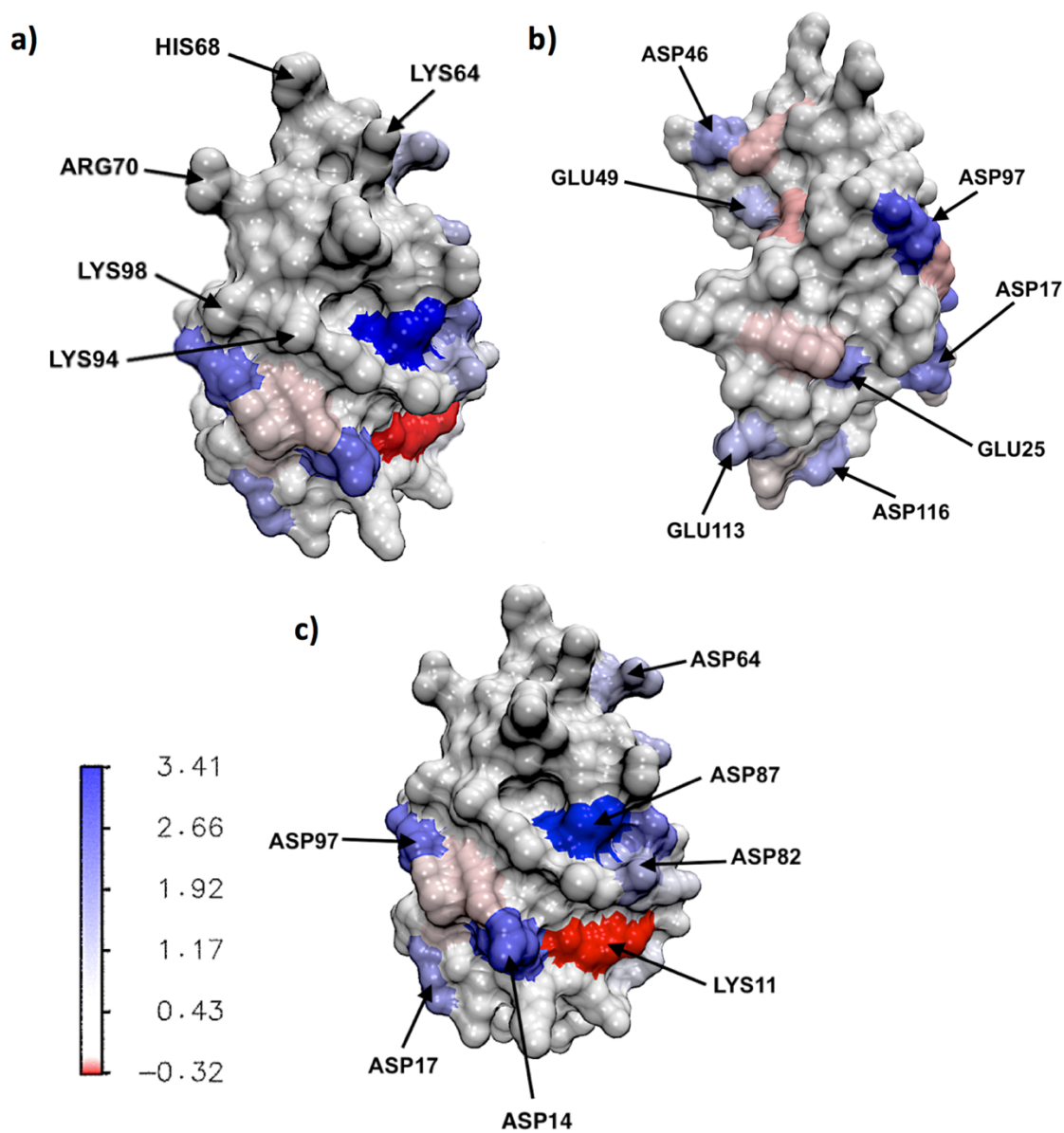
**Figure 3.3:** Computed potentials of mean force between the centers of mass of the proteins and the polyelectrolyte chain. **a)** Data for LYZ at solution pH equal to 7.0, 10.9 (pI) and 13.0. **b)** Data for  $\alpha$ -LA at solution pH equals to 4.0, 5.3 (pI) and 8.0. pH regimes where a negative minimum for  $\beta w(r)$  is observed are shown with solid lines while repulsive cases are shown with dashed lines for all three panels.

We next examined the pH effects on the free energy curves. Figures 4.3a) and 4.3b) show the  $w(r)$  profiles for lysozyme and  $\alpha$ -lactalbumin at the three different pH regimes studied. While LYZ is well-known as a protein whose complexation properties come solely from the charge regulation mechanism,<sup>50</sup>  $\alpha$ -LA is similar in size and has been used before as a proof to support the patch-theory arguments.<sup>43</sup> Below the pI, both proteins are positively charged and strongly interact with the polyanion. This is a predominant direct Coulombic interaction. At pH 7, LYS has +7.5 units of charge, while, at pH 4,  $\alpha$ -LA has +3.9 units of charge. The intermolecular interaction with a negatively charged polymer chain ( $Z_\alpha = -21$ ) is strongly attractive. The purpose of selecting these two pH values is also to show how the other

electrostatic terms contribute to enhance the attraction even in the direct Coulombic attractive regime. Despite the differences in  $Z$  ( $Z_{\text{LYZ}}=+7.5$  and  $Z_{\alpha\text{-LA}}=+3.9$ ), the minimum for  $w(r)$  observed for both proteins is similar. This happens because, although  $\alpha$ -LA has the smaller charge in this comparison, it has a higher  $C$  (1.6) and  $\mu$  (64) at pH 4. Therefore, the combination of such interactions results in an attractive behavior similar to a highly charged molecular case. Both proteins exhibit attraction at pI in agreement with the KS predictions. At the repulsive regime (pH equals to 8 and 13, respectively, for  $\alpha$ -LA and LYZ), the higher pH values found in basic solutions force the deprotonation of amino acids in the proteins, leading to a more negatively charged protein. Since the polyelectrolyte is also negatively charged, this results in a stronger repulsion between the two macromolecules.

#### *4.3.3 pKa shifts due to the interactions with the polyelectrolyte*

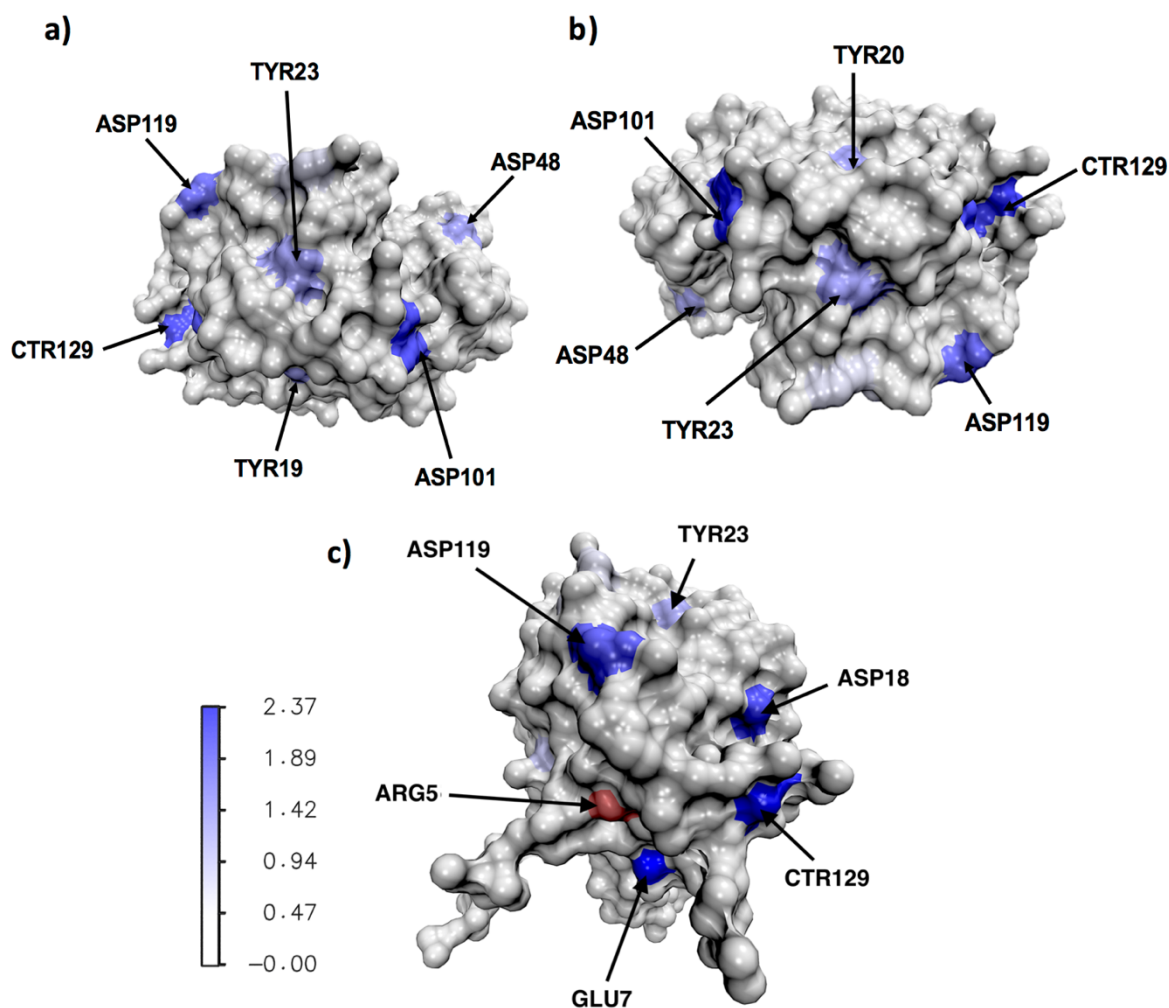
The results discussed so far do not indicate yet if the complexation is specific or nonspecific, *i.e.* if the polymer chain preferentially binds to a specific oppositely charged patch on the protein or visits multiple surface amino acids. For  $\alpha$ -LA, de Vries suggested a positively charged patch involving amino acid residues, LYS.62.NZ (K62), LYS.94.NZ (K94), LYS.98.NZ K(98), ARG.70.NH1 (R70), and HIS.68.ND1 (H68) as specific for the complexation with a polyanion.<sup>43</sup> Conversely, in another computational study,<sup>50</sup> single or multiple mutations of these basic amino acids did not prevent the complexation if the charge fluctuation mechanism was included in the model. The analysis of the pKa shifts ( $\Delta pK_a = pK_{a\text{ppol}} - pK_{a\text{p}}$ ) can clarify this scenario by revealing which protein titratable groups are more often close to the charged polymer chain.



**Figure 3.4:** Snapshots of the  $\alpha$ -LA protein showing the difference in pKa values between the protein in the presence of the polyanion and for the isolated protein simulations. The amino acid side chains undergoing a change in pKa are labeled. Blue indicates a positive shift in pKa, while red indicates a negative shift in pKa. Shifts are calculated as  $\Delta pK_a = pK_{a_{ppol}} - pK_{a_p}$ . a), b), and c) shows the  $\alpha$ -LA from different angles and viewpoints to provide a complete picture of the shifts observed.

Figure 4.4 shows the shifts in pKa occurring for different amino acid residues on the  $\Delta$ -LA due to the presence of a polyanion. A positive change in pKa ( $\Delta pK_a = pK_{a,PPoI} - pK_{a,P}$ ), highlighted in blue, indicates that the pKa for the amino acids in the solution with the polyelectrolyte is higher than for the isolated protein case. This indicates that those amino acids, when exposed to the polyelectrolyte, are more likely to be protonated even at higher pH values, resulting in an increase in the pKa value. A negative pKa change ( $\Delta pK_a = pK_{a,PPoI} - pK_{a,P} < 0$ ), highlighted in red, indicates a lower likelihood of the amino acids exposed to the polyelectrolyte to protonate. Figure 4.4a) specifically compares a group of amino acids that constitute a “charged patch” in de Vries et al.<sup>43</sup> No pKa shifts are observed in any of these labeled amino acid residues. The two amino acid groups that experience observable positive pKa changes are aspartic acid (ASP) and glutamic acid (GLU). For the case of the isolated protein in an electrolyte solution, the pKa values for ASP and GLU were found to be around 2-3 and 4 pH units, respectively (see Table A4.1), indicating that they are negatively charged and deprotonated above pI. Therefore, when exposed to a negatively charged polyelectrolyte, their pK’as shift to a larger value, allow them to function as proton donors. In general, the amino acid side chains seem to result in a positive change in pKa, indicating that it is easier for them to accept a proton with a polyelectrolyte present leading to a more positive charge. On the other hand, the lysine (LYS) in the isolated protein (without the polyanion) has a high pKa value of 11-13 pH units, indicating that it is likely positively charged and in its protonated form. However, due to the presence of a polyanion, it deprotonates and experiences a negative shift in pKa.

It can also be observed that the pKa changes for ASP and GLU are occurring *all* over the protein surface, and not just in one specific area, confirming that there is not just one preferential “hot spot”, as suggested by the “charged patch” hypothesis.<sup>43</sup> The magnitude of the change in pKa of amino acid residues is correlated with the frequency the corresponding region was visited by the polyelectrolyte, since each interaction would result in a further rise or drop in the pKa of the amino acids in that region. Since ASP and LYS exhibit the largest changes in pKa, it can be inferred that the polyanion interacted most frequently with the regions surrounding them. This is probably due to the fact that ASP in the isolated protein was found to have the lowest pKa<sub>p</sub> (ranging from 0-3 pH units) while LYS was found to have the highest pKa<sub>p</sub> (ranging from 11-13 pH units), with respect to the other amino acid side chains. Therefore, it is expected that ASP and LYS would undergo the largest change in pKa when interacting with the polyelectrolyte at closer separation distances.



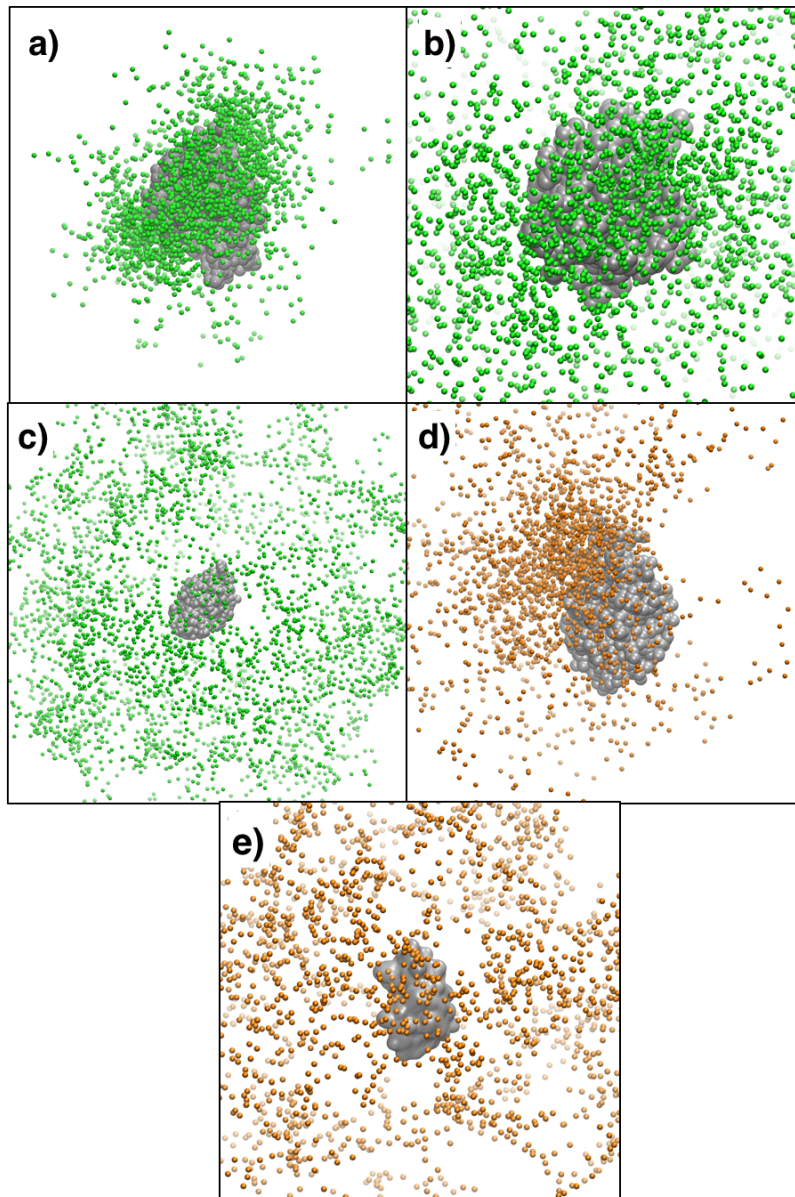
**Figure 3.5:** Mapping the pKa shifts for the LYS protein showing the difference in pKa values between the protein in the presence of the polyanion and for the isolated protein simulations. The amino acid side chains undergoing a change in pKa are labeled. Blue indicates a positive shift in pKa, while red indicates a negative shift in pKa. Shifts are calculated as  $\Delta pK_a = pK_{a,PP01^-} - pK_{a,p}$ . a), b), and c) shows the lysozyme from different angles and viewpoints to provide a complete picture of the shifts observed.

Figure 4.5 shows the pKa shifts observed for the amino acid side chains in the lysozyme due to the protein-polyelectrolyte interactions. Most of the amino acid residues exhibit an increase in pKa, with the most significant changes occurring in aspartic acid (ASP), glutamic acid (GLU), and tyrosine (TYR). The pKa<sub>p</sub> values for ASP, GLU, and TYR in the isolated protein are in the ranges of pKa<sub>p</sub> 1-3, pKa<sub>p</sub> 2-3, and pKa<sub>p</sub> 8-10 (see Table A4.2), respectively. Because the pKa<sub>p</sub> values for ASP and GLU were much lower than the TYR, it is easier for them to protonate, leading to larger pKa changes than the TYR. This is indicated by the darker shade of blue for the ASP and GLU amino acids. It should be noted that Arginine (ARG) actually undergoes a very slight negative pKa change of -0.0049, rounded to 0.00 on the color scale bar, and can be visualized as the red area on the protein surface. This is the only amino acid residue that undergoes a negative pKa change indicating that it deprotonates in the presence of the polyanion.

It can also be observed that, overall, the  $\alpha$ -LA undergoes larger shifts in pKa values than the lysozyme. The largest pKa change for the  $\alpha$ -LA was 3.4 while the largest pKa change for the LYZ was 2.4. This is because the  $\alpha$ -LA has a much larger dipole moment than the lysozyme, resulting in a larger attraction and, consequently, larger shifts in pKa as the polyanion is more often close to the protein. This is in agreement with the stronger affinity observed between  $\alpha$ -LA and the polyanion, when compared to the interaction between LYS and the same polyelectrolyte chain.<sup>45</sup> Even though LYZ has a much smaller dipole moment, no preference for a “hot spot” is observed in this case either. pKa shifts occur all over the surface of the LYZ, indicating that the polyanion is interacting with multiple areas on the protein, instead of a single specific area or “patch”. This visualization of the interaction clearly

supports the theory that charge regulation mechanism, and not “charged patches”, are the driving force for protein-polyelectrolyte complexation in this low salt regime regardless of the dipole moment or capacitance of a protein.

In order to verify the pKa shifts on the proteins are occurring due to their interaction with the polyelectrolyte, we mapped the varying coordinates of the polyelectrolyte onto a single frame to allow us to see the trajectory of the polyelectrolyte (Figure 4.6). This visualization was conducted for the LYS at three different pH levels and for the  $\alpha$ -LA at two different pH levels. The data for the lysozyme in the attractive regime, at pI, and in the repulsive regime is shown in Figures 4.6a)-c), which confirms that there is no preferential hot spot on the protein that attracts the polyelectrolyte. Figures 4.6d) and 4.6e) show the visualizations for the  $\alpha$ -LA at pI and in the repulsive regime. At pI (see Figure 4.6d)), there appears to be a slight preference in the top left section, which is the same region that de Vries et al.<sup>48</sup> deemed as a “charged patch”. This is due to the larger dipole moment for  $\alpha$ -LA which enhances the  $A_{\text{dip}}$  term in Equation (4.1). However, we observe that even with the slight preference, the polyelectrolyte is still interacting with several different areas on the protein and not just one patch. Figure 4.6e) further shows that any preferential spots the polyelectrolyte might interact with at pI disappears in the repulsive regime. For both proteins, as the pH level increases, the distance between the polyelectrolyte beads and the proteins also increases, again confirming the stronger repulsion and weaker binding at higher pH levels shown earlier in Figure 4.3.



**Figure 3.6:** A visualization of the changing coordinates of the polyelectrolyte with the proteins mapped into a single frame, allowing us to see all the points visited by the polyelectrolyte. The green polyanion beads indicate interactions with the lysozyme while the orange polyanion beads describe the interaction with the  $\alpha$ -lactalbumin. The trajectories were visualized at the following pH regimes: a) 7.0 (LYS, attractive) b) 10.9 (LYS, pI) c) 13.0 (LYS, repulsive) d) 5.3 ( $\alpha$ -LA, pI) e) 8.0 ( $\alpha$ -LA, repulsive)

#### 4.3.4 Accuracy of the pKa shifts

Computed pKa predictions are often compared with experimental measurements as well with other available theoretical methods in order to assess their accuracy.<sup>21</sup> Lysozyme is one of the most popular proteins in such studies due to its large number of titratable amino acids. Table 4.3 shows the comparison between the experimental pKa<sub>p</sub> values<sup>57</sup> for certain amino acids in the isolated lysozyme and the pKa<sub>p</sub> values calculated by our MC simulations with explicit ions. Typical numerical descriptors used in benchmark pKa studies, such as the maximum absolute error (MAX), the averaged absolute error (AAE) and the root-mean-square error (RMSE), are calculated and reported in this table too. Data from other common theoretical methods with different degrees of granularity are listed together. In comparison with the experimental data (measured at a slightly higher salt concentration), our calculated pKa values have the MAX, AAE and RMSE values of 3.3, 1.2 and 1.5 pH units, respectively. These numbers are within the range of values given by different theoretical models for lysozyme (MAX=[1.4-2.8], AAE=[0.5-1.4] and RMSE=[0.8-1.6]) and also for larger sets of protein systems (MAX=[0.5-4.3], AAE=[0.4-1.5] and RMSE=[0.2-1.5]).<sup>21</sup> Our results for amino acids such as GLU7 and ASP18 show quite good agreement with experimental data, but others such as GLU35 show a poor approximation. This is probably due to the location of GLU35, which is buried deeply inside the protein structure. Since all interactions implicitly included in measuring the pKa assume the same environment in both cases, buried sites are not accurately described leading to large deviations from experimental values. This is observed for most of the theoretical methods as seen in Table 4.3.

**Table 3.3:** Calculated and Experimental pKa values of lysozyme. <sup>(a)</sup> Data taken from Chen et al.<sup>57</sup> at 50mM of salt. <sup>(b)</sup> Data taken from Barroso da Silva et al.<sup>21</sup>

<b>Amino Acid</b>	<b>Experimental (a)</b>	<b>Present work</b>	<b>GB (a)</b>	<b>All-atom REX- CpHMD (a)</b>	<b>PropKa (b)</b>	<b>FPTS (b)</b>	<b>NULL (b)</b>
<b>GLU 7</b>	2.6(2)	2.5	2.6(1)	3.5(1)	4.0	3.3	4.4
<b>HIS 15</b>	5.5(2)	6.3	5.3(5)	5.1(0)	6.7	5.6	6.3
<b>ASP 18</b>	2.8(3)	2.2	2.9(0)	2.9(4)	3.4	2.8	4.0
<b>GLU 35</b>	6.1(4)	2.8	4.4(2)	8.6(1)	6.5	3.5	4.4
<b>ASP 48</b>	1.4(2)	2.5	2.8(2)	0.6(6)	1.8	3.4	4.0
<b>ASP 52</b>	3.6(3)	2.6	4.6(0)	5.5(1)	3.8	3.3	4.0
<b>ASP 66</b>	1.2(2)	1.9	1.2(4)	0.3(7)	1.9	3.0	4.0
<b>ASP 87</b>	2.2(1)	1.9	2.0(1)	1.5(7)	3.3	3.2	4.0
<b>ASP 101</b>	4.5(1)	1.9	3.3(3)	5.9(2)	3.9	2.9	4.0
<b>ASP 119</b>	3.5(3)	2.3	2.5(1)	3.2(1)	3.6	3.2	4.0
<b>MAX</b>		3.3	1.7	2.5	1.4	2.6	2.8
<b>AAE</b>		1.2	0.5	1.0	0.7	1.0	1.4
<b>RMSE</b>		1.5	0.9	1.2	0.8	1.4	1.6

## 4.4 Conclusion

Through various Monte Carlo simulations focusing mainly on electrostatic interactions, along with both quantitative and visual analyses, we show the significance of the charge regulation mechanism in protein-polyelectrolyte complexation for two different proteins,  $\alpha$ -lactalbumin and lysozyme. Both proteins are similarly sized milk proteins with different dipole moments and capacitance values. We conducted simulations for the proteins at varying pH levels, both in the presence of a polyelectrolyte and without it. By studying the main physicochemical parameters, we observe the ratio of  $A_{reg}/A_{dip}$  to be always positive over the range of pHs studied, indicating that the charge regulation mechanism is stronger than the

“patch” contributions from the ion-dipole interactions. The potential of mean force (PMF) analysis provides further proof that the only way to achieve complexation is to allow for the fluctuation of charges. Visualizations of the amino acid pKa shifts on both protein surfaces provide us with an indirect measure of protein-polyelectrolyte interactions and show no preferential hot spots on either surface. This shows, in an easy-to-comprehend manner, that charge regulation is the dominant factor in protein complexations, regardless of the dipole moment or capacitance of the protein. In order to confirm the visualized *pKa* shifts are a result of the interactions between the polyelectrolyte and the proteins, we also mapped the various coordinates of the polyanion beads throughout the simulation in order to show exactly where the polyelectrolyte interacts with the protein surface. These measures of analysis help provide a complete picture supporting our hypothesis that charge regulation, and not charged “patches”, is the more important mechanism in protein-polyelectrolyte complexation.

## **4.5 Acknowledgment**

This work has been supported in part by the Fundação de Amparo à Pesquisa do Estado de São Paulo [Fapesp 2015/16116-3 (FLBDS)] and the University Global Partnership Network (UGPN). FLBDS also thanks the support of the University of São Paulo through the NAP-CatSinQ (Research Core in Catalysis and Chemical Synthesis) and the hospitality of the NCSU during his visits at the Department of biomolecular and chemical engineering for the development of this work.

## 4.6 References

1. Gray, C.; Gubbins, K.; Joslin, C. Theory of Molecular Fluids 2. Applications. In Oxford Science Publications; Oxford University Press, 2011; Sec. 8.3.
2. Chen, K. *et al.* Electrostatic selectivity in protein-nanoparticle interactions. *Biomacromolecules* **12**, 2552–2561 (2011).
3. Steiner, E., Gastl, M. & Becker, T. Protein changes during malting and brewing with focus on haze and foam formation: A review. *European Food Research and Technology* **232**, 191–204 (2011).
4. Egan, T., O’Riordan, D., O’Sullivan, M. & Jacquier, J. C. Cold-set whey protein microgels as pH modulated immobilisation matrices for charged bioactives. *Food Chem.* **156**, 197–203 (2014).
5. Barroso da Silva, F. L., Pasquali, S., Derreumaux, P. & Dias, L. G. Electrostatics analysis of the mutational and pH effects of the N-terminal domain self-association of the major ampullate spidroin. *Soft Matter* **12**, 5600–12 (2016).
6. Wagoner, T., Vardhanabhuti, B. & Foegeding, E. A. Designing Whey Protein–Polysaccharide Particles for Colloidal Stability. *Annu. Rev. Food Sci. Technol.* **7**, 93–116 (2016).
7. Whitaker, M. ., Howdle, S. M. & Shakeseff, K. M. Polymeric delivery of protein-based drugs. *Bus. Brief. Pharmatech* 118–123 (2002).
8. Home, D. S. Food colloids - emulsions, gels and foams. *Curr. Opin. Colloid Interface Sci.* **5**, 173–175 (2000).
9. Doublier, J. L., Garnier, C., Renard, D. & Sanchez, C. Protein-polysaccharide

- interactions. *Current Opinion in Colloid and Interface Science* **5**, 202–214 (2000).
10. Baskin, E. M., Shklovskii, B. I. & Zilberstein, G. V. Electrophoretic separation of proteins via complexation with a polyelectrolyte. *Phys. A Stat. Mech. its Appl.* **317**, 313–320 (2003).
  11. De Kruif, C. G., Weinbreck, F. & De Vries, R. Complex coacervation of proteins and anionic polysaccharides. *Current Opinion in Colloid and Interface Science* **9**, 340–349 (2004).
  12. de Vries, R. & Cohen Stuart, M. Theory and simulations of macroion complexation. *Current Opinion in Colloid and Interface Science* **11**, 295–301 (2006).
  13. De Vries, R., Weinbreck, F. & De Kruif, C. G. Theory of polyelectrolyte adsorption on heterogeneously charged surfaces applied to soluble protein-polyelectrolyte complexes. *J. Chem. Phys.* **118**, 4649–4659 (2003).
  14. Weinbreck, F., de Vries, R., Schrooyen, P. & de Kruif, C. G. Complex coacervation of whey proteins and gum arabic. *Biomacromolecules* **4**, 293–303 (2003).
  15. Arshady, R. Microcapsules for food. *J. Microencapsul.* **10**, 413–35 (1993).
  16. Yoshioka, T., Sternberg, B. & Florence, A. T. Preparation and properties of vesicles (niosomes) of sorbitan monoesters (Span 20, 40, 60 and 80) and a sorbitan triester (Span 85). *Int. J. Pharm.* **105**, 1–6 (1994).
  17. Hugerth, A., Caram-Lelham, N. & Sundelöf, L.-O. The effect of charge density and conformation on the polyelectrolyte complex formation between carrageenan and chitosan. *Carbohydr. Polym.* **34**, 149–156 (1997).
  18. De Kruif, C. G. & Tuinier, R. Polysaccharide protein interactions. in *Food*

- Hydrocolloids* **15**, 555–563 (2001).
19. Girard, M., Turgeon, S. L. & Gauthier, S. F. Thermodynamic parameters of  $\beta$ -lactoglobulin-pectin complexes assessed by isothermal titration calorimetry. *J. Agric. Food Chem.* **51**, 4450–4455 (2003).
  20. Carlsson, F., Linse, P. & Malmsten, M. Monte Carlo simulations of polyelectrolyte-protein complexation. *J. Phys. Chem. B* **105**, 9040–9049 (2001).
  21. Barroso da Silva, F. L. & MacKernan, D. Benchmarking a fast proton titration scheme in implicit solvent for biomolecular simulations. *J. Chem. Theory Comput.* **13**, 2915–2929 (2017).
  22. Lewis, M. & Bamforth, C. W. *Essays in brewing science*. (Springer, 2006).
  23. Garrett, R. H. & Grisham, C. M. *Biochemistry*. Saunders College Publishing (Saunders's College Publishing, 1999).
  24. Foegeding, E. A. Food Protein Functionality--A New Model. *J. Food Sci.* **80**, C2670–C2677 (2015).
  25. Verway, E. J. W. & Overbeek, J. T. G. Theory of the Stability of Lyophobic Colloids. *J. Phys. Colloid Chem.* **51**, 631–636 (1948).
  26. Voorn, M. J. Journal of Royal Netherlands Chemical Society. *Recl. Des Trav. Chim. Des Pays-Bas-Journal R. Netherlands Chem. Soc.* **5**, 317–330 (1956).
  27. Overbeek, J. T. G. & Voorn, M. J. Phase separation in polyelectrolyte solutions. Theory of complex coacervation. *J. Cell. Comp. Physiol.* **49**, 7–26 (1957).
  28. Netz, R. R. Electrostatics of counter-ions at and between planar charged walls: From Poisson-Boltzmann to the strong-coupling theory. *Eur. Phys. J. E* **5**, 557–574

- (2001).
29. Naji, A., Arnold, A., Holm, C. & Netz, R. R. Attraction and unbinding of like-charged rods. *Europhys. Lett.* **67**, 130–136 (2004).
  30. Jönsson, B., Lund, M. & Da Silva, F. L. B. Electrostatics in macromolecular solutions. *Food Colloids Self-Assembly Mater. Sci.* **302**, 129–154 (2007).
  31. Grymonpre, K. R., Staggemeier, B. A., Dubin, P. L. & Mattison, K. W. Identification by Integrated Computer Modeling and Light Scattering Studies of an Electrostatic Serum Albumin-Hyaluronic Acid Binding Site. *Biomacromolecules* **2**, 422–429 (2001).
  32. Hattori, T., Hallberg, R. & Dubin, P. L. Roles of electrostatic interaction and polymer structure in the binding of  $\beta$ -lactoglobulin to anionic polyelectrolytes: measurement of binding constants by frontal analysis continuous capillary electrophoresis. *Langmuir* **16**, 9738–9743 (2000).
  33. Seyrek, E., Dubin, P. L., Tribet, C. & Gamble, E. A. Ionic strength dependence of protein-polyelectrolyte interactions. *Biomacromolecules* **4**, 273–282 (2003).
  34. Cooper, C. L., Dubin, P. L., Kayitmazer, A. B. & Turksen, S. Polyelectrolyte-protein complexes. *Current Opinion in Colloid and Interface Science* **10**, 52–78 (2005).
  35. Mattison, K. W., Dubin, P. L. & Brittain, I. J. Complex Formation between Bovine Serum Albumin and Strong Polyelectrolytes: Effect of Polymer Charge Density. *J. Phys. Chem. B* **102**, 3830–3836 (1998).
  36. Xu, Y., Mazzawi, M., Chen, K., Sun, L. & Dubin, P. L. Protein purification by polyelectrolyte coacervation: Influence of protein charge anisotropy on selectivity.

- Biomacromolecules* **12**, 1512–1522 (2011).
37. Hattori, T., Kimura, K., Seyrek, E. & Dubin, P. L. Binding of Bovine Serum Albumin to Heparin Determined by Turbidimetric Titration and Frontal Analysis Continuous Capillary Electrophoresis. *Anal. Biochem.* **295**, 158–167 (2001).
  38. Molina-Bolívar, J. A., Galisteo-González, F. & Hidalgo-Álvarez, R. Colloidal stability of protein-polymer systems: A possible explanation by hydration forces. *Phys. Rev. E* **55**, 4522–4530 (1997).
  39. Overbeek, J. T. G. Colloids. A fascinating subject: Introductory Lecture. *Colloid. Dispersions* (ed. J.W. Goodwin) **43**, (1982).
  40. Kesvateraaj, T., Jonsson, B., Thulin, E. & Linse, S. Binding of Ca<sup>2+</sup> to Calbindin D9k: Structural Stability and Function at High Salt Concentration. *Biochemistry* **33**, 14170–14176 (1994).
  41. Yigit, C., Heyda, J. & Dzubiella, J. Charged patchy particle models in explicit salt: Ion distributions, electrostatic potentials, and effective interactions. *J. Chem. Phys.* **143**, (2015).
  42. Yigit, C., Heyda, J., Ballauff, M. & Dzubiella, J. Like-charged protein-polyelectrolyte complexation driven by charge patches. *J. Chem. Phys.* **143**, (2015).
  43. de Vries, R. Monte Carlo simulations of flexible polyanions complexing with whey proteins at their isoelectric point. *J. Chem. Phys.* **120**, 3475–3481 (2004).
  44. Kirkwood, J. G. & Shumaker, J. B. Forces between protein molecules in solution arising from fluctuations in proton charge and configuration. **38**, 863–871 (1952).
  45. da Silva, F. L. B. & Jönsson, B. Polyelectrolyte–protein complexation driven by

- charge regulation. *Soft Matter* **5**, 2862 (2009).
46. Biesheuvel, P. M. & Stuart, M. A. C. Electrostatic free energy of weakly charged macromolecules in solution and intermacromolecular complexes consisting of oppositely charged polymers. *Langmuir* **20**, 2785–2791 (2004).
  47. Noid, W. G. Perspective: Coarse-grained models for biomolecular systems. *J. Chem. Phys.* **139**, (2013).
  48. Levesque, D., Weis, J. J. & Hansen, J. P. in 47–120 (Springer Berlin Heidelberg, 1986). doi:10.1007/978-3-642-82803-4\_2
  49. Binder, K. *Monte Carlo Methods in Statistical Mechanics*. (Berlin: Springer-Verlag, 1986).
  50. Barroso da Silva, F. L., Lund, M., Jönsson, B. & Åkesson, T. On the Complexation of Proteins and Polyelectrolytes. *J. Phys. Chem. B* **110**, 4459–4464 (2006).
  51. Brasil, C. R. S., Delbem, A. C. B. & Da Silva, F. L. B. Multiobjective evolutionary algorithm with many tables for purely ab initio protein structure prediction. *J. Comput. Chem.* **34**, 1719–1734 (2013).
  52. Kesvatera, T., Jönsson, B., Thulin, E. & Linse, S. Ionization behavior of acidic residues in calbindin D(9k). *Proteins Struct. Funct. Genet.* **37**, 106–115 (1999).
  53. Labbez, C. & Jönsson, B. A New Monte Carlo Method for the Titration of Molecules and Minerals. *Appl. Parallel Comput. State Art Sci. Comput.* 66–72 (2009). doi:10.1007/978-3-540-75755-9\_8
  54. Teixeira, A. A. R., Lund, M. & Da Silva, F. L. B. Fast proton titration scheme for multiscale modeling of protein solutions. *J. Chem. Theory Comput.* **6**, 3259–3266

(2010).

55. Nozaki, Y. & Tanford, C. Examination of titration behavior. *Methods Enzymol.* **11**, 715–734 (1967).
56. Ralet, M. C., Dronnet, V., Buchholt, H. C. & Thibault, J. F. Enzymatically and chemically de-esterified lime pectins: Characterisation, polyelectrolyte behaviour and calcium binding properties. *Carbohydr. Res.* **336**, 117–125 (2001).
57. Chen, W., Wallace, J., Yue, Z. & Shen, J. Introducing Titratable Water to All-Atom Molecular Dynamics at Constant pH. *Biophys. J.* **105**, L15–L17 (2013).

## Appendix

**Table A4.1:**  $\Delta pK_a$  values for all the titratable amino acid side chains and their locations in the PDB structure for the  $\alpha$ -lactalbumin.  $\Delta pK_a$  values were calculated between  $pK_{aPPol}$  (protein+polyelectrolyte) and  $pK_{aP}$  (isolated protein), as well as between  $pK_{aPPol}$  and  $pK_0$  (ideal  $pK_a$ ).

Location	Amino acid side chain	$pK_{aPPol}$ (Protein+polyelectrolyte)	$pK_{aP}$ (Isolated protein)	Difference between $pK_{aPPol}$ and $pK_{aP}$	Difference between $pK_{aPPol}$ and $pK_0$
1	GLU	4.9	4.5	0.3	0.4
5	LYS	12.1	12.1	-0.1	1.7
7	GLU	4.4	3.9	0.5	0.0
11	LYS	14.4	14.7	-0.3	4.0
13	LYS	11.4	11.4	0.0	1.0
14	ASP	4.0	1.8	2.1	0.0
16	LYS	11.8	11.9	0.1	1.4
17	ASP	4.1	2.6	1.5	0.1
18	TYR	10.3	10.4	-0.1	0.6
25	GLU	3.9	2.4	1.4	-0.5
32	HIS	6.3	6.3	0.0	0.0
36	TYR	10.0	10.1	-0.1	0.4
37	ASP	4.3	3.8	0.6	0.3
46	ASP	3.9	2.6	1.3	-0.1
49	GLU	4.8	3.8	1.0	0.4
50	TYR	12.2	12.3	-0.2	2.6
58	LYS	13.1	13.2	-0.1	2.7
62	LYS	11.6	11.6	0.0	1.2
63	ASP	4.6	3.5	1.1	0.6
64	ASP	4.4	3.5	0.9	0.4
68	HIS	6.3	6.3	0.0	0.0
70	ARG	12.0	12.0	0.0	0.0
78	ASP	4.3	3.3	1.0	0.3
79	LYS	12.6	12.7	-0.1	2.2
82	ASP	2.5	0.7	1.8	-1.5
83	ASP	4.5	4.0	0.5	0.5
84	ASP	4.3	3.2	1.0	0.3
87	ASP	2.5	-1.0	3.4	-1.5

**Table A4.1 Continued**

Location	Amino acid side chain	pK <sub>aPPol</sub> (Protein+polyelectrolyte)	pK <sub>aP</sub> (Isolated protein)	Difference between pK <sub>aPPol</sub> and pK <sub>aP</sub>	Difference between pK <sub>aPPol</sub> and pK <sub>0</sub>
88	ASP	2.6	0.1	2.4	-1.4
93	LYS	13.3	13.4	-0.1	2.9
94	LYS	11.7	11.7	0.0	1.3
97	ASP	4.3	2.3	2.1	0.3
98	LYS	11.3	11.3	0.0	0.9
103	TYR	10.6	10.7	-0.1	1.0
107	HIS	6.3	6.3	0.0	0.0
108	LYS	12.8	12.8	-0.1	2.4
113	GLU	4.4	3.6	0.8	0.0
114	LYS	11.7	11.8	0.0	1.3
116	ASP	3.7	2.6	1.1	-0.3

**Table A4.2:**  $\Delta pK_a$  values for all the titratable amino acid side chains and their locations in the PDB structure for the lysozyme.  $\Delta pK_a$  values were calculated between  $pK_{a_{ppol}}$  (protein+polyelectrolyte) and  $pK_{a_p}$  (isolated protein), as well as between  $pK_{a_{ppol}}$  and  $pK_0$  (ideal  $pK_a$ ).

Location	Amino acid side chain	$pK_{a_{ppol}}$ (Protein+polyelectrolyte)	$pK_{a_p}$ (Isolated protein)	Difference between $pK_{a_{ppol}}$ and $pK_{a_p}$	Difference between $pK_{a_{ppol}}$ and $pK_0$
1	LYS	10.9	10.7	0.2	0.5
5	ARG	12.0	12.0	0.0	0.0
7	GLU	4.8	2.5	2.4	0.4
13	LYS	11.2	11.2	0.1	0.8
14	ARG	12.0	12.0	0.0	0.0
15	HIS	6.3	6.3	0.0	0.0
18	ASP	3.9	2.2	1.7	-0.1
20	TYR	9.3	8.4	0.9	-0.3
21	ARG	12.0	12.0	0.0	0.0
23	TYR	9.7	8.8	0.9	0.1
33	LYS	10.8	10.1	0.6	0.4
35	GLU	4.5	2.8	1.6	0.1
45	ARG	12.0	12.0	0.0	0.0
48	ASP	3.6	2.5	1.0	-0.4
52	ASP	4.0	2.6	1.4	0.0
53	TYR	9.9	9.3	0.6	0.3
61	ARG	12.0	12.0	0.0	0.0
66	ASP	2.9	1.9	1.0	-1.1
68	ARG	12.0	12.0	0.0	0.0
73	ARG	12.0	12.0	0.0	0.0
87	ASP	4.0	1.9	2.0	0.0
96	LYS	11.2	11.0	0.1	0.8
97	LYS	11.4	11.3	0.1	1.0
101	ASP	3.5	1.9	1.6	-0.5
112	ARG	12.0	12.0	0.0	0.0
114	ARG	12.0	12.0	0.0	0.0
116	LYS	10.8	10.4	0.4	0.4
119	ASP	3.7	2.3	1.4	-0.3
125	ARG	12.0	12.0	0.0	0.0
128	ARG	12.0	12.0	0.0	0.0

**Table A4.2 Continued**

Location	Amino acid side chain	$pK_{a_{ppol}}$ (Protein+polyelectrolyte)	$pK_{a_p}$ (Isolated protein)	Difference between $pK_{a_{ppol}}$ and $pK_{a_p}$	Difference between $pK_{a_{ppol}}$ and $pK_0$
129	CTR	3.5	1.7	1.9	0.3
130	NTR	8.1	6.8	1.3	-0.4

## CHAPTER 4 : Conclusions and Future Work

In this dissertation, we have used Monte Carlo methods to perform simulations to study three main topics of interest:

- a) the effect of molecular shape and fluid-wall interactions on pressures in carbon pores,
- b) the effect of confinement on chemical reactions in carbon pores, and
- c) the significance of the charge regulation mechanism in driving protein-polyelectrolyte complexation for milk proteins.

We used several different ensembles to study the varied systems. These include the constant-pressure Gibbs Ensemble, referred to as CP-GEMC in this text, the Reactive Monte Carlo (RxMC) technique, and the semi-grand canonical ensemble. In addition to the Monte Carlo methods utilized, we also used other techniques to aid in understanding the systems of interest. For example, we conducted *ab initio* calculations to determine more accurate fluid-wall interaction energies for the nitric oxide molecules in the carbon pores. In order to calculate the pressure in pores, which exists as a second-order tensor, we used the mechanical route along with the Irving-Kirkwood method to calculate both the normal and tangential pressure tensors in slit-shaped pores.

Below is a conclusion of our findings for each section in this dissertation.

### 5.1 Pressure Enhancement in Confined Fluids

In Chapter 2, we examined the effect on the tangential pressure of varying the molecular shape, strength of the fluid-wall interactions, and pore width, for carbon slit-shaped

pores. We show that molecular shape and pore size have a notable impact on the layering of molecules in the pore, greatly influencing both the shape and scale of the tangential pressure profile. We further demonstrate that the strength of the fluid-wall interactions has a large impact on the pressure tensor, due to its direct effect on the molecular density.

The data for the monomers consistently showed sharp peaks in the tangential pressure but the magnitude of these peaks increased significantly with the strength of the fluid-wall interactions and with pore width, due to an increased number density of monomers in the pore. For multi-site molecules, the presence of additional rotational degrees of freedom led to unique changes in the shape of the tangential pressure profile, such as broad shoulders attached to the sharp peaks in the tangential profile, a unique phenomenon that is not observed with single-site Lennard Jones molecules. This phenomenon was especially obvious in larger pores. In addition, like the monomers, the multi-site molecules also experienced an increase in the magnitude of their tangential pressure peaks with stronger fluid-wall interactions.

Due to the strong attraction between the fluid molecules and the carbon wall, the adsorbed molecules in the contact layers were very densely packed and extremely well-aligned. In the future, it would be interesting to compare the tangential pressure peaks for the contact and inner layers to the virial pressure of a strictly 2-D Lennard-Jones system at high density. From our literature review, we failed to find a 2-D equation of state that describes 2-D LJ systems at reduced densities higher than  $\rho^* = \rho\sigma^2 = 0.8$ , where the 2-D density is  $\rho=N/A$ . We calculated the reduced density of our adsorbed contact layers to be in the range of 1.0 to 1.3 for the systems studied in this chapter, indicating a need for an equation of state to describe this region of the 2-D Lennard-Jones phase diagram.

## 5.2 The Nitric Oxide Dimer Reaction

Using RxMC and CP-GEMC, we studied the equilibrium conversion of the nitric oxide dimerization reaction in carbon slit-shaped pores and carbon nanotubes in Chapter 3. While previous simulation studies have used Lorentz-Berthelot (LB) mixing rules to approximate the interaction energies between the adsorbate molecules and carbon walls, we used *ab initio* quantum chemistry methods to calculate more accurate interaction energies between the nitric oxide monomer and dimer molecules and a benzene ring. The resulting interaction energies were over 16 and 21 times greater than those predicted by the LB mixing rules for the monomer and dimer sites, respectively. After accounting for the stronger fluid-wall interactions, we consistently found higher reaction conversions in a variety of slit pore sizes, ranging from  $H = 3\sigma$  to  $H = 5.5\sigma$ , compared to previous simulation studies. The slit pore of width  $H = 3\sigma$  showed the highest reaction conversion of around 90%. Over the temperature range studied (120 – 160 K), we detected little to no temperature dependency indicating that the stronger fluid-wall interactions overpower any temperature effects in this temperature range that would otherwise be observed through Le Chatelier's principle. Pore width was also found to affect the reaction conversion due to the monomers and dimers packing differently in different pore sizes. Furthermore, we calculated the slit-pore pressure tensor using the mechanical route and found the tangential pressure to generally increase with increasing pore width to reach millions of bar.

Confinement had an even larger impact on the NO dimerization reaction in carbon nanotubes. The conversion in carbon nanotubes was found to be around 89% for the (10,10)

bundle and reached up to 98% for the (8,8) bundle, indicating that the diameter of the carbon nanotube has a notable effect on the reaction conversion.

While our results consistently showed much better agreement with experiments than prior simulation studies, there is still a small discrepancy that is yet to be resolved. We hypothesize that this discrepancy could be due to using only one benzene ring to simulate a graphene sheet for our *ab initio* calculations. It is possible that more benzene rings are required to obtain a more accurate fluid-wall interaction energy but the computing resources required for calculations involving additional rings are not insignificant. In addition, it might also be beneficial to study the carbon nanotube bundles in an orthorhombic simulation box. This would allow whole nanotubes to pack hexagonally and avoid any edge effects that can occur with orthogonal box dimensions.

### **5.3 Protein-Polyelectrolyte Interactions**

In Chapter 4, we studied the attractive phenomenon in protein-polyelectrolyte complexation that has often been described as “complexation on the wrong side of pI”. The driving force for this attraction is often attributed to one of two interactions: a) ion-dipole interactions forming “charged patches” on the protein surface, or b) charge-induced interactions due to perturbations of the acid-base equilibrium. Using constant-pH Monte Carlo simulations in the semi-grand canonical ensemble focusing mainly on electrostatic interactions, along with several quantitative and visual analysis tools, we investigated the significance of each of these interactions for two whey proteins,  $\alpha$ -lactalbumin ( $\alpha$ -LA) and lysozyme (LYZ). We conducted simulations at varying pH levels and through physical

chemistry parameters and free energies of interactions, we showed the charge regulation mechanism to be the most important contributor in protein-polyelectrolyte complexation regardless of pH, dipole moment, and protein capacitance. In addition, mapping the amino acid *pKa* shifts on protein surfaces and visualizing the coordinates of the polyelectrolyte trajectory with respect to the proteins failed to reveal any preferential hot spots. These measures of analysis help provide significant evidence suggesting that charge regulation is the more important mechanism in protein-polyelectrolyte complexation.